Analysis of a Lateral Spreading Case History from the 2007 Pisco, Peru Earthquake

Rajat M. Gangrade

Thesis submitted to the faculty of the Virginia Polytechnic Institute and State University in partial fulfillment of the requirements for the degree of

Master of Science

In

Civil Engineering

Adrian Rodriguez-Marek, Chair

Joseph E. Dove

Russell A. Green

June 7, 2013

Blacksburg, VA

Keywords:

Lateral Spreading

Slope Stability Analysis

Bayesian Updating

Analysis of a Lateral Spreading Case History from the 2007 Pisco, Peru Earthquake

Rajat M. Gangrade

ABSTRACT

On August 15, 2007, Pisco, Peru was hit by an earthquake of Magnitude (Mw) = 8.0 which triggered multiple liquefaction induced lateral spreads. The subduction earthquake lasted for approximately 100 seconds and showed a complex rupture. From the geotechnical perspective, the Pisco earthquake was significant for the amount of soil liquefaction observed. A massive liquefaction induced seaward displacement of a marine terrace was observed in the Canchamana complex. Later analysis using the pre- and post-earthquake images showed that the lateral displacements were concentrated only on some regions. Despite the lateral homogeneity of the marine terrace, some cross-sections showed large displacements while others had minimal displacements. The detailed documentation of this case-history makes it an ideal case-study for the determination of the undrained strength of the liquefied soils; hence, the main objective of this research is to use the extensive data from the Canchamana Slide to estimate the shear strength of the liquefied soils. In engineering practice, the undrained strength of liquefied soil is typically estimated by correlating SPT-N values to: 1) absolute value of residual strength, or 2) residual strength ratio. Our research aims to contribute an important data point that will add to the current understanding of the residual strength of liquefied soils.

Acknowledgements

I would like to thank my committee chair, Dr. Adrian Rodriguez-Marek, without whom this work would not have been possible. I sincerely thank him for believing in my abilities and being patient enough throughout. I extend my acknowledgement to Dr. Russell Green for being an inspiration and a role model. I thank him for showing the way to work meticulously and logically. I thank Dr. Joseph Dove for his guidance when I first landed at Virginia Tech and for being on my committee. I owe my deepest gratitude to my committee, who undertook to act as my supervisors despite their other academic and professional commitments. Their wisdom, knowledge and commitment to the highest standards inspired and motivated me.

I would also like to acknowledge the contributions of Haitham Dawood, Brett Maurer, Abeera Batool and Manisha Rai who extended their support in guiding me through graduate school. Acknowledgment and thanks go to my parents, Prof. Mukesh Gangrade and Prof. Rajani Gangrade, for putting me through my graduate program, believing in me and encouraging me in all my endeavors towards graduate studies. My sisters, Mehek, Manasi and Devanshi are just generally cool and should be so recognized. Finally, the friends and acquaintances I have made in Blacksburg are too numerous to list entirely, so I won't even make an attempt at a complete roster. I do mention Sayantani, Hemanth, Sushrut, Tanmay, Avinash and Suvarna for being an enjoyable company and motivating me to complete my thesis and dissertation

Table of Contents

1 INTRODUCTION 1

1.1 Pisco Earthquake – Seismological Aspects 1

1.2 Liquefaction failure in Canchamana 2

1.3 Objective and Scope 4

2 LITERATURE REVIEW 6

2.1 Existing methodologies to calculate shear strength of liquefied soil 6

2.2 Liquefaction induced lateral spreading 8

2.2.1 Empirical Models 10

2.2.2 Simplified Analytical Models 13

2.2.3 Finite Element Models 14

2.3 Slope stability analysis of liquefied soils 15

2.4 Use of Bayesian Techniques in Geotechnical Engineering 20

SUMMARY 22

REFERENCES 24

ABSTRACT 28

3 INTRODUCTION 29

3.1 Data Collection 31

3.1.1 Reconnaissance observations 31

3.1.2 Field Exploration 33

3.2 Methodology 39

3.3 Development of cross sections 40

3.3.1 Approach A: uniform profile 40

3.3.2 Approach B: non-uniform profile 41

3.4 Interpretation of displacement observations 42

3.5 Liquefied Shear Strength Ratio 44

3.6 Seismic Slope Stability Analysis 48

3.7 The Limit State Line 51

3.8 Bayesian Updating Technique 53

3.9 Results and Discussion 59

3.10 Summary and Conclusions 69

ACKNOWLEDGEMENTS 71

REFERENCES 72

4 ENGINEERING SIGNIFICANCE & RECOMMENDATIONS FOR FUTURE WORK 76

APPENDIX I: COMPOSITION OF RECONNAISSANCE AND FIELD INVESTIGATION TEAMS 79

APPENDIX II: SLOPE STABILITY ANALYSIS 81

APPENDIX III: SUMMARY OF BAYESIAN UPDATING TECHNIQUE AND RESULTS 108

List of Tables

Table 3.1. SPT test number and the corresponding bins 35

Table 3.2. Maximum displacement in each bin and classification of the bin 44

Table 3.3. Estimated $\mu lnPGA$ values from Approach A for the 'c' value corresponding to the upper bound of Olson and Stark (2002) relationship. 64

Table 3.4. Range of 'c' values using Approach A and assuming that the median PGA is that measured by the ICA-2 station. 64

Table 3.5. Range of $\mu lnPGA$ values (g), from Approach B, for the 'c' value corresponding to the upper bound of Olson and Stark (2002) relationship. 67

Table 3.6. Range of 'c' values using Approach B and assuming that the median PGA is that measured by the ICA2 station.....68

Table AI-1. Reconnaissance team.....79

Table AI-2. Field Investigation teams.....80

Table AIII-1. Limit State Line equation for bins. The equation gives the MHEA as a function of c.....110

Table AIII-2. Bayesian updating technique set-up for 'Failed' bin 111

Table AIII-3. Bayesian updating technique set-up for a 'Non-Failed' bin.....111

Table AIII-4. Evaluating posterior distribution from the 'failure' and 'no-failure' probabilities of the bins 112

Table AIII-5. Bayesian Updating Tables for Non-Uniform profile for a combination of 'failed' Bin (3) and 'non-failed' Bin (2) for median PGA = 0.31 g and standard deviation of PGA = 0.1 113

Table AIII-6. Bayesian Updating Tables for Uniform profile for a combination of 'failed' Bin (12) and 'non-failed' Bin (20) for median PGA = 0.26 g and standard deviation of PGA = 0.2 114

List of Figures

Figure 1.1. Accelerogram recorded in ICA at station ICA -2. For ICA-2, $R_{jb} = 0$ 2

Figure 2.1. Schematic force diagram for simplified slope stability analysis (Olson 2001) 16

Figure 2.2. Simplified pre-failure and post-failure geometry of Lower San Fernando Dam (Olson 2001) 17

Figure 2.3. Pre- and post-failure geometry of Calaveras Dam (Olson 2001).....18

Figure 2.4. Post-failure geometry of Calaveras Dam used for liquefied shear strength ratio analyses (Olson 2001) 19

Figure 3.1. Epicenter and overview of the affected area from the 2007 Pisco Earthquake (MAE 2008) 29

Figure 3.2. Sketch of the cross-section at Canchamana illustrating the massive displacement of the marine terrace (from: GEER 2007).....32

Figure 3.3. Overview of the affected area at Canchamana showing bin numbers, SPT and MASW test locations (Background image from Google Earth).....34

Figure 3.4. Soil profiles for Bin (2) inferred from SPT borings (left) and SPT N-value profiles (right), including the average SPT profile for the bin.....36

Figure 3.5. Soil profiles for Bin (3) inferred from SPT borings (left) and SPT N-value profiles (right), including the average SPT profile for the bin.....36

Figure 3.6. Soil profiles for Bin (20) inferred from SPT borings (left) and SPT N-value profiles (right), including the average SPT profile for the bin.....37

Figure 3.7. Soil profiles for Bin (12) inferred from SPT borings (left) and SPT N-value profiles (right), including the average SPT profile for the bin.....37

Figure 3.8. DEM map of the Canchamana lateral spread complex (Courtesy of Dr. B. Cox). The color indicates surface elevation while the vectors superposed on the map are displacement vectors estimated from comparison of pre- and post-earthquake satellite images. 38

Figure 3.9. Representative model of the cross-section of bin (3) with the layering of the soil profile and the test locations. (Figure Not to Scale).....41

Figure 3.10. Representative model of the cross-section of bin (12) with the layering of the soil profile and the test locations. (Figure Not to Scale) 42

Figure 3.11. Magnitude and azimuth of the displacement vectors within the 20 bins as recorded in post-earthquake analysis. For reference, the displacement direction perpendicular to the coast has an azimuth of -100^{o} 43

Figure 3.12. A comparison of liquefied strength ratio relationships based on the normalized SPT blowcount (from:Olson and Stark 2002).....46

Figure 3.13: Interpolations between the upper and the lower bound curves from the (Olson and Stark 2002) proposed relationship 47

Figure 3.14. Extending the interpolated curves in Olson and Stark (2002) relationship to $(N_1)_{60}$ values > 12 using the slope from Davies and Campanella (1994) curves.....48

Figure 3.15. Limit State line for bins (2), (3), (12) and (20) on the basis of uniform SPT values in the profile (Approach-A).....52

Figure 3.16. Limit State line for bins (2), (3), (12) and (20) on the basis of uniform SPT values in the profile (Approach-B) 53

Figure 3.17. Normalized Maximum Horizontal Equivalent Acceleration versus Normalized Fundamental Period of Waste Fill for a Rock Site. (Bray and Rathje 1998) 55

Figure 3.18. Attenuation relationships for subduction zone earthquakes along with the recordings from the 2007 Pisco earthquake. The ICA–2 station recordings are highlighted.....57

Figure 3.19. Posterior distribution curves for a combination of bin (12) and bin (20) uniform profiles (Approach -A) for $\sigma lnPGA$ = 0.65.....59

Figure 3.20. Posterior distribution curves for a combination of bin (12) and bin (20) non-uniform profiles (Approach B) for $\sigma lnPGA$ = 0.65 60

Figure 3.21. Correlation between 'c' values and the estimated mean PGA ($\mu lnPGA$) from bin (12) and bin (20) limit state lines using Approach-A. Red lines indicate best estimate PGA.....61

Figure 3.22. Correlation between 'c' values and the estimated mean PGA ($\mu lnPGA$) from bin (3) and bin (20) limit state lines using Approach-A. Red lines indicate best estimate PGA. 62

Figure 3.23. Correlation between 'c' values and the estimated mean PGA ($\mu lnPGA$) from bin (12) and bin (2) limit state lines using Approach-A. Red lines indicate best estimate PGA. 62

Figure 3.24 Correlation between 'c' values and the estimated mean PGA ($\mu lnPGA$) from bin (3) and bin (2) limit state lines using Approach-A. Red lines indicate best estimate PGA. 63

Figure 3.25. Correlation between 'c' values and the estimated mean PGA ($\mu lnPGA$) from bin (12) and bin (20) limit state lines using Approach-B. Red lines indicate best estimate PGA. 65

Figure 3.26. Correlation between 'c' values and the estimated mean PGA ($\mu lnPGA$) from bin (3) and bin (20) limit state lines using Approach-B. Red lines indicate best estimate PGA. 65

Figure 3.27. Correlation between 'c' values and the estimated mean PGA ($\mu lnPGA$) from bin (12) and bin (2) limit state lines using Approach-B. Red lines indicate best estimate PGA. 66

Figure 3.28. Correlation between 'c' values and the estimated mean PGA ($\mu lnPGA$) from bin (3) and bin (2) limit state lines using Approach-B. Red lines indicate best estimate PGA. 66

Figure 3.29. Estimated range of constant value 'c' between Approach A and Approach B bounds 69

Figure AII-1. SLIDE input file for Bin (12), Uniform Profile 83

Figure AII - 2. Layering for Bin (12) – Uniform Profile 84

Figure AII - 3. Output for Bin (12) – Uniform Profile 85

Figure AII-4. SLIDE input file for Bin (12) – Non-uniform layering 86

Figure AII-5. Layering for Bin (12) Non-uniform profile 87

Figure AII-6. Output file for Bin (12), Non-uniform profile 88

Figure AII-7. SLIDE input file for Bin (20), Non-uniform profile 89

Figure AII-8. Output file for Bin (20), Non-uniform profile 90

Figure AII-9. Output file for Bin (20), Uniform profile. 91

Figure AII-10.SLIDE input file for Bin (3), Uniform profile 92

Figure AII-11. Output file for Bin (3), Uniform profile 93

Figure AII-12. Layering for Bin (3), Non-Uniform profile 94

Figure AII-13. Output for Bin (3), Non-uniform profile 95

Figure AII-14. SLIDE file for Bin (2), Uniform profile 96

Figure AII-15. Output file for Bin (2), Uniform profile 97

Figure AII-16. Output for Bin (2), non-uniform profile 98

1 Introduction

1.1 Pisco Earthquake – Seismological Aspects

On August 15 2007, a large interface event occurred off the coast of Central Peru, the epicenter located about 60 km west of the city of Pisco, and about 145 km SSE of the capital city of Lima. The earthquake has been referred to as the Pisco Earthquake, as Pisco was the most affected city. It was a thrust-faulting event on the interface between the two plates, with the South American plate moving over the Nazca plate. The area affected by the earthquake was about 170 km long and 130 km wide and corresponded to a previously identified seismic gap between the rupture areas of the 1974 Lima event (M_w 7.5) and 1996 Nazca event (M_w 7.7). The 2007 Pisco Earthquake had a moment magnitude (Mw) = 8.0. As per the United States Geological Survey (USGS), the focus of the event was located at 13.35^o S and 76.509^o W, at a hypocentral depth of 39 km. Ji and Zeng (2007) provided the finite fault solution for the event that indicated a rupture plane dip of 27^o. Tavera et al. (2008) reported the Joyner-Boore distance (Rjb) = 0.0 for stations at ICA and Parcona suggesting these cities lied within the ground surface projection of the rupture plane.

Figure (1.1) shows the accelerogram recorded in the ICA province at station ICA-2 that is located at approximately 40 km from the source. The two peaks in the accelerogram correspond to the rupture of asperities located far away from each other. Tavera et al. (2008) denoted the two peaks in the accelerogram as two wave trains R_1 and R_2. As the asperities are separated by a considerable distance, we observe a 65-70 seconds long phase of weak motions between the peaks. However the notable characteristic of the ground motion is the long duration of shaking.

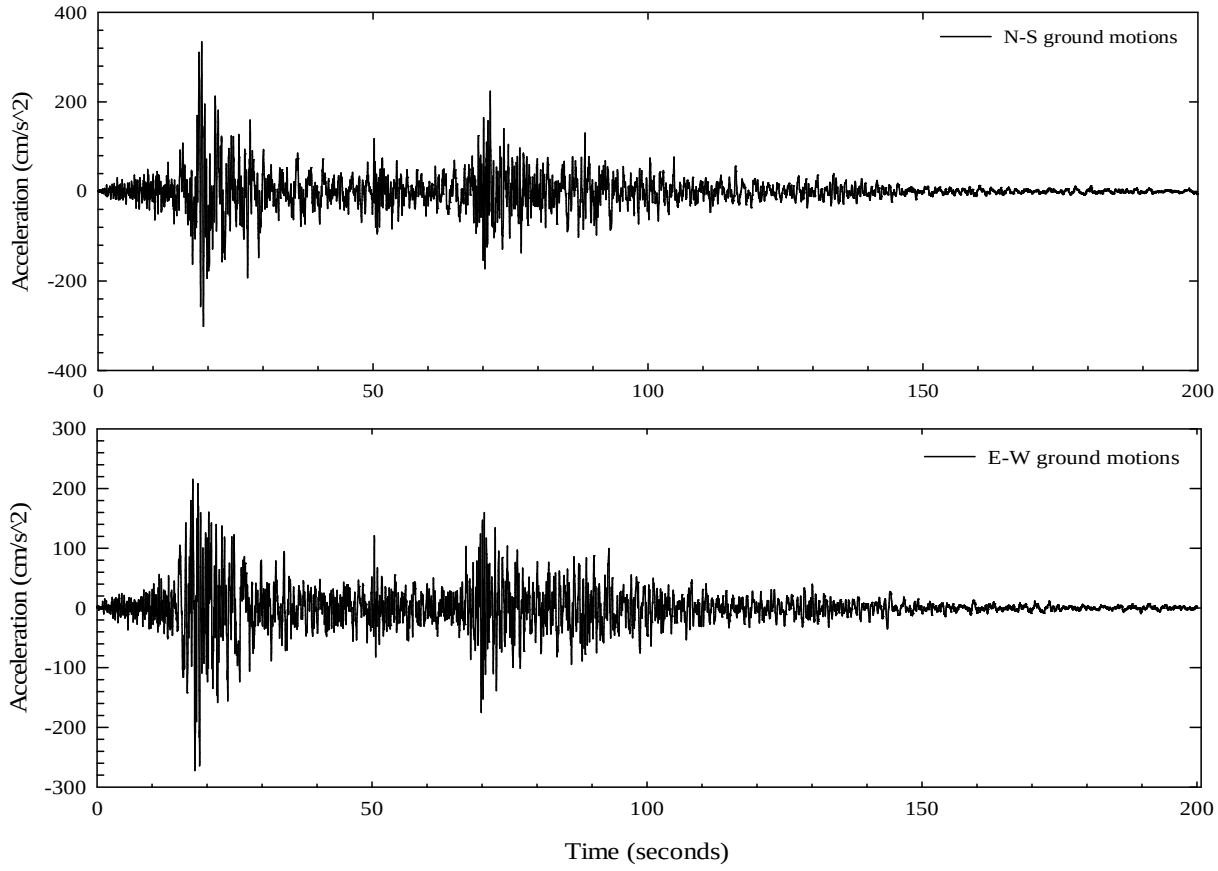

Figure 1.1. Accelerogram recorded in ICA at station ICA -2. For ICA-2, $R_{jb} = 0$.

1.2 Liquefaction failure in Canchamana

The Pisco earthquake was significant for the amount of observed soil liquefaction. Liquefaction induced damage included differential settlements, landslides and lateral spreading. The earthquake caused considerable damage to infrastructure facilities including highway embankment failures, rupture of water and sewer pipelines and foundation failures. The field reconnaissance team found multiple cases of lateral spreading along the coast of Peru.

A massive liquefaction induced lateral spread of one marine terrace was observed in Canchamana (2.5 km north of Tambo de Mora). The reconnaissance team on the basis of field

observations, interpreted the displaced area to be approximately 3 km by 1 km. However, this was just an initial interpretation of the damage. Observations indicate that the marine terrace deposit is composed of a layer of non-liquefiable soil over a layer of silty sand (liquefiable soil). An interface between the marine terrace and the Canete formation (approximately 10-20 m above the marine terrace) defined the eastern boundary of the lateral spread in the terrace. A maximum vertical displacement of about 3 m was observed along the interface between the marine terrace and the Canete formation. Towards the north, lateral spreading of the marine terrace induced failure of an 8 m tall embankment fill, which led to a complete destruction of the Pan American highway - an important infrastructure element. The reconnaissance team pointed out that the depth of the ground water table across the marine terrace varied from approximately 5 m deep at the center of the displaced area to about 2 m deep at approximately 700 m away towards north. Lateral displacements of about 5.0 m were observed in the field. Cracks of about 1 m width and filled with sand ejecta were observed by the reconnaissance team. Sand boils of approximately 2 m diameter were observed at multiple locations in the marine terrace.

After about $2 - {}^{1}/_{2}$ years, a field characterization study was completed in the Canchamana complex. The reconnaissance team carried out a series of in-situ tests in the affected area. The observations and field characterization results from Canchamana complex provide a great opportunity to back-calculate the undrained shear strength of the liquefied soils. In the past, several researchers have presented back-analysis approach on liquefaction induced flow failure case histories. This lateral spreading case history is one of its kind and is used to estimate the undrained shear strength of the liquefied soils. A detailed description of the methodology is given in Chapter 3 of this thesis.

1.3 Objective and Scope

The liquefaction induced lateral spreading ground failure in Canchamana provides a reasonable amount of information to estimate the undrained shear strength of the soil post-liquefaction. The primary objective of the research is to perform back-analysis on the field observations from the Canchamana slide complex to estimate the undrained shear strength of the liquefied soils. In engineering practice, the undrained strength of the liquefied soil is typically estimated by laboratory methods or empirical relations suggested by several researchers. The outcome of this research can serve as recommendations to back calculate the undrained shear strength of the soil undergone liquefaction.

The scope of the research includes the following tasks:

a) Literature Review
b) Utilizing the reconnaissance results to develop cross-sections of liquefied soils.
c) Performing slope stability analysis to evaluate the 'yield acceleration' and the location of weak layer for each cross-section
d) Generating a *Limit State* line for 'failure' and 'non-failure' cross-sections based on the observations in the marine terrace.
e) Applying Bayesian Inference Technique, to either update the uncertainty of PGA at the site, or to get a better estimate of the undrained shear strength, using the observations from the field.

The thesis is presented in the manuscript format and is structured as:

Chapter 2. Literature Review

Chapter 3. Analysis of Lateral Spreading Case Histories from Pisco, Peru Earthquake, 2007.

Chapter 4. Engineering Significance and Recommendations for Future Work.

Appendix- I: Composition of the reconnaissance team.

Appendix –II: Slope Stability Analysis.

Appendix- III: Summary of Bayesian Updating Technique and Results.

2 Literature Review

This chapter presents a literature review of topics associated with the thesis research presented in Chapter 3. The literature review starts with a brief summary of the existing methodologies used in geotechnical engineering practice to estimate the undrained shear strength of liquefied soils. The review then includes a discussion of existing lateral spread displacement models to estimate the surface displacements due to lateral spreading ground failure. A brief discussion of slope stability analysis of slopes with liquefied soils is then provided, along with a case history. The literature review concludes by discussing the significance of probabilistic methods in general geotechnical engineering practice and a short summary of the research study presented subsequently.

2.1 Existing methodologies to calculate shear strength of liquefied soil

The strength of the soil when loaded to failure under undrained conditions is called the undrained shear strength of the soil. In the field, the undrained conditions occur when the loads are applied to a mass of the soil faster than the soil can drain. During liquefaction conditions, a sand behaves temporarily as an undrained material, hence the liquefied shear strength is understood to be the undrained shear strength. Olson and Stark (2002) stated: "*The liquefied shear strength is the shear strength mobilized at large deformation in a saturated, contractive soil following liquefaction.*" Several researchers have proposed procedures to estimate the shear strength of the liquefied soils. In general engineering practice, procedures developed by Poulos et al. (1985), Seed (1987), Seed and Harder (1990), Stark and Mesri (1992) and Olson and Stark (2002) are used. A brief description of the procedures developed by each of the above mentioned researchers is provided below.

As per Poulos et al. (1985), the shear strength of the liquefied soils is based on the concept of undisturbed sampling and laboratory testing. Poulos et al. (1985) developed a laboratory based procedure for evaluating the steady-state shear strength of liquefied soils using multiple consolidated undrained triaxial compression tests on undisturbed and reconstituted soil samples (Stark et al. 1998). Poulos et al. (1985) indicated that the steady state strength is a function of the void ratio after consolidation. The consolidated undrained triaxial tests results are used to determine a relation between the steady state shear strength and void ratio. The resulting steady state line is used to adjust the laboratory test results to in-situ conditions to account for densification through sampling, transportation handling and, laboratory sample preparation. The laboratory testing procedure assumes that: (1) the slope of the steady state line for the undisturbed specimens is same as the slope for reconstituted specimens, and (2) the slope of the steady state line is affected chiefly by the shape of the grains in the given soil sample and is independent of the method used to reconstitute the samples in the laboratory.

Seed (1987) approach is based on the back-analysis of field case histories. In this methodology, the liquefied shear strength of the soil is back-calculated from the information available for the case histories (SPT penetration resistance), by performing limit equilibrium analyses on the post-failure geometry of the slope. The final geometry of the slope and different failure surfaces helped in determining the residual shear strength of the soil. With addition of few case histories to the Seed (1987) data and estimating SPT blow-count from relative densities for some case histories, Seed and Harder (1990) developed a relation between the liquefied shear strength and clean sand blow count, $(N_1)_{60\text{-}cs}$.

Stark and Mesri (1992) presented an approach that suggested an increase in liquefied shear strength due to an increase in pre-failure vertical effective stress. Stark and Mesri (1992) approach

is based on the back-analysis of liquefaction case histories, where the liquefied shear strength is estimated as a function of pre-failure vertical effective stress. With the addition of few case histories to the Seed and Harder (1990) data, Stark and Mesri (1992) developed the relationship between the liquefied strength ratio and $(N_1)_{60\text{-}cs}$ (Olson and Stark 2002). Stark and Mesri (1992) also suggested that many of the liquefaction failures experienced partial drainage during flow and the resulting back calculated shear strength did not represent an undrained condition.

Olson and Stark (2002) proposed a relationship for liquefied shear strength ratio and SPT blow counts, that showed considerably less scatter compared to the bounds presented by Stark and Mesri (1992). The relationship indicated an approximately linear correlation between liquefied shear strength ratio and penetration resistance up to a normalized SPT blow count value of 12. Studies by Stark and Mesri (1992) and Seed and Harder (1990) included the fines content adjustment to generate an 'equivalent clean sand' blow count, $(N_1)_{60\text{-}cs,}$ to evaluate the liquefied shear strength. Fines content adjustment was used to increase the penetration resistance of the silty sands to that shown by the clean sands (Olson and Stark 2002). However, Olson and Stark (2002) did not include fines content adjustment for estimating liquefied strength ratio.

2.2 Liquefaction induced lateral spreading

Seed and Idriss (1982) suggested that as shear waves propagate through the ground, cyclic shear stresses and strains are generated. If a cohesionless soil mass is saturated, excess pore pressures generate as a result of the tendency of the soil to contract under shear, leading to liquefaction. The soil mass undergoes softening as a result of rapid loading under undrained conditions. Various ground failures are associated with soil liquefaction. The most widely discussed ground failures include flow failures of slopes, lateral spreads, sand boils and ground

oscillation. This section of the literature review introduces the lateral spreading ground failure mode and discusses some methodologies to calculate the lateral displacements that result from rapid loading (i.e. earthquake).

Rauch (1997) stated: *"Liquefaction-induced lateral spreading is defined as the finite, lateral displacement of gently sloping ground or virtually flat ground, as a result of pore-pressure build-up in a shallow underlying deposit during an earthquake"*. Bartlett and Youd (1995) mentioned that liquefaction induced lateral spreading occurs on mild slopes underlain by loose sands and shallow water table. Soil deposits comprising of loose sands and shallow water table are susceptible to contraction under shear, pore-pressure generation, softening and liquefaction due to earthquakes. The geologic conditions favorable for lateral spreading are gentle surface slope, shallow water table, liquefiable soils and are found along waterfronts in alluvial or deltaic deposits, (Youd and Hoose 1976). Tension cracks, ground fissures and sand boils are common indications of liquefaction and are found in the regions affected by lateral spread (Rauch 1997).

Lateral spreads occur more frequently in comparison to flow liquefaction ground failure. Flow liquefaction generally involves very large down-slope movement of the soil mass and has far more severe effects as compared to lateral spreading. The conditions for lateral spreading as discussed by Bartlett and Youd (1995) generate low confining pressures and lower static shear stresses than flow liquefaction conditions. Low confining pressure results in a dilative behavior of the soil and the soil undergoes cyclic mobility, when the static shear stress is less than the shear strength of the liquefied soil. The deformations (i.e. lateral spreading) produced by cyclic mobility are driven by both cyclic and static shear stresses and develop incrementally during an earthquake. The amount of lateral displacement typically ranges from a few centimeters to several meters (Bartlett and Youd 1995).

An important phenomenon in lateral spreading is the upward movement of the pore water. In a liquefied state, the soil grains sink under gravity and the liquefied soil densifies near the bottom and loosens near the top. Lateral spreading occurs as blocks of the soil slide over the weaker soil near the top of the liquefied soil deposit. Stark and Mesri (1992) suggested partial drainage in the liquefaction case histories during back-calculation of the shear strength of liquefied soils. Drainage of excess pore pressures might considerably reduce the magnitude of lateral spread displacements.

Post-liquefaction, it is important to anticipate the ground displacements due to lateral spreading type of ground failure. The surface displacements due to lateral spreading type of ground failure help to evaluate the impact of liquefaction. Several investigators have proposed methodologies to evaluate the lateral spreading surface displacements. Rauch (1997) presented a broad classification of the methods to evaluate the lateral spreading displacements. The classification involved grouping the methods into three models: (1) Empirical models; (2) Simplified Analytical models; and (3) Finite element models. Some of the empirical models and simplified analytical models are described below. The discussion of the finite element models is beyond the scope of this literature review.

2.2.1 Empirical Models

Empirical models are developed from the lateral spreading displacement case histories. Moreover, they are easier to use as compared to analytical and finite element models. Some of the empirical models are discussed below:

Hamada et al. (1986) proposed an empirical model to evaluate the lateral spreading displacements. The model is based on the lateral spreading studies conducted in the cities of Niigata and Noshiro, Japan during the 1964 Niigata and 1983 Nihonkai-Chubu earthquakes

respectively. The observations for ground deformations were based on the pre-earthquake and post-earthquake aerial photographs of the damaged area. As a part of the approach to develop the model, Hamada et al. (1986) divided the lateral spread into discrete blocks. Averaging the horizontal displacement, thickness of the liquefied layer and the ground slope within each block, resulted in the empirical equation

$$D = 0.75 \cdot \sqrt[2]{H} \cdot \sqrt[3]{\theta} \tag{2.1}$$

where, D is the displacement (m) and H is the thickness (m) of the liquefied soil and θ is the largest of the gradient (%) of the slope of the base of liquefied layer or surface topography. (Bartlett and Youd 1995)

Youd and Perkins' LSI model is based on the relationship between the earthquake source parameters and severity of the ground motions (Rauch 1997). Youd and Perkins (1987) suggested that horizontal displacements are a function of the earthquake magnitude and the duration of the ground motion and introduced LSI – "liquefaction severity index", to estimate the maximum horizontal ground displacement due to lateral spreading. Due to limited strong motion records from the case histories, LSI empirically is expressed in terms of earthquake magnitude (M) and the logarithm of the distance (R) from the source of the earthquake. The empirical equation can be expressed as:

$$\log(LSI) = -3.49 - 1.86 \log(R) + 0.98 M_w \tag{2.2}$$

where, LSI is the maximum expected horizontal displacement in mm; R is the Joyner-Boore distance in km and M_w is the moment magnitude of the earthquake.

Bartlett and Youd (1995) used a large database of lateral spreading case histories to develop an empirical model for computing lateral spreading ground displacements. The model is developed by fitting equations to displacement vectors from lateral spreading case histories in Japan and western USA (Rauch 1997). Bartlett and Youd developed two empirical models: a free face for sites near steep banks and a ground slope model for gently sloping sites.

For free-surface sites, displacements can be computed from:

$$\log D_H = -16.366 + 1.178M_w - 0.927 \cdot \log R - 0.0133 \cdot R + 0.657 \cdot \log W + 0.348 \cdot \log T_{15} + 4.527 \cdot \log(100 - F_{15}) - 0.0922(D_{50})_{15} \quad (2.3)$$

For gently sloping sites, displacements can be computed from:

$$\log D_H = -16.366 + 1.178M_w - 0.927 \cdot \log R - 0.0133 \cdot R + 0.429 \cdot \log S + 0.348 \cdot \log T_{15} + 4.527 \cdot \log(100 - F_{15}) - 0.0922(D_{50})_{15} \quad (2.4)$$

Where D is the horizontal displacement (m), M_w is the moment magnitude of the earthquake, and R is the nearest horizontal distance (km) to the seismic energy source of fault rupture. T_{15} is the thickness (m) of saturated cohesionless soils (excluding soils deeper than 20 m or with $\geq$ 15% clay content) with $N_{1\text{-}60} \leq 15$, ($N_{1\text{-}60}$ is the standard SPT blow-count). F_{15} is the average fines content (% finer than 0.075 mm) in T_{15}, and $(D_{50})_{15}$ is the average D_{50} grain size (mm) in T_{15}.W is the ratio of the height of the free surface to the horizontal distance between the base of the free face and the point of interest and S is the ground slope in percent.

Rauch and Martin (2000) suggested regrouping the displacement vectors associated with liquefaction induced lateral spreads to denote the lateral ground displacement. The regional average model developed has four input parameters all related to the earthquake ground motion and is expressed as:

$$D = (D_R - 2.21)^2 + 0.149 \; and$$
$$D_R = (613 \cdot M_w - 13{,}9R_f - 2420A_{\max} - 11.4T_d)/1000 \quad (2.5)$$

Where D is the average horizontal displacement (m); R_f is the shortest horizontal distance to the fault rupture; M_w is the moment magnitude; A_{max} is the peak ground acceleration (g) and T_d is the duration (sec) of the strong ground motion (>0.05g).

Bardet et al. (1999) developed a four-parameter model to provide an approximate measure of the liquefaction induced lateral ground displacements. The model developed is independent of the soil properties such as mean grain size and fines content. The model has the following equation:

$$\log(D + 0.01) = -6.815 - 0.465^F + 1.017M - 0.278\log(R) - 0.026R + +0.497^F \log(W) + 0.464^G \log(S) + 0.558\log(T_{15}) \quad (2.6)$$

where D is the average horizontal displacement (m); R is the nearest horizontal distance (km) to the seismic energy source or fault rupture; M is the moment magnitude; S the slope (%) of ground surface; W is the free face ratio (%) and T_{15} is the thickness (m) of saturated cohesionless soils with $N_{1\text{-}60}$ <15. The equation applies to free-face and ground-slope cases. In cases with free-face, the coefficients with superscript G is set equal to zero, while in the ground-slope cases, the coefficients with superscript F are set to zero.

2.2.2 Simplified Analytical Models

Simplified Analytical procedures are mostly based on Newmark's sliding block model which assumes that the slope deformations are driven by seismic base accelerations. Newmark (1965) proposed a model to compute ground surface displacements, based on the analogy of a sliding block. As per the model, the soil mass begins to move relative to the base soil, when the sum of the static and dynamic forces exceed the shear resistance from the soil. The

condition when the soil mass begins to slip is described in terms of yield acceleration (a_y). The displacement of the soil mass relative to the base soil initiates when yield acceleration, (a_y) is exceeded and continues until the soil mass and base soil move with the same velocity. Newmark's sliding block model uses coupled and decoupled methods to compute the displacements due to lateral spreading. Idriss and Boulanger (2008) stated that: *"The differences in the displacements computed via coupled and decoupled methods depends on the characteristics of the soil mass and the ground motions."* A detailed description of these methods is beyond the scope of this literature review.

2.2.3 Finite Element Models

A variety of finite element models have been used to compute the ground displacements due to lateral spreading ground failure. Rauch (1997) suggests that a finite element model would need to simulate complex phenomena that include seismic excitation, softening of the soil, pore pressure build-up, possible progressive failure and deformations. The formulation of these phenomena would produce a highly non-linear model. Finite element models serves as a powerful tool for computing lateral displacements and to investigate complex mechanisms that are difficult to assess through the aforementioned models (Idriss and Boulanger 2008). The finite element models have the disadvantage of requiring a high degree of expertise to understand and run the simulations. The biggest disadvantage of finite element models is the complexity involved in simulating the behavior of liquefied soil. A detailed description of the type of finite element models is beyond the scope of this literature review.

2.3 Slope stability analysis of liquefied soils

Duncan and Wright (2005) suggested a reduction in the stability of the slope due to reduction in the shear strength of the soil. The stability of a slope following an earthquake can be evaluated depending whether or not liquefaction has occurred (Duncan and Wright 2005). This section of the literature review covers a review of slope stability analyses of soil that liquefied and suffered a flow liquefaction ground failure. It discusses the slope stability analysis procedures suggested by Olson (2001) and a case history in support of the procedures discussed.

Olson (2001) suggested that if liquefaction is triggered, a post-triggering stability analysis of the slope must be conducted using the pre-failure geometry to determine whether the static shear forces are greater than the available shear resistance of the slope. Olson (2001) presented thirty-three flow failure case histories to back-calculate the shear strength of the liquefied soils. In order to get an estimate of the liquefied shear strength ratio, Olson (2001) discussed three types of stability analysis: (1) simplified stability analysis of post-failure geometry; (2) rigorous stability analysis of post-failure geometry; and (3) stability analysis considering kinetics of failure mass movements. The selection of the type of stability analysis depended on the amount of information available from the case history. The information consisted of details about several variables including unit weight of the soil, loading conditions, subsurface stratigraphy, cause of sliding and shape of the slip surface.

For the cases with minimum available information, a simplified stability analysis was conducted to estimate the liquefied shear strength ratio. Ishihara (1990) developed the method for simplified stability analysis of a slope, assuming (1) the ground surface and the surface of the flowed material are parallel; (2) side forces are equal, opposite and collinear; and (3) the shear strength mobilized

at the moment the failed mass comes to rest is the liquefied shear strength. As shown in Figure 2.1, if the average thickness of the liquefied layer (flowed material) is H and a unit weight of γ_t, then force equilibrium in the direction of flow shows that

$$s_u(liq) = \gamma_t \cdot H \cdot sin\alpha \cdot cos\alpha \tag{2.7}$$

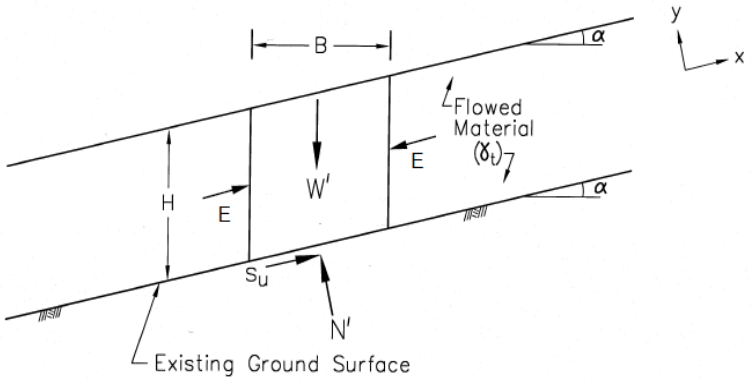

Figure 2.1. Schematic force diagram for simplified slope stability analysis (from: Olson 2001). Used under *fair use* 2013

where, α is the angle of inclination of the sliding surface and the flowed material to horizontal (Olson 2001). The above mentioned equation was used to estimate the values of the liquefied shear strength for cases histories with minimum information.

Olson (2001) performed rigorous slope stability analysis on 21 case histories that presented sufficient information, to back-calculate the liquefied shear strength ratio. The rigorous stability analysis was performed in UTEXAS3 (Wright 1992), using Spencer's method of slope analysis. This method of slope stability analysis required an accurate estimation of pre-failure vertical effective stress (σ'_{vo}). Olson (2001) examined the case histories and assumed the initial failure surface to pass approximately through the center of the zone of liquefaction. This analysis involved a complex procedure of dividing the post-failure sliding surfaces into a number of segments. The

pre-failure vertical effective stress (σ'_{vo}) is determined for each segment in the liquefied soil and was assigned to the corresponding segment in its post-failure position. Figure 2 shows the post-failure sliding surface segments. Olson (2001) concluded that rearranging the positions of the post-failure sliding surface segments, only has a marginal effect on the back-calculated liquefied shear strength. Figure 2.2 explains the analysis for the flow failure from Lower San Fernando Dam case history.

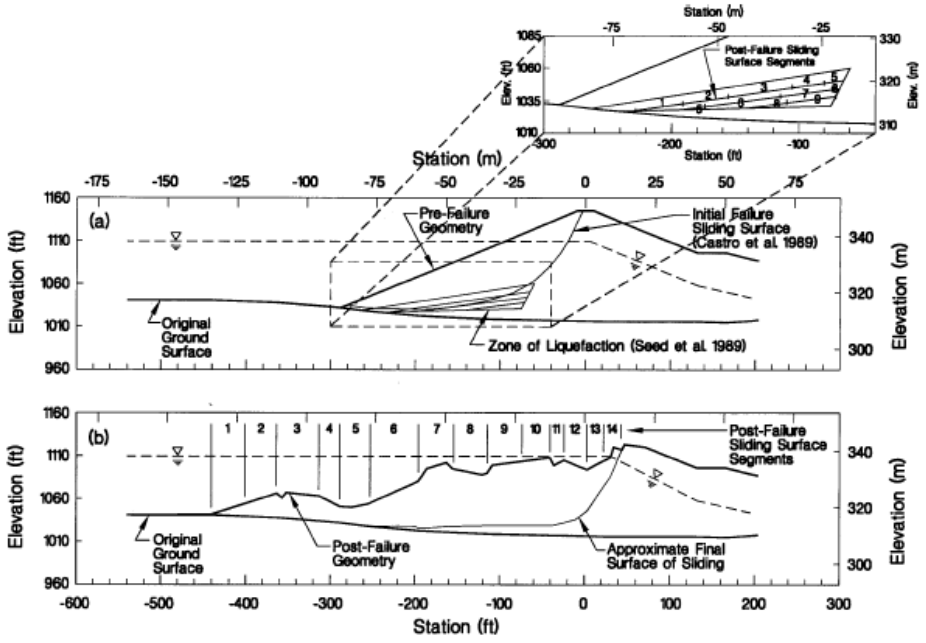

Figure 2.2. Simplified pre-failure and post-failure geometry of Lower San Fernando Dam (from: Olson 2001). Used under *fair use* 2013.

The analysis allowed for a variation in pre-failure vertical effective stress (σ'_{vo}), within the zone of liquefaction to be reflected in liquefied shear strengths along the final sliding surface. Based on detailed analysis of the information from the case histories, Olson (2001) assigned shear strengths for the soils for each of the case histories. The liquefied shear strength ratio was varied until a factor of safety of unity was achieved.

The thirty-three flow failure case histories back-analyzed by Olson (2001) included the Calaveras Dam failure in California, USA. The Calaveras dam was constructed using hydraulic fill for the core and interior portions of the shells and uncompacted dumped fill for the majority of the upstream and downstream shells. On March 24, 1981 about 600,000 $m^3$of material from the central to the eastern side of the upstream slope of the dam failed and slid into the reservoir. The maximum height of the dam was 61 m and the depth of the reservoir was approximately 23 m, at the time of failure. Hazen (1918) and Hazen (1920) described the failure of Calaveras Dam, as well as the surveys conducted in an attempt to explain the post-failure geometry (Figure 2.3). Hazen (1918) indicated that:

> *"The men who saw the dam go state that at first the whole mass seemed to move forward as a unit. Afterward it seemed to separate, and the parts that were farthest back stopped, while those that were further advanced continued to move forward…the material was carried forward on a good lubricant, and that the lubricant first became used up or expelled near the center of the dam and left the higher parts of the dam on solid bottom while there was still lubricant to carry forward the lower and more advanced portions."*

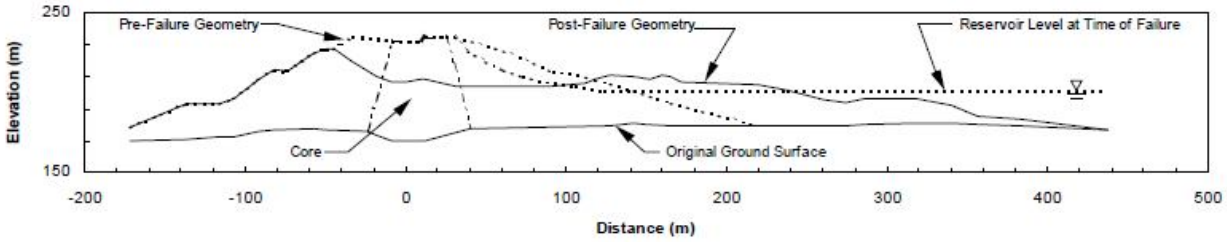

Figure 2.3. Pre- and post-failure geometry of Calaveras Dam (from Olson 2001). Used under *fair use* 2013.

Based on Hazen (1918) investigations, Olson (2001) suggested that the liquefied shell soil (lubricant) near the center of the dam had a higher shear strength than the liquefied shell soil farther from the center of the dam. Through thorough post-failure investigations, Hazen (1918) speculated that the failure initiated in the sandy shell material and suggested that:

"As water pressure is increased, the pressure on the edges is reduced and the friction resistance of the material becomes less. If the pressure of the water in the pores is great enough to carry all the load, it will have the effect of holding the particles apart and of producing a condition that is practically equivalent to that of quicksand…A sharp blow, as with the foot, however, liquefies a certain volume and makes quicksand. The condition of quicksand lasts for only a few seconds until the surplus water can find its way out. When this happens the grains again come to solid bearings and stability is restored. During a few seconds after the sand is struck, however, it is almost liquid, and is capable of moving or flowing or of transmitting pressure in the same measure as a liquid…The conditions that control the stability or lack of stability in quicksand may also control the stability or lack of stability of materials in dams…It may be that after the first movement there was some readjustment of the material in the toe [upstream slope] which resulted in producing temporarily this condition of quicksand, and which destroyed for a moment the stability of the material and facilitated the movement that took place."

Figure 2.4 shows the post-failure sliding surface segments used for stability analyses. No penetration tests data were available for the case history. Olson (2001) estimated the "representative" SPT and CPT penetration resistances from an estimate of the relative density and vertical effective stress using Holtz and Gibbs (1979) and Robertson and Campanella (1983) correlations. An approximate relative density of 35% and an average vertical effective stress of 307.5 kPa, yielded "representative" values of $(N_1)_{60}$ and q_{c1} of approximately 8 and 5.5 MPa.

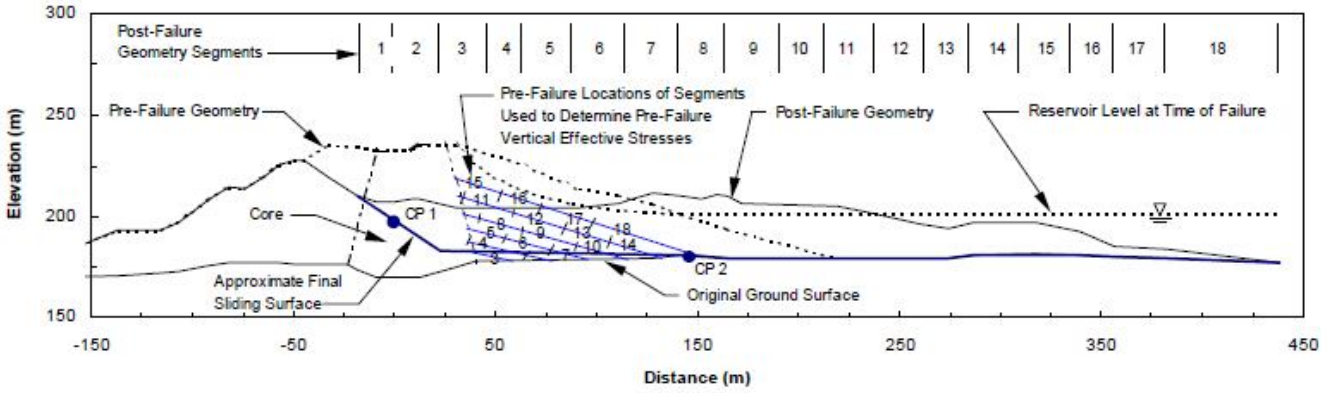

Figure 2.4. Post-failure geometry of Calaveras Dam used for liquefied shear strength ratio analyses (from: Olson 2001). Used under *fair use* 2013.

Olson (2001) reproduced the post-failure geometry of the dam, based on the examination of the post-failure geometry as described by Hazen (1920). The material that did not liquefy was assigned a ϕ' between 30^o and 35^o. Rigorous slope stability analysis was performed using the post-failure sliding surface. The liquefied strength ratio was estimated as 0.012, with a possible range from 0.007 to 0.033, with the pre-failure vertical effective stress equal to 307.5 KPa (Olson 2001).

Thus, Olson (2001) suggested a methodology of dividing the post-failure sliding surface into segments and based on the length of the post-failure segments, corresponding lengths of liquefied soils are defined within the pre-failure geometry.

2.4 Use of Bayesian Techniques in Geotechnical Engineering

Uncertainty is commonly encountered in geotechnical engineering. Over the years, geotechnical engineers have spoken and written about the importance of recognizing the uncertainties and incorporating them into the design procedure. Casagrande's well known, Terzaghi lecture (1965) was specifically about "calculated risk" (Whitman 2000). Casagrande, in his lecture stated that:

> *"(a) The use of imperfect knowledge, guided by judgment and experience, to estimate the probable ranges for all pertinent quantities that enter into the solution of the problem.*
>
> *(b) The decision on an appropriate margin of safety, or degree of risk, taking into consideration economic factors and the magnitude of losses that would result from failure."*

This section of the literature review discusses the use of Bayesian updating in regular geotechnical engineering practice and applications.

Engineering decisions are usually made in the face of some uncertainty because some future events, such as the magnitude of a potential earthquake or the settlement of a foundation due to settlement of a near-by foundation or the strength of the soil post liquefaction, cannot be stated with certainty. Similarly, the outcome of any design or maintenance option cannot be predicted with certainty. Use of probability methods, such as Bayesian updating, in decision making allows the various uncertainties and their effects to be accounted for in a systematic manner. Bayesian updating technique begins with a prior probability or a prior probability distribution function. Christian (2004) defined this process as selecting the state of nature. The observations then update the probability of the state of nature. Any further addition of the data makes possible a further update and hence a better estimate of the state of nature.

Fenton (1997) discusses Bayesian probability procedures providing a logical bias for revising engineer's judgment. Fenton (1997) in his report discussed the use of observational method to help engineers deal with uncertainty or variability in site conditions and performance behavior of the structure. The engineer selects a hypotheses about the site conditions and field observations are gathered towards the correct hypothesis. For continuous random variables, the updated probability of a given hypothesis (H), based on the observation (E), is determined as:

$$P'' (H) = k\, L (E \mid H)\, P (H) \tag{2.8}$$

where, P (H) represents the estimated probability of hypothesis prior to observation; L (E | H) is referred to as the likelihood of the hypothesis and k is the normalizing constant such that the updated probability will be 1.0.

The following example, adopted from Fenton (1997), depicts the importance of Bayesian updating in general engineering applications. The example is the interpretation of the soil profile from the borehole during the characterization phase of a site. Post field characterization a geotechnical engineer can face the question of "the probability of finding a specific soil at a particular depth given that the soil has been found or not found at some other depth?" The probability can be evaluated using Bayesian updating technique. In the example mentioned, the engineer investigating the site will have a sound knowledge of the geology of the area. Use of Bayesian updating will combine the engineer's judgement with the results of site characterization to estimate the "likelihood" of presence of a soil at a particular depth. Thus, using the Bayesian updating methodology, we overcome or at least "reduce" the uncertainty in our knowledge of the hypothesis.

Summary

A literature review has revealed the following deficiencies in the state of knowledge:

1. Limited number of studies have included the lateral spreading case history to estimate the liquefied shear strength. Olson and Stark (2002) included about 33 liquefaction failure case histories to estimate the liquefied shear strength ratio. However, it did not include any lateral spreading case histories.
2. There are a number of practical difficulties in using the existing methods to estimate the liquefied shear strength. In addition, the laboratory testing is an expensive and difficult means to estimate the liquefied shear strength.
3. A very few geotechnical engineering case studies have included the probabilistic methods to incorporate the uncertainties in the parameters involved in the study. The number of case

studies are further reduced where Bayes' theorem for updating probabilities given additional information/observations is used.

The research presented in this thesis includes a liquefaction induced lateral spreading case history to evaluate the liquefied shear strength of the soil using back-analysis procedure. The study presented involves use of Bayesian updating technique to incorporate the uncertainty in selecting the ground acceleration that caused the earthquake and to get a close approximate of the liquefied shear strength of the soils.

References

Bardet, J.P. et al. (1999). "Large-scale modeling of liquefaction induced ground deformation, Part I: A four-parameter MLR model". *Proc. of the 7th U.S.-Japan Workshop on Earthquake Resistant Design of Lifeline Facilities and Countermeasures against soil liquefaction.*, Technical Report MCEER-99-0019, Seattle, WA.

Bartlett, S. F., and Youd, T. L. (l995). "Empirical prediction of liquefaction-induced lateral spread" *J. Geotech. Engrg*., ASCE, 121(4), 316-329.

Christian, J. (2004). "Geotechnical Engineering Reliability: How Well Do We Know What We Are Doing?." *J.Geotech.Geoenviron.Eng*.,130(10), 985-1003.

Duncan, J. M., and Wright, S.G. (2005). *Soil Strength And Slope Stability*, John Wiley & Sons.

Fenton, G.A., (1997)."Probabilistic methods in Geotechnical Engineering." *Proc. GeoLogan Conference*, Logan, Utah.

Hamada, M., Yasuda, S., Isoyama, R., and Emoto, K. (1986). "Study on liquefaction induced permanent ground displacements." *Association for the Development of Earthquake Prediction in Japan*, Tokyo, Japan.

Hazen, A. (1918). "A study of the slip in the Calaveras Dam." *Engineering News-Record*, 81(26), 1158-1164.

Hazen, A. (1920). "Hydraulic-fill dams." *Transactions of the American Society of Civil Engineers*, Paper No. 1458, 1713-1821 (including discussions).

Holtz, W.G. and Gibbs, H.J. (1979). "Discussion of "SPT and relative density in coarse sand." *J.Geotech.Engrg*, ASCE, 105(GT3), 439-441.

Idriss, I. and Boulanger, R. W. (2008). *Soil liquefaction during earthquakes*, Earthquake Engineering Research Institute.

Ishihara, K., Yasuda, S. and Yoshida, Y. (1990). "Liquefaction induced flow failure of embankments and residual strength of silty sands." *Soils and Foundations*, 30(3), 69-80.

Ji, C. and Zeng, Y. (2007). "Preliminary Result of the Aug 15, 2007 Mw 8.0 Coast of Central Peru Earthquake". *Web report (http://earthquake.usgs.gov/eqcenter/eqinthenews/2007/us/2007/gbcv/finite_fault.php).*

Newmark, N.M. (1965). "Effects of earthquakes on dams and embankments." *Fifth Rankine Lecture, Geotechique*, Vol. 15, No. 2, June, pp. 139-159.

Olson, S.M., (2001). "Liquefaction analysis of level and sloping ground using field case histories and penetration resistance." *PhD thesis.*, University of Illinois Urbana Champaign, Urbana, Illinois.

Olson, S. M., & Stark, T. D. (2002). "Liquefied strength ratio from liquefaction flow failure case histories". *Canadian Geotechnical Journal*, 39(3), 629-647.

Poulos, S. J., Castro, G., and France, J. (1985). "Liquefaction evaluation procedure". *J. Geotech. Engrg.*, 111(6), 772–792.

Rauch A.F. (1997) "EPOLLS: An empirical method for predicting surface displacements due to liquefaction-induced lateral spreading in earthquakes". *PhD thesis*, Virginia Polytechnic Institute and State University; 1997; 333.

Rauch, A. F., and Martin, J. R., II. (2000). ''EPOLLS model for predicting average displacements on lateral spreads.'' *J. Geotech. Geoenviron. Eng.*, 126(4), 360–371.

Robertson, P.K. and Campanella, R.G. (1983). “Interpretation of cone penetration tests. Part I: Sand.” *Canadian Geotechnical Journal*, 20(4), 718-733.

Seed, H.B., and Idriss, I.M. (1982). “Ground Motions and soil liquefaction during earthquakes”. *Monograph, Earthquake Engineering Research Institute*, Berkeley, California, 134 pages

Seed, H. (1987). “Design Problems in Soil Liquefaction”. *J.Geotech.Engrg*., 113(8), 827-845

Seed, R. B. and Harder, L. F. (1990). “SPT-based analysis of cyclic pore pressure generation and undrained residual strength”. *Proc., H.B. Seed Memorial Symp., Vol. 2,* BiTech Publishers Ltd, Vancouver, B. C., Canada.

Stark, T. D., and Mesri, G. (1992). “Undrained shear strength of liquefied sands for stability analysis”. *J. Geotech. Engrg*., ASCE, 118(11),1727-1747.

Stark, T.D., Olson, S.M., Kramer S.L., Youd, T.L. (1998). “Shear Strength of Liquefied Soil”. *Proc.,Geotechnical Earthquake Engineering and Soil Dynamics-III*. pp. 313-324. Seattle Washington USA.

Tavera, H., Bernal, I., Strasser, F.O., Arango-Gaviria, M.C., Alarcón, J.E. and Bommer, J.J. (2008)”. Ground motions observed during the 15 August 2007 Pisco, Peru, event”. *Bulletin of Earthquake Engineering*.

Whitman, R. (2000). “Organizing and Evaluating Uncertainty in Geotechnical Engineering.” *J. Geotech. Engrg*., ASCE, 126(7), 583-593.

Wright, S.G. (1992). *UTEXAS3: A computer program for slope stability calculations*. Geotechnical Engineering Software GS86-1, Dept. of Civil Engineering, University of Texas, Austin.

Youd, T. L., and Hoose, S. N. (1976). “Liquefaction during the 1906 San Francisco Earthquake.” *J. Geotech. Engrg*. Div., ASCE, 112(5), 425-439.

Youd, T. L., and Perkins, D. M. (1987). “Mapping of liquefaction severity index.” *J. Geotech. Engrg.*, ASCE, 113(11),1374-1392.

Analysis of a Lateral Spreading Case History from the 2007 Pisco, Peru Earthquake *(In the process of submission)*

Abstract

On August 15, 2007, Pisco, Peru was hit by an earthquake of magnitude (M_w) = 8.0 which triggered multiple liquefaction induced lateral spreads. The subduction earthquake lasted for approximately 100 seconds and showed a complex rupture. From the geotechnical perspective, the Pisco earthquake was significant for the amount of soil liquefaction observed. A massive liquefaction induced seaward displacement of a marine terrace was observed in the Canchamana complex. Later analysis using the pre- and post-earthquake images showed that the lateral displacements were concentrated only on some regions. Despite the lateral homogeneity of the marine terrace, some cross-sections showed large displacements while others had minimal displacements. The detailed documentation of this case-history makes it an ideal case-study for the determination of the undrained strength of the liquefied soils; hence, the main objective of this research is to use the extensive data from the Canchamana Slide to estimate the shear strength of the liquefied soils. In engineering practice, the undrained strength of liquefied soil is typically estimated by correlating SPT-N values to: 1) absolute value of residual strength, or 2) residual strength ratio. Our research aims to contribute an important data point that will add to the current understanding of the residual strength of liquefied soils.

3 Introduction

On August 15 2007, at 6:40 p.m. local time (UTC/GMT: 11:40 p.m.), a large subduction interface event occurred off the coast of Central Peru. The epicenter was located about 60 km west of the city of Pisco, and about 150 km SSE of the capital city of Lima. The focus of the event was located at 13.354° S and 76.509° W as per the United States Geological Survey (USGS). The USGS estimated that the moment magnitude (M_w) of the event was 8.0, and the hypocentral depth was about 39 km. The earthquake has been referred to as the Pisco Earthquake, since Pisco was the most affected city (Figure 3.1). The Pisco earthquake was a result of the subduction process between the Nazca plate and the South American continental plate. The event occurred on a previously identified seismic gap between the rupture areas of the 1974 Lima and the 1996 Nazca earthquake (Tavera et al. 2009).

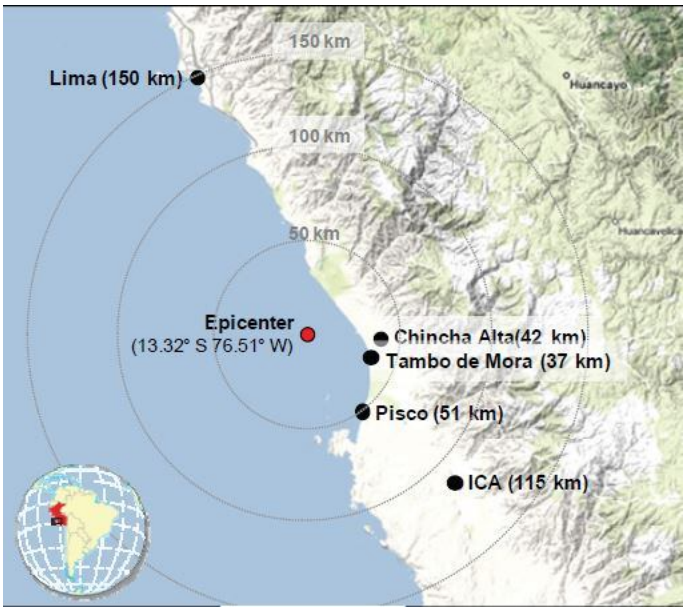

Figure 3.1. Epicenter and overview of the affected area from the 2007 Pisco Earthquake (from: MAE 2008). Used under *fair use* 2013.

From the geotechnical perspective, the Pisco earthquake was significant for the amount of observed soil liquefaction and the considerable damage to the urban areas and civil infrastructure. A significant amount of damage was caused by differential settlements, landslides, and lateral spreading. Observations in the field revealed multiple cases of lateral spreading in the earthquake affected region (i.e. along the coast of Peru). Notable liquefaction-induced damage included a massive lateral spread of a marine terrace in the region of Canchamana (2.5 km north of Tambo de Mora, (see Figure 3.1). A maximum vertical displacement of 3.0 m was observed in the Canchamana area along the interface between the marine terrace deposits and an older marine terrace (the Canete Formation). Lateral displacements which added to about 5.0 m in places were observed in the field, as well as numerous ground cracks parallel to the sea-coast with widths up to 1.0 m.

The undrained shear strength of the liquefied soil is an important parameter and its evaluation is one of the challenging problems in geotechnical engineering. Several researchers have proposed methodologies to estimate the shear strength of the liquefied soils. In general engineering practice, the most widely used procedures are those developed by Poulos et al. (1985), Seed (1987), Seed and Harder (1990), and Stark and Mesri (1992). However, there are a number of practical challenges and uncertainties in using the above mentioned methodologies to estimate the liquefied shear strength. The liquefaction induced lateral spreading ground failure in Canchamana provides a reasonable amount of information to estimate the undrained shear strength of the soil post-liquefaction. A back-analysis procedure on the extensive data from the Canchamana complex is presented in this work. The objective of the back-analysis is to evaluate the range of the undrained shear strength of the liquefied soils. The relationship proposed by Olson

and Stark (2002) to estimate the liquefied shear strength ratio from SPT penetration resistance is adopted.

The paper first discusses the data collection and the observations made by the reconnaissance team, followed by a section on interpreting the damage caused by the Pisco earthquake, concentrating on the lateral spreading features. The study then provides a brief description of the proposed methodology to estimate the undrained shear strength of the liquefied soils. The core of the proposed method is the back analysis procedure that incorporates the Bayesian Updating technique.

3.1 Data Collection

The data used in this study was collected in three different stages. An initial reconnaissance studied liquefaction features shortly after the earthquake and identified the Canchamana lateral spread complex. A larger field exploration work was conducted about 2.5 years later; this work included geotechnical characterization of the site as well as the development of a detailed digital elevation model using land based Light Detection and Ranging Radar (LiDAR) techniques. Finally, a third stage included the compilation of satellite imagery to estimate post-earthquake displacements at the site. In this section, we describe each of the data collection stages along with the relevant results.

3.1.1 Reconnaissance observations

In response to the 2007 Pisco earthquake event, the Geotechnical Earthquake Engineering Reconnaissance (GEER) organization, with funding from the National Science Foundation (NSF), organized a reconnaissance team to investigate the geotechnical engineering aspects of the earthquake. The earthquake spawned a wide variety of liquefaction failures. The reconnaissance

team arrived in Peru on August 20, 2007 and visited the cities of Lima, Paracas, Pisco and Ica and other smaller coastal towns. The observations of the reconnaissance team are summarized in a GEER Report (GEER 2007).

The most striking liquefaction induced failure was a lateral spread complex in the region of Canchamana. This feature is the focus of this study. Figure 3.2 represents a sketch of the cross-section at Canchamana showing massive displacement of the marine terrace. A vertical offset between the marine terrace and the Canete Formation and cracks filled with ejecta were some of the features observed in the field immediately after the earthquake. Local fishermen reported a slight bulge near the coastline that lead to a retreat of the coastline; however, the reconnaissance team was unable to verify this feature.

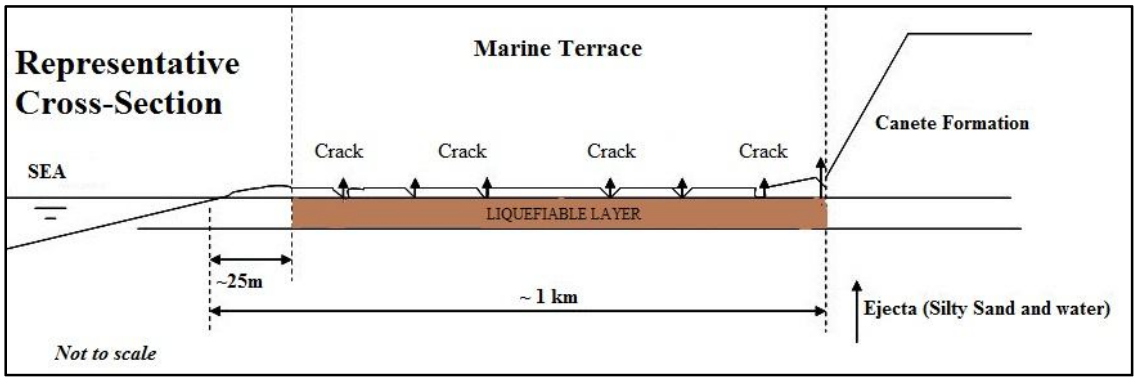

Figure 3.2. Sketch of the cross-section at Canchamana illustrating the massive displacement of the marine terrace (from: GEER 2007). Used under *fair use* 2013.

Apart from the damage in the marine terrace, some of the striking liquefaction-related features explored in the field by the reconnaissance team included a 400 m long slope failure of an approximately 50 m high steep faced slope near the Canchamana site; foundation failures of various single and double story buildings in Tambo de Mora, in some cases adding up to 0.90 m of settlement; damage to highway embankments; rupture of water and sewer lines; and disruption

of port facilities. The occurrence of liquefaction at each of these sites was confirmed by presence of sand boils in the ground surface or wet sand ejecta in open cracks.

3.1.2 Field Exploration

A comprehensive field characterization study was completed in the Canchamana complex about 2.5 years after the earthquake. The field investigation team was comprised by researchers from the Universidad Nacional de Ingenieria del Peru (UNI), the University of Arkansas, Drexel University, and Washington State University. The composition of the teams is listed in Appendix I. The field exploration included a series of Standard Penetration Tests (SPT), shear-wave velocity measurements, and soil classification and index testing using samples obtained in the field. The locations of the SPT tests were spaced so as to cover the complete extent of the marine terrace in the north-south direction and in the east-west direction. The SPT's were located along 4 east-west cross-sections that covered the region from north to south. The SPT's were carried out at multiple locations in each cross-section, the locations shifting in the east-west direction. The SPT tests were conducted by a crew from the UNI and were closely supervised by the US researchers. The borehole was advanced using a wash-boring technique. In all other respects, the test was conducted using standard protocols and equipment; hence the SPT N-values are assumed to correspond to an energy ratio of 60%, similar to common practices in the United States. Shear wave velocity (V_s) measurements were taken using the MASW technique (Wood and Cox 2012) on 19 locations along the marine terrace in Canchamana.

On average, the borings reached a depth of 10 m. Based on the laboratory tests results for liquid limit, plastic limit, and grain size distribution, most of the soil specimens were classified as SP or SP-SM as per the Unified Soil Classification System (USCS). However, at some test

locations small pockets of GP-GM, SC-SM, and SW soils were encountered. The average shear wave velocity for the entire site was calculated to be 312 m/sec.

To facilitate the matching of in-situ test data with displacement observations (discussed in the next section), the marine terrace was divided into 20 bins (Figure 3.3). These bins are approximately perpendicular to the coast line and span the entire length of the marine terrace deposits.

Figure 3.3. Overview of the affected area at Canchamana showing bin numbers, SPT and MASW test locations (Background image from Google Earth)

SPT boreholes are matched to the corresponding bins (Table 3.1). As mentioned, the SPT's were located along 4 cross-sections in the terrace and hence the field exploration results were available for 4 bins in the marine terrace.

Table 3.1. SPT test number and the corresponding bins

Bin No.	SPT test location
Bin (2)	UA-SPT-07; UA-SPT-08
Bin (3)	UA-SPT-04; UA-SPT- 05; UA-SPT-06
Bin (12)	UA-SPT-01; UA-SPT-02; UA-SPT-03
Bin (20)	UA-SPT-11; UA-SPT-15; UA-SPT-17

Figures 3.4 through 3.7 show the soil profile inferred from the SPT tests, and the corresponding SPT N-values for all the tests conducted in the marine terrace. The profiles in Figures 3.4-3.7 convey information about the soil layering at the test locations, the major soil type found in the terrace, the depth of investigation, and the location of the ground water table. The SPT profiles are used in the slope stability analyses (discussed in Section 3.6). For the purpose of the stability analyses, a profile that has uniform SPT N-values across each of the cross-sections is desired. This equivalent SPT profile is obtained using all the SPT tests at a given cross section and is defined as the arithmetic mean of all the SPT N-values at a given depth. The individual SPT N-value profiles, the equivalent profiles, and the soil classification inferred from the SPT samples and the laboratory testing are shown in Figures 3.4 through 3.7.

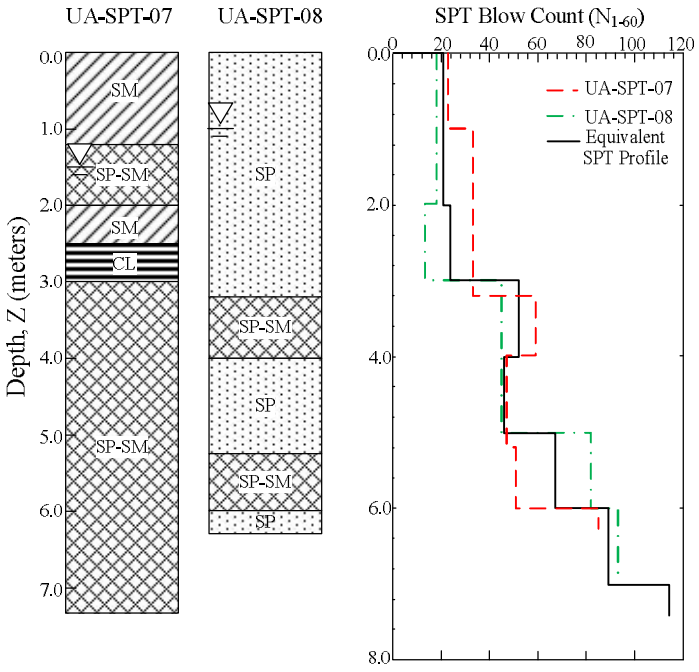

Figure 3.4. Soil profiles for Bin (2) inferred from SPT borings (left) and SPT N-value profiles (right), including the average SPT profile for the bin.

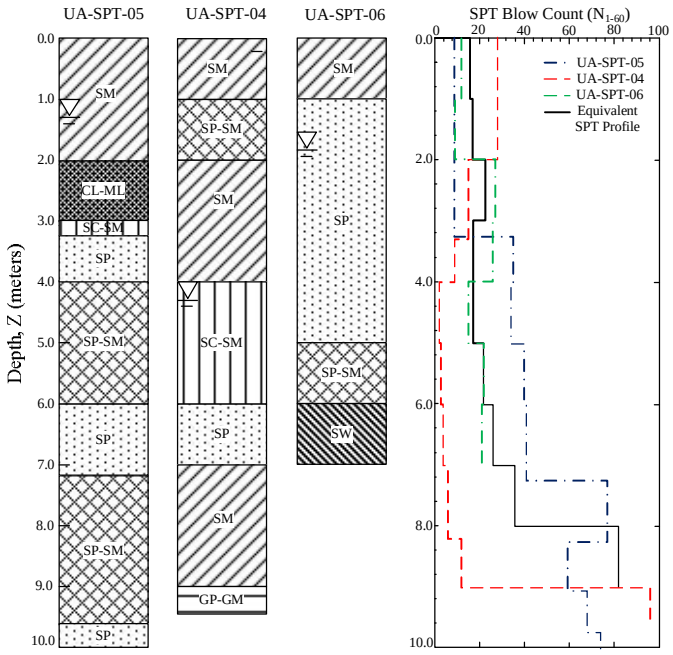

Figure 3.5. Soil profiles for Bin (3) inferred from SPT borings (left) and SPT N-value profiles (right), including the average SPT profile for the bin.

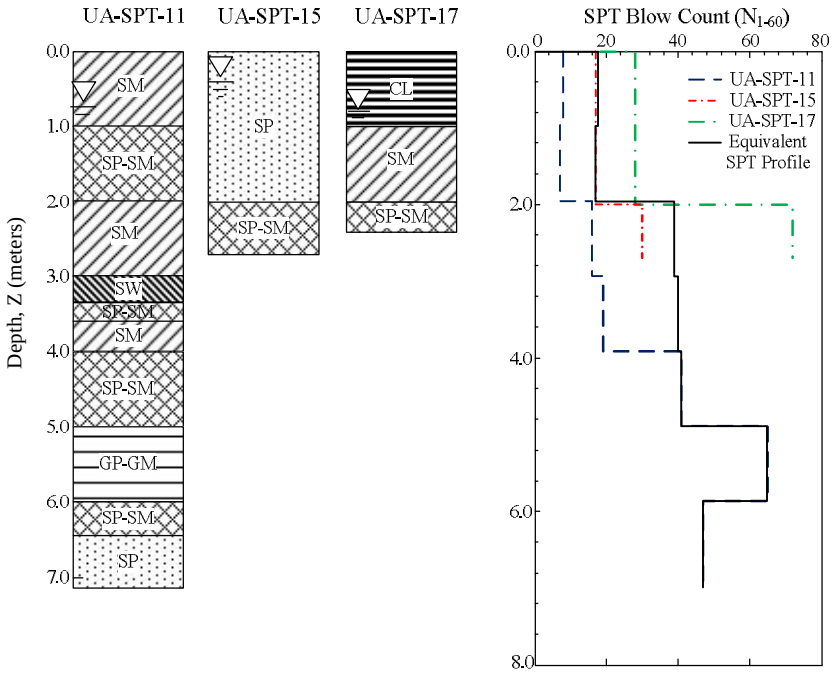

Figure 3.6. Soil profiles for Bin (20) inferred from SPT borings (left) and SPT N-value profiles (right), including the average SPT profile for the bin.

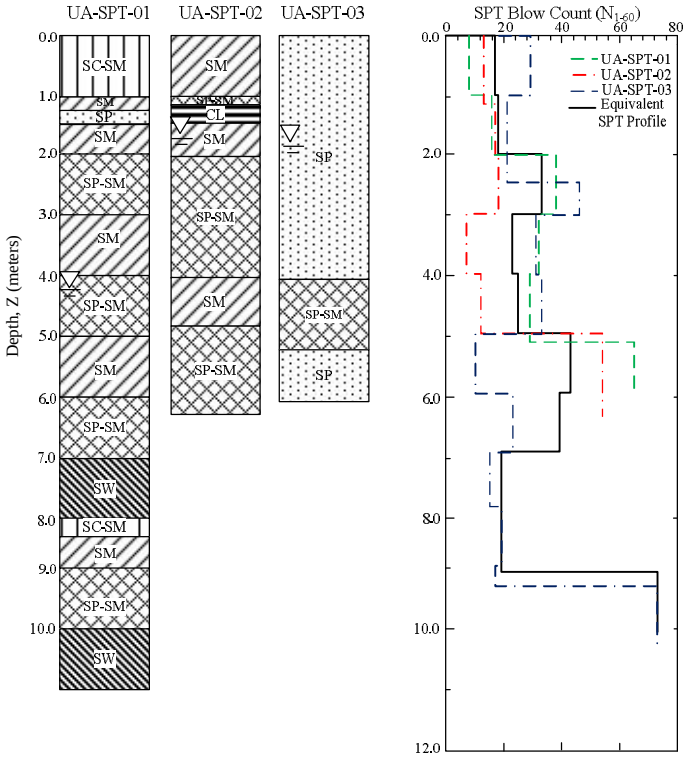

Figure 3.7. Soil profiles for Bin (12) inferred from SPT borings (left) and SPT N-value profiles (right), including the average SPT profile for the bin.

3.1.2.1 Remote Sensing Analyses

A detailed measurement of the topography of the site was obtained using a LiDAR survey. Results from the LiDAR survey were turned into a Digital Elevation Model (DEM) of the affected region (Figure 3.8). The DEM produced using LiDAR data offered the advantage of better horizontal and vertical resolution of the surface topography.

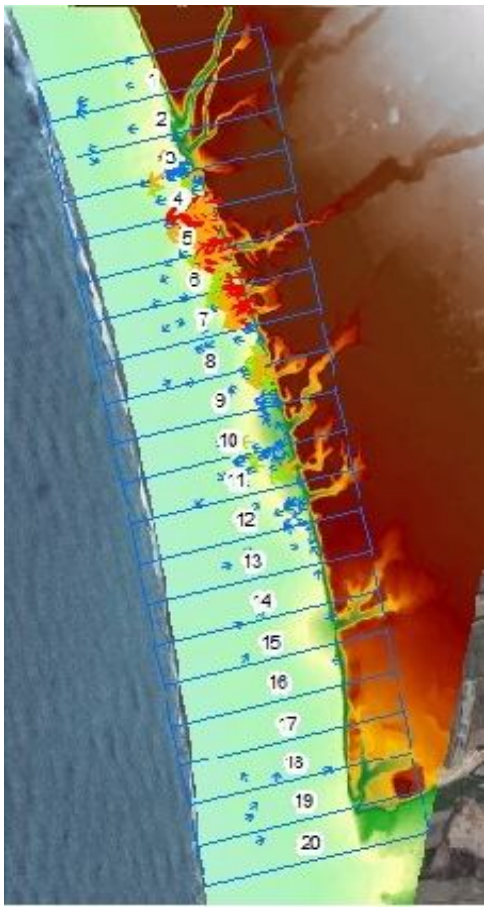

Figure 3.8. DEM map of the Canchamana lateral spread complex (Courtesy of Dr. B. Cox). The color indicates surface elevation while the vectors superposed on the map are displacement vectors estimated from comparison of pre- and post-earthquake satellite images (from: GEER 2007). Used under *fair use* 2013.

Field observations of post-earthquake displacements were obtained by the reconnaissance team briefly after the earthquake. However, the large extent of the Canchamana lateral spread

feature precluded a comprehensive post-earthquake survey. Moreover, the terrain was not conducive to accurate measurements of lateral displacements; since the surface soil was sandy, small lateral displacements were not evident near the surface. For this reason, satellite imagery from before and after the earthquake was used to estimate post-earthquake displacements. These analyses were conducted by the Center for Advanced Spatial Technologies (CAST) at the University of Arkansas. Details of these measurements are given in Section 3.4. The magnitude of the displacements were characterized by the displacement vectors recorded in each of the bins.

Figure 3.8 shows the DEM map of the complex in combination with the bins and the displacement vectors. The displacement vectors show a large spatial variability, despite the lateral homogeneity of the terrace. Multiple displacements were observed in each bin, ranging from 0~1 m (small)toabout 4 m (large). The color of the vector arrows used in the DEM map denotes the magnitude of the displacements in the region. The DEM map shows that bins (3) through (12) contain red and yellow colored vector arrows indicating large displacements. The remainder of the bins with green and blue vector arrows experienced comparatively smaller displacements.

3.2 Methodology

This section presents a back-analysis procedure to estimate the shear strength of the liquefied soils at the Canchamana site. The methodology incorporates (1) development of the cross-sections from the field exploration results, (2) classification of each bin as 'failed' and 'non-failed' based on the displacement observations in the marine terrace, (3) selection of a relationship to assign liquefied shear strength ratio to the soil layers in the built cross-sections, (4) performing seismic slope stability analysis and, (5) application of a Bayesian updating technique to get an improved estimate of the undrained shear strength of the liquefied soils. Each of the aforementioned steps are discussed below.

3.3 Development of cross sections

The first step of the methodology involves developing soil profiles for the stability analyses of the marine terrace. These cross-sections were developed using the DEM maps obtained from the LiDAR survey for ground surface topography. Soil layering was primarily based on the SPT boring logs in the marine terrace. The cross-sections were developed based on two approaches: (1) assuming an equivalent SPT profile for the entire cross-section and, (2) retaining the differences in measured SPT N-values for each borehole in the cross-sections. A detailed description of each approach is presented below.

3.3.1 Approach A: uniform profile

As a simplification of the problem the first approach adopted in the analyses was to assume that every layer in the cross-section is characterized by a single SPT N-value. The SPT blow-count variation with depth varied for every test location in the bin. To maintain uniformity in the SPT N-value for each bin, a mean SPT value (i.e.an arithmetic mean of the SPT N-values at individual test locations in the bin) was calculated. This seemed to be a reasonable approach in estimating the mean SPT N-value in the cross-section. An equivalent SPT profile shows the variation of the mean SPT N-value in the cross-section. Figure 3.9 is a representative model of the cross-section of bin (3). SPT test locations are shown along with the layering. Each layer is parallel to the surface topography. The fill in the layers in Figure 3.9 is only for representing the pattern of layering and does not represent any soil type. Similar models were constructed for the rest of the bins mentioned in Table 3.1.

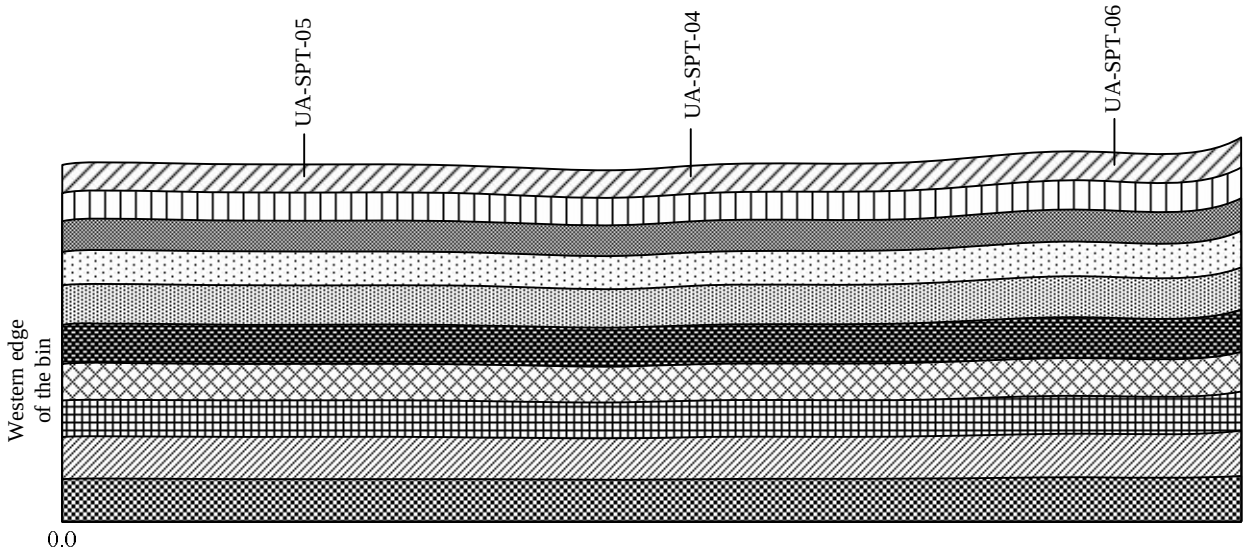

Figure 3.9. Representative model of the cross-section of bin (3) with the layering of the soil profile and the test locations. (Figure Not to Scale)

3.3.2 Approach B: non-uniform profile

In this approach, every SPT N-value recorded at a specific test location along the slope is retained in the process of developing the cross-sections for slope stability analyses. As a result, each layer in the cross-section is characterized by an SPT N-value that varies with the horizontal coordinate of the profile. The cross-section is partitioned by variable boundaries, depending on the number of test locations along the slope. This method assures a lateral variation of the SPT N-value in the cross-section. The primary reason for adopting this approach is to represent the east-to-west variability in the measured SPT N-values.

As shown in the Figures 3.4 to 3.7, we do not have any information about the change in the soil properties and layering between the test locations. To take into account this uncertainty, the variable boundary in the cross-sections was shifted by ± 25 m (distances measured away from the coast are positive). The outcome of this approach is discussed in the results section. Figure

3.10 is a representative model of the cross-section of Bin (12) showing the SPT test locations and the layering. Each layer is parallel to the surface topography.

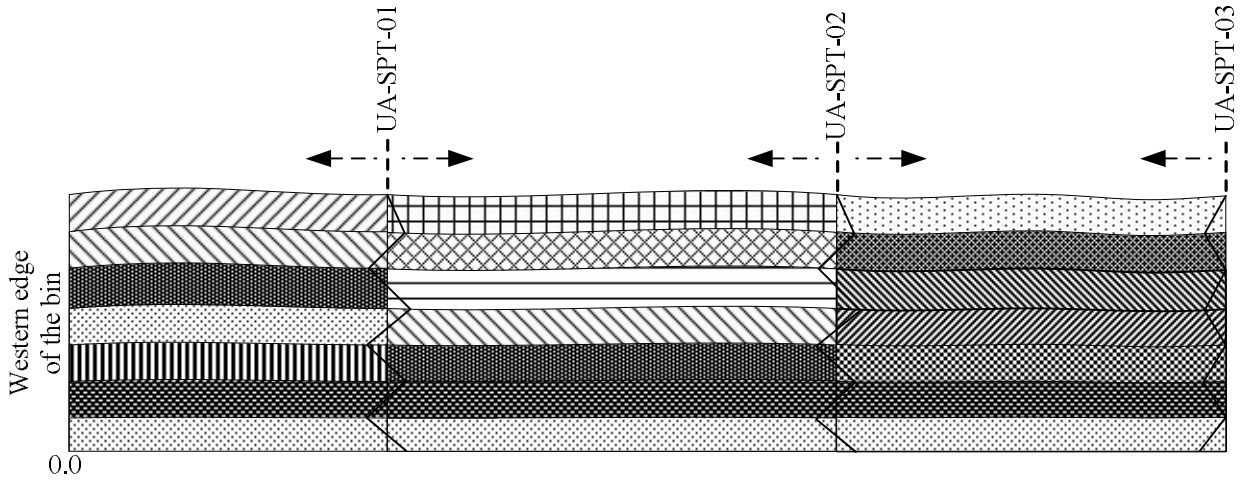

Figure 3.10. Representative model of the cross-section of bin (12) with the layering of the soil profile and the test locations. (Figure Not to Scale)

3.4 Interpretation of displacement observations

This section involves interpreting the displacements that occurred along the marine terrace due to the earthquake. As indicated previously, these post-earthquake displacements were determined from the satellite imagery before and after the earthquake by the CAST center at the University of Arkansas. Multiple displacements were observed in each bin ranging from smaller displacements (0 ~ 1 m) to larger displacements (about 4 m). For the subsequent analyses, it was convenient to associate each bin with a single displacement magnitude. For this purpose, each bin was associated with the maximum displacement observed in that bin.

Figure 3.11 shows the vectors within the 20 bins in the marine terrace. For reference, vectors with a displacement directed towards the coast would have an azimuth of -100^0. Displacements with magnitudes lower than about 1.5 m have random azimuths and do not appear to represent the type of coherent displacement that is associated with lateral spreading. The scatter

in displacement orientations below displacements of 1.5 m could possibly be associated with the resolution of the pre- and post-earthquake satellite images. Better resolution for displacement magnitudes greater than about 1.5 m explains the improved alignment of the vectors after 1.5 m. The same reasoning leads to a choice of 1.5 m as the 'threshold value' of displacement magnitude that for classifying the bins in the marine terrace as 'failed bins' and 'non-failed bins'. Bins experiencing displacements greater than 1.5 m are classified as 'failed bins', whereas the bins with displacements less than the 'threshold value' are classified as 'non-failed bins'. Table **3.2**3.2 lists the classification of the bins as 'failed' and 'non-failed' based on the magnitude of maximum displacement observed in the bins.

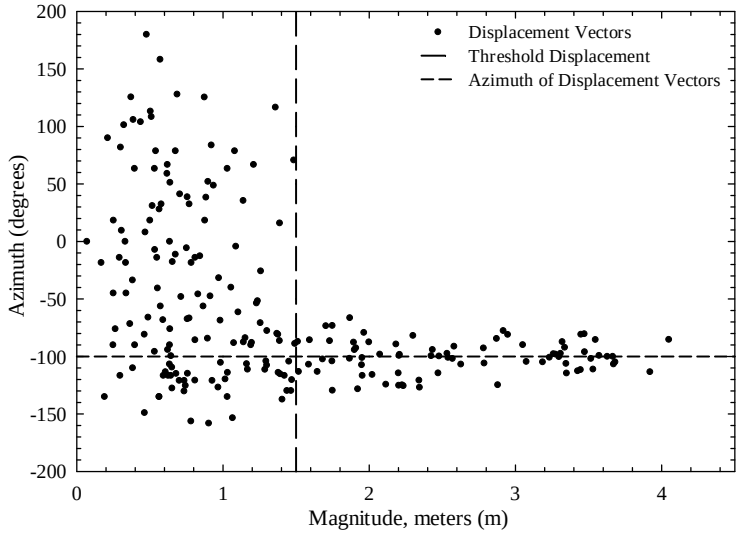

Figure 3.11. Magnitude and azimuth of the displacement vectors within the 20 bins as recorded in post-earthquake analysis. For reference, the displacement direction perpendicular to the coast has an azimuth of -100^{o}

Table 3.2. Maximum displacement in each bin and classification of the bin

Bin (No.)	Maximum Displacement (m)	Failed (*F*) or Non-Failed (*NF*)
1	1.29	NF
2	1.20	NF
3	2.02	F
4	3.36	F
5	4.05	F
6	3.92	F
7	3.53	F
8	2.20	F
9	2.53	F
10	1.89	F
11	2.34	F
12	1.52	F
13	0.87	NF
14	1.21	NF
15	1.39	NF
16	1.36	NF
17	-	-
18	0.55	NF
19	1.14	NF
20	1.48	NF

Large displacements were observed in the stretch from bin (3) to bin (12). Comparatively smaller displacements were observed in the bins south of bin (12). We note that no displacements were recorded in bin (17). It is evident from the field displacement results that bins (3) and (12) underwent failure whereas, bins (2) and (12) did not fail. This information is used in the sections ahead.

3.5 Liquefied Shear Strength Ratio

This section involves selecting an appropriate relationship to estimate the shear strength of the liquefied soils. The liquefied shear strength, which will be denoted by s_u, is the shear strength mobilized at large deformations after liquefaction triggering in saturated sandy soils. Castro (1969)

showed that post-liquefaction, sands retain some resistance to shear deformation (Stark et al. 1997). This shear strength has been referred to as the undrained steady-state shear strength by Poulos et al. (1985), the undrained residual shear strength by Seed (1987), and critical shear strength by Stark and Mesri (1992). Based on the results of back-analysis of liquefaction case histories, Stark and Mesri (1992) presented an approach for estimating the shear strength of liquefied soils in terms of critical strength ratio and, as a function of clean-sand SPT blow count. Olson and Stark (2002) proposed a relationship for estimating the liquefied shear strength in terms of liquefied shear strength ratio, (s_u/σ'_{vo}). Idriss and Boulanger (2008) suggested that the liquefied shear strength ratio, (s_u/σ'_{vo}) is more effective in describing undrained stress-strain behavior to moderate strain levels in undrained monotonic laboratory tests. The use of (s_u/σ'_{vo}) better reflects the potential effects of strength loss that is induced by the void redistribution than is provided by a direct correlation with s_u (Idriss and Boulanger 2008).

Olson and Stark (2002) proposed a relationship for liquefied shear strength ratio and SPT blow count that showed considerably less scatter as compared to the bounds presented by Stark and Mesri (1992). The Olson and Stark (2002) relationship is purely based on the data from the investigations of 33 liquefaction flow failure case histories. Figure 3.12 shows the Olson and Stark (2002) relationship, where the liquefied shear strength ratio is a function of the SPT blow count value. The relationship indicates approximately linear correlation between liquefied shear strength ratio and penetration resistance up to a normalized SPT blow count value of 12. The median trend line of the relationship between the liquefied shear strength ratio and SPT normalized penetration resistance is expressed as:

$$\frac{s_u(liq.)}{\sigma'_{vo}} = 0.03 + 0.0075 \cdot [(N_{1-60})] \quad (3.1)$$

The above proposed relation is applicable only for $(N_{1\text{-}60}) \leq 12$.

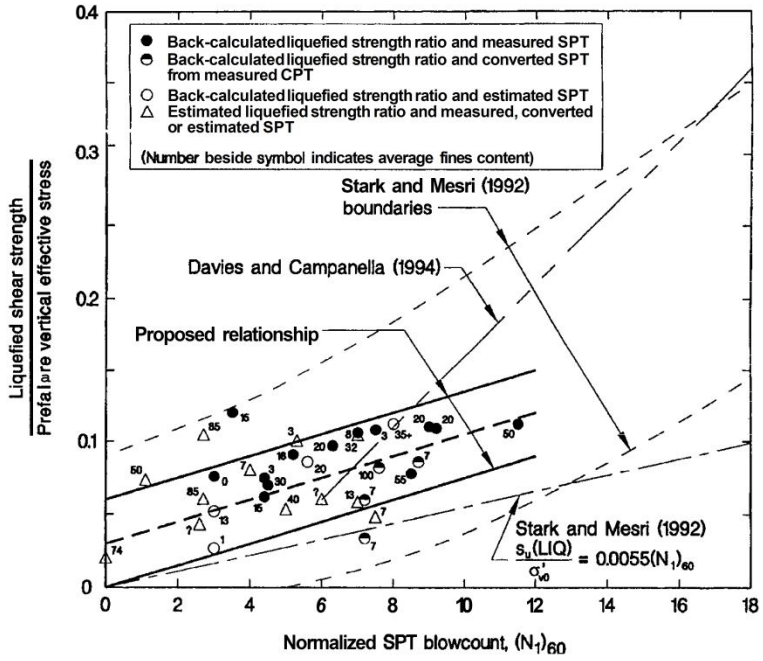

Figure 3.12. A comparison of liquefied strength ratio relationships based on the normalized SPT blowcount (from:Olson and Stark 2002). Used under *fair use* 2013

Based on the relationship proposed by Olson and Stark (2002), an SPT blow count can take any value of liquefied shear strength ratio between the two extremes presented in the relationship. To get multiple values of the liquefied shear strength ratio for a single SPT blow count value, all values between the upper and the lower bounds proposed by Olson and Stark (2002) were considered. The equations for each interpolated line are given by

$$(s_u / \sigma'_{vo}) = m \cdot N_{1-60} + c \tag{3.2}$$

where, c is the intercept of the line and m is the slope. Considering any of the cross-sections described above, the SPT blow count varied in the soil layers and therefore, the resulting liquefied shear strength changed along with the SPT blow count value, the intercept 'c' of the interpolated

curves, and the effective confining stress at each layer. Figure 3.13 shows the interpolated curves between the bounds of the relationship proposed by Olson and Stark (2002).

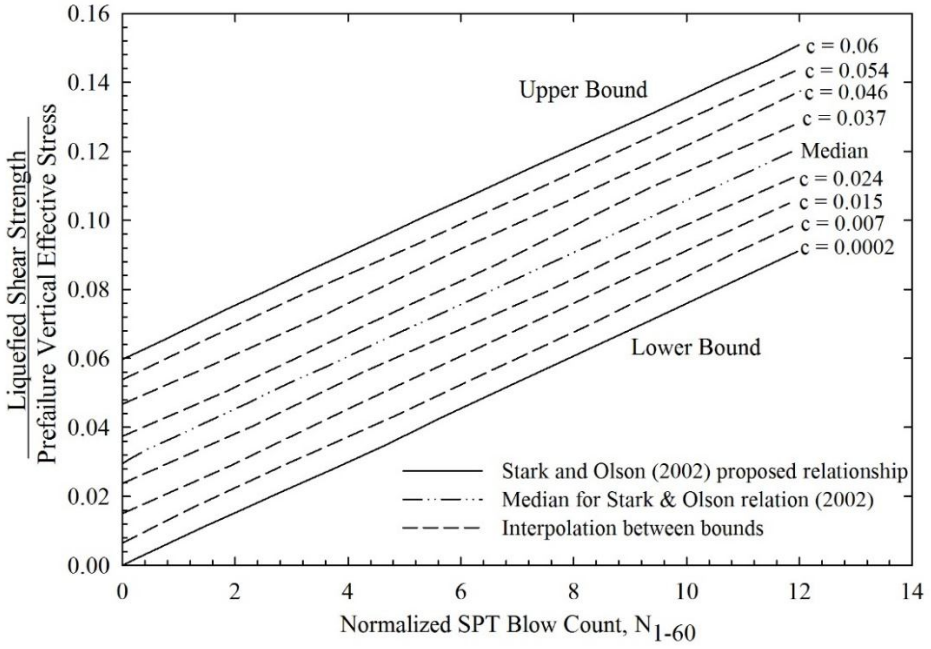

Figure 3.13. Interpolations between the upper and the lower bound curves from the (Olson and Stark 2002) proposed relationship.

The uncertainty of the liquefied shear strength ratio will be represented by allowing the intercept '*c*' to vary; however the slope of the interpolated curves is same as that proposed by Olson and Stark (2002).

The Olson and Stark (2002) relationship is only valid for SPT blow-counts less or equal to 12. To obtain values of liquefied shear strength ratio for SPT blow counts greater than 12, we propose extending the Olson and Stark (2002) relationship and the interpolated curves at a slope suggested by Davies and Campanella (1994). Figure 3.14 shows the interpolated curves between the Olson and Stark (2002) relationship but extended to $(N_1)_{60} > 12$, using the slope from Davies and Campanella (1994) curves.

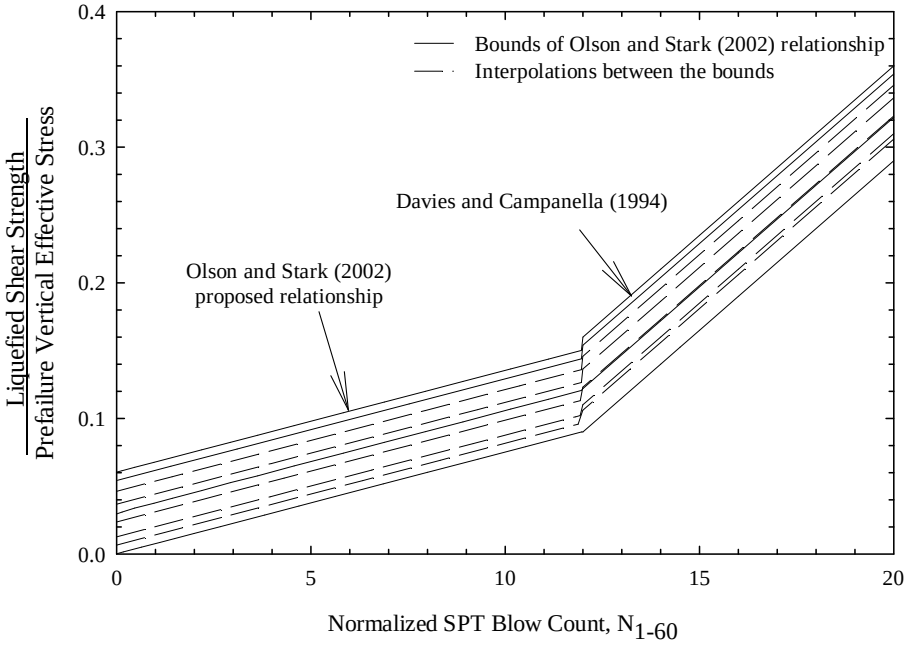

Figure 3.14. Extending the interpolated curves in Olson and Stark (2002) relationship to $(N_1)_{60}$ values > 12 using the slope from Davies and Campanella (1994) curves

Thus, the Davies and Campanella (1994) curves are used for extending the interpolated curves in the Olson and Stark (2002) relationship, in order to get liquefied shear strength for $(N_{1\text{-}60})$ > 12.

3.6 Seismic Slope Stability Analysis

Slopes become unstable when the shear stresses required to maintain equilibrium exceed the available shear strength in the soil profile on some potential failure surface. To account for seismic loading, the traditional assumption is to represent the inertial forces that result from the ground acceleration as a horizontal force, this is known as a pseudo-static analysis. The objective of performing seismic slope stability analysis is to determine the potential failure surface and the 'yield acceleration', that is, the minimum horizontal pseudo-static acceleration required to cause the instability of the soil mass (i.e. producing a unit factor of safety, FS). This section involves a

discussion of the details of the method, the soil model and the seismic coefficient used for seismic slope stability analysis of the developed cross-sections.

Based on the liquefied shear strength ratio and the effective vertical stress at the center of each layer in the profile, shear strengths for each layer were calculated. Once the post - earthquake shear strengths were determined, seismic slope stability analyses were performed using the software SLIDE version 6.0 (Rocscience 2010). Duncan (1996) found that consistent estimates of a slope's FS are calculated from any slope stability procedure that satisfies all three equilibrium conditions. The slopes were analyzed using Spencer's method - a rigorous method of slope analysis satisfying all the three equilibrium conditions: force equilibrium in horizontal and vertical direction and moment equilibrium and applicable to all types of slope geometries. Due to seismic loading on the slopes in the marine terrace, an 'undrained' soil model ($\phi = 0$; $s_u = c$) was found to be appropriate for the analysis. To locate the critical slip surface in a heterogeneous multi-layered slope as in the marine terrace, a non-circular failure surface method was considered, as circular methods can over predict the factor of safety (Zolfaghari et al. 2005). Thus, a non-circular failure surface was used to characterize the slip surface in the slope. In order to get a minimum factor of safety, the simulated annealing search methodology was adopted. Optimizing the non- circular slip surfaces, allowed to search for a slip surface with the lowest possible factor of safety.

Seismic slope stability analysis is complex as it involves the effects of (1) dynamic stresses induced from earthquake shaking and (2) effect of stresses on strength and stress-strain behavior of the slope materials (Kramer 1996). Pseudo-static slope stability analysis is typically used, as it produces a factor of safety against seismic slope failure analogous to the factor of safety produced by limit equilibrium analyses. The results of pseudo-static analysis are critically dependent on the value of the seismic coefficient (k_h), which acts as a horizontal destabilizing force on the landfill.

Seismic coefficients are dimensionless coefficients representing the maximum earthquake acceleration as a fraction of the acceleration due to gravity. The vertical pseudo-static force typically has less influence on the factor of safety and its effect is neglected.

Seed and Martin (1966) developed the concept of horizontal equivalent acceleration (HEA) for earth embankments. The HEA conceptually represents the shear stresses acting at the base of a wedge-type potential sliding mass. In this model, the HEA can be considered to be equivalent to the seismic loading applied to the slopes (Bray and Rathje 1998). Thus, the seismic coefficient (k_h) applied for seismic slope stability analysis is assumed to be equal to the maximum horizontal equivalent acceleration (MHEA). Terzaghi (1950) suggested $k_h = 0.1$ for "severe earthquakes", $k_h = 0.2$ for "violent destructive" earthquakes and $k_h = 0.5$ for "catastrophic earthquakes" (Kramer 1996). However, the maximum value of earthquake acceleration (PGA) is useful in hazard analyses because it is a readily available parameter. Hence, various authors have proposed a wider range of MHEA values tied to the PGA (Bray 2007). In this study, MHEA amplitudes ranging from 0 to 0.5 g with an increment of 0.05 were applied to the slope. These values are compatible with the PGA values estimated at the site during the earthquake. A more comprehensive analysis would have to consider the ratio of MHEA to PGA, but a selection of this ratio for this particular slope geometry is not a simple matter and is beyond the scope of this study.

It is important to note that, prior to performing slope stability analyses, two quantities are unknown: (1) the 'yield acceleration' that causes the failure of the slope and, (2) the undrained shear strength of the liquefied soil. Our approach targets to estimate which of the interpolated curves between the bounds of the Olson and Stark (2002) relationship actually fit the observed failure or no failure patterns. However, uncertainties on the PGA at the site during the earthquake are significant; hence, there are uncertainties on the value of the yield acceleration. The last two

steps of the methodology aim to get a best estimate of the unknown quantities through the generation of a '*Limit State line*' and use of the Bayesian Inference Technique.

3.7 The Limit State Line

As discussed before, seismic slope stability analysis provides the yield acceleration and the location of the weak layer (i.e. the layer through which failure surface passes for FS = 1.0). By assuming different values of the '*c*' parameter, a different shear strength value was assigned to each layer in the cross-section as a function of its SPT N-value, the liquefied shear strength ratio (Figures 3.13 and 3.14), and the pre-failure vertical effective stress. As the shear strength varied, a different seismic load was required for the slope to reach the critical condition (i.e. FS=1). The slope stability analyses for each bin and multiple values of '*c*' yielded an MHEA vs. *c* curve for a unit factor of safety. The MHEA vs. '*c*' curve defines the strength of the soil layer for different dynamic loading. These curves are connected with the SPT N-values of the profiles.

The pseudo-static slope stability analyses can be used to define a *Limit State* line that divides the MHEA vs. '*c*' space into failure and no–failure regions. Figures 3.15 and 3.16 illustrate this process. Each point in Figures 3.15 and 3.16 represent a slope stability analysis for a given bin, with a given value of '*c*', and a given MHEA applied to the slope. All the points for a given bin define the *Limit State* line for that bin. At the same time, each point is also represented as red or green depending on whether the bin it corresponds to was classified as 'failed' or 'non-failed', respectively. The actual combination of MHEA and '*c*' values must lie below the *Limit State* line for the failed bins (e.g., for a given strength, the MHEA computed from slope stability analysis is an upper bound to the MHEA observed by the slope); at the same time, these values must lie above the *Limit State* line for the non-failed bins (e.g., for a given strength, the MHEA computed from slope stability analyses is a lower bound to the MHEA observed by the slope). Figure 3.15

illustrates the process for Approach A, where an equivalent SPT value is assigned to each layer in the soil profile. The dotted line represents an estimate of the location of the true MHEA -'*c*' curve. Bins (3) and (12) underwent failure and are indicated by red dots moving towards the true MHEA -'*c*' curve. The nature of the curve suggests that for higher values of constant '*c*' and thus for higher values of shear strength in the layer, a higher magnitude of seismic load is required to achieve the critical condition (FS = 1.0). Similarly, points for bins (2) and (20) that did not undergo failure, are indicated by green dots that move upwards towards the limit state curve. The points provide the information about the 'yield acceleration' for an absolute value of '*c*' depending on the interpolated curves selected.

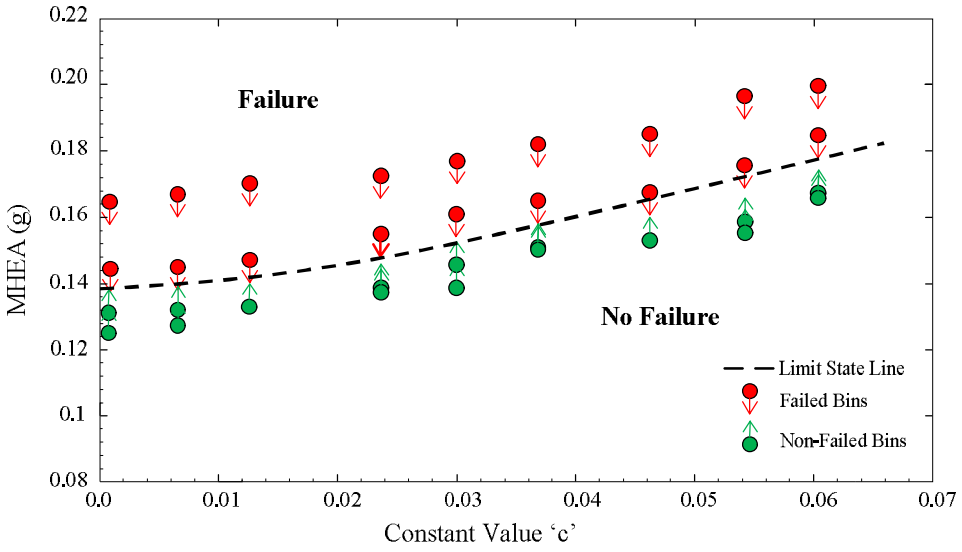

Figure 3.15. Limit State line for bins (2), (3), (12) and (20) on the basis of uniform SPT values in the profile (Approach-A)

Figure 3.16 illustrates the process for Approach B, where each SPT N-value is retained in the layer in the profile. We note that Approach B gives a higher range of yield acceleration values for unit factor of safety as compared to Approach A.

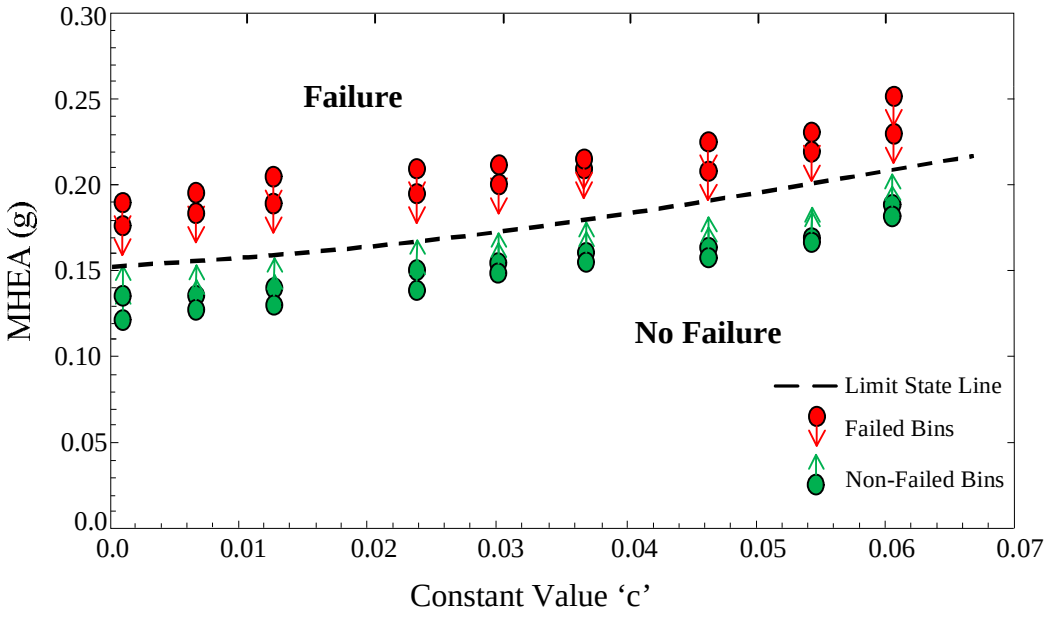

Figure 3.16. Limit State line for bins (2), (3), (12) and (20) on the basis of uniform SPT values in the profile (Approach-B)

We postulate that the MHEA vs. '*c*' curves obtained in this fashion collectively defines the properties for the 4 bins under investigation. It is important to note that the orientation of the points is as per the results from the pseudo-static stability analysis whereas, the color code used to denote the failure and no-failure bins is based on the field observations.

In the preceding paragraphs, we illustrated the process of obtaining the true MHEA -'*c*' curve. In order to do this in a quantitative fashion, we use a Bayesian updating technique. This technique is described in the next section.

3.8 Bayesian Updating Technique

Based on the interpolated curves between the upper and the lower bound curve from the relationship proposed by Olson and Stark (2002), we have a range of '*c*' values that represent the undrained shear strength for the liquefied soils. Also, the interpretation of the displacement

observations determines the 'failure' and 'no-failure' state of the bins. On the basis of the information available, our methodology proposes the use of a Bayesian updating technique in order to get a best estimate of the '*c*' value, given that we know (or we can approximate) the maximum horizontal equivalent acceleration (MHEA). Bayesian updating techniques use Bayes' rule to update the probability estimate of a hypothesis as additional evidence is learned. Bayes' rule is a simple mathematical equation used to calculate conditional probabilities and can be expressed as:

$$P\,(H|D) = \frac{P\,(D|H)}{P(D)} \cdot P\,(H) \tag{3.3}$$

where, H denotes the hypothesis and D denotes the observations from the data. P (D | H) indicates the probability of observing D if the hypothesis is true and is known as the "likelihood" of the event. P (H) denotes the degree of belief regarding the hypothesis before the observations from the data and is known as the prior distribution (Shi et al. 2010). Thus, we get an estimate of the posterior probability of the hypothesis H by updating the probability after learning additional information from the observations. The same rule can be stipulated in term of probability distribution functions (*pdf*) instead of simply probabilities. In order to proceed with our solution to estimate the undrained shear strength, it was important to select prior distributions for the parameters to be used in the Bayesian updating equation.

We are not aware of the nature of the distribution the '*c*' value would follow. For each '*c*' value to be equally probable, we select a uniform distribution, which is also called an 'uninformed prior distribution'. Therefore, the '*c*' value is considered as a random variable with a uniform distribution. The bounds for the distribution are defined by the minimum and the maximum values of '*c*' from the Olson and Stark (2002) relationship. These values are a = 0.002 and b = 0.06. The *pdf* of a uniformly distributed random variable ('*c*') is defined as 1/ (b-a) for '*c*' ϵ (a,b) and 0

otherwise. Also, an 'uninformed prior' or a 'uniform distribution' for the ratio of MHEA to the PGA is assumed. To inform our choice of bounds for the MHEA distribution, we use the results of slope stability analyses presented by Bray and Rathje (1998). Figure 3.17 shows the MHEA at the base of the landfill normalized with respect to PGA plotted against the initial fundamental period of waste fill normalized by the mean period of the input rock motion (Bray and Rathje 1998).

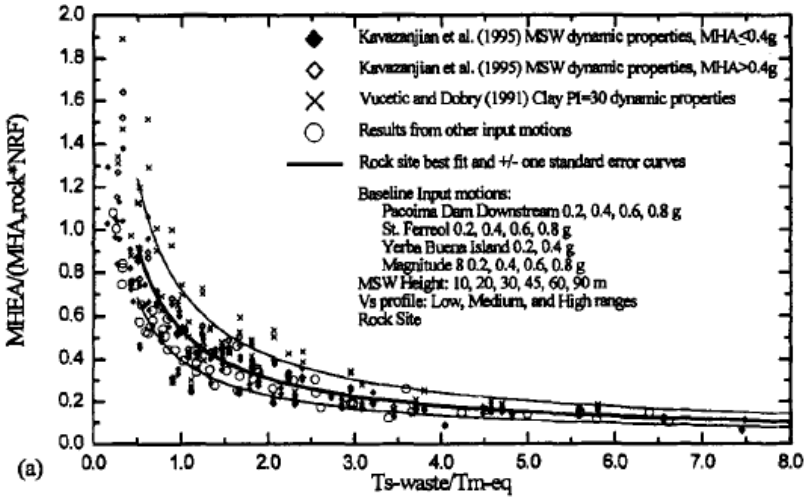

Figure 3.17. Normalized Maximum Horizontal Equivalent Acceleration versus Normalized Fundamental Period of Waste Fill for a Rock Site. (from: Bray and Rathje 1998). Used under *fair use* 2013.

To get a reasonable estimate of the peak ground acceleration, the minimum and the maximum values for the uniform distribution of (MHEA/PGA) was assumed to be 0.4 and 1.0 respectively. A detailed analysis of the selection of the bounding values that would correspond to a more physical analysis of the Canchamana slopes is beyond the scope of this study.

Since most of the ground motion parameters tend to be log-normally distributed, a lognormal distribution is selected for the peak ground acceleration (PGA). Thus, PGA is a log-normally distributed random variable such that its logarithm is normally distributed. The *pdf* of PGA (log-normally distributed variable) is not symmetric and is given by

$$f_{PGA} = \frac{1}{PGA\sqrt{2\Pi}\sigma_{\ln PGA}} \exp[-\frac{1}{2}(\frac{\ln(PGA) - \mu_{\ln PGA}}{\sigma_{\ln PGA}})^2] \quad (3.4)$$

where, μ_{lnPGA} denotes the mean value of the PGA and σ_{lnPGA} denotes its standard deviation.

The earthquake ground motions for the Pisco earthquake were recorded at 15 different stations. Ground motions from the ICA–2 station can be assumed to be a 'best estimate' for the site as the site to station distance was about 40 km (Tavera et al. 2008), which is the same as the source-to site distance of the ICA-2 station. However, it is important to note that this value is only an estimate, and some degree of uncertainty must be associated with it.

An alternative to estimate the PGA at the site is the use of attenuation relationships. Existing attenuation relationships predict PGA as a function of the closest distance to the rupture surface. The choice of attenuation relationship must take into consideration the tectonic conditions in the area. Since, the earthquake was a subduction interface event, models developed by Boore and Atkinson (2003), Gregor et al. (2002), Youngs et al. (1997) and Zhao et al. (2006) were selected. These Ground Motion Prediction Equations (GMPE) were superimposed on the PGA recorded for all 15 stations in Figure 3.18. Observations suggest that the median Young's et al. (1997) GMPE model best fits the attenuation relationship for ICA–2 station point. This model predicts, for a magnitude 8.0 earthquake with a hypocentral depth of 39 km, at approximately 37 km from the rupture surface for a soil site, a median PGA (μ_{lnPGA}) of 0.323 and a standard deviation (σ_{lnPGA}) of 0.65. For comparison, the median PGA for the recordings at ICA-2 site is 0.31 g (Tavera et al. 2008). The uncertainty given by attenuation relationships for the predicted PGA can be used as a bound to the uncertainty on the actual PGA value at the site.

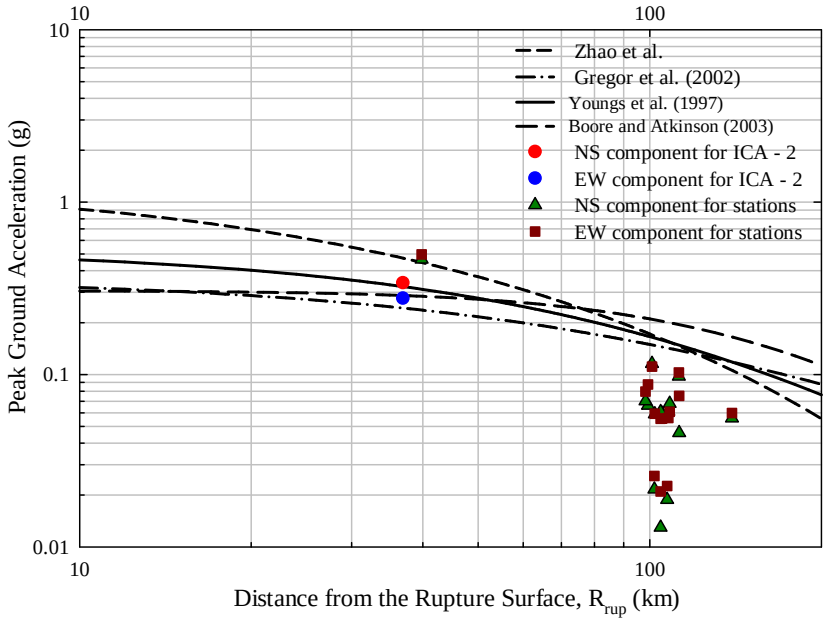

Figure 3.18. Attenuation relationships for subduction zone earthquakes along with the recordings from the 2007 Pisco earthquake. The ICA–2 station recordings are highlighted.

The Bayesian updating technique provides an approach to get the best estimate of the undrained shear strength given that liquefaction has been observed over the marine terrace. The effects of bin 'failure' and 'no-failure' are incorporated into the 'likelihood' term of the Bayesian updating technique. The 'posterior' probability distribution for the *'c'* value given that some bins have failed and some have not failed is given by:

$$f\left(c\middle|F_3 \cdot \overline{F}_2 \cdot F_{12} \cdot \overline{F}_{20}\right) = \frac{P\left(F_3|c\right) \cdot P\left(\overline{F_2}|c\right) \cdot P\left(F_{12}|c\right) \cdot P\left(\overline{F}_{20}|c\right)}{P\left(F_3 \cdot \overline{F}_2 \cdot F_{12} \cdot \overline{F}_{20}\right)} \cdot f(c) \tag{3.5}$$

where $f(c)$ is the prior distribution, $f\left(c\middle|F_3 \cdot \overline{F}_2 \cdot F_{12} \cdot \overline{F}_{20}\right)$ is the posterior distribution of c, F_i denotes failure of bin i, and $\overline{F}_j$ denotes 'no failure' in bin j. The 'likelihood' term in the equation gives the product of probabilities of failure and no-failure of the bin, given that we have an estimate of the *'c'* value. The likelihood is then multiplied with the prior distribution of *'c'* and divided by

a normalizing factor. In this application of the Bayesian updating technique, the probability $P(F_3 \cdot \overline{F}_2 \cdot F_{12} \cdot \overline{F}_{20})$ is fixed and is the normalizing factor in the equation.

The Bayesian updating equation given above is expanded in the form of integrals. The likelihood term collectively is expressed as P (E | *c*), where for simplicity we use E to denote the observation of failure or no failure on a slope or multiple slops (hence, in Equation 3.5, $E = F_3\overline{F_2}F_{12}\overline{F_{20}}$). Hence:

$$P(E \mid c) = \int_{k}^{\infty} \int_{PGA=0}^{\infty} f_{PGA} \cdot f_{MHEA} \cdot H \cdot dPGA \cdot dk \tag{3.6}$$

$$H = \begin{cases} 1, & k \cdot PGA > PGA^* \\ 0, & otherwise \end{cases}$$

where f_{PGA}, f_c, f_{MHEA} are probability distribution functions of peak ground acceleration, '*c*' value and maximum horizontal equivalent acceleration respectively and PGA^* denotes the peak ground acceleration at which failure occurs. The normalizing factor P (E) is expressed as

$$P(E) = \int_{c=0}^{\infty} \int_{PGA^*(c)}^{\infty} f_{PGA} \cdot f_c(c) \cdot dPGA \cdot dc \tag{3.7}$$

The probability density function for PGA (f_{PGA}) has parameters $\mu_{\ln PGA}$ and $\sigma_{\ln PGA}$. The selection of these parameters is an approximation, resulting in large variability. As discussed earlier, the variability in the median PGA can be reduced by assuming that the recordings from ICA-2 apply to the site. However, the uncertainty in PGA (expressed as a standard deviation of PGA, σ_{lnPGA}), also has to be considered.

3.9 Results and Discussion

Using the Bayesian updating technique presented in the previous section, a posterior distribution for the '*c*' value was obtained. As discussed previously, the assumption on the prior distribution of the '*c*' value is that this value is uniformly distributed between the upper and lower bounds given by the Olson and Stark (2002) relationship; the PGA is assumed to be log-normally distributed with a given mean and standard deviation; and the ratio of MHEA to PGA is assumed to be uniformly distributed between 0.4 and 1.0. Figures 3.19 and 3.20 show the posterior distributions for the '*c*' value obtained using Approach-A (uniform cross-section) and Approach B (where the cross section is allowed to vary from east to west according to the measured N values) respectively. Figures 3.19 and 3.20 plot different posterior distributions as a function of the assumed μ_{lnPGA} value for a σ_{lnPGA}= 0.65.

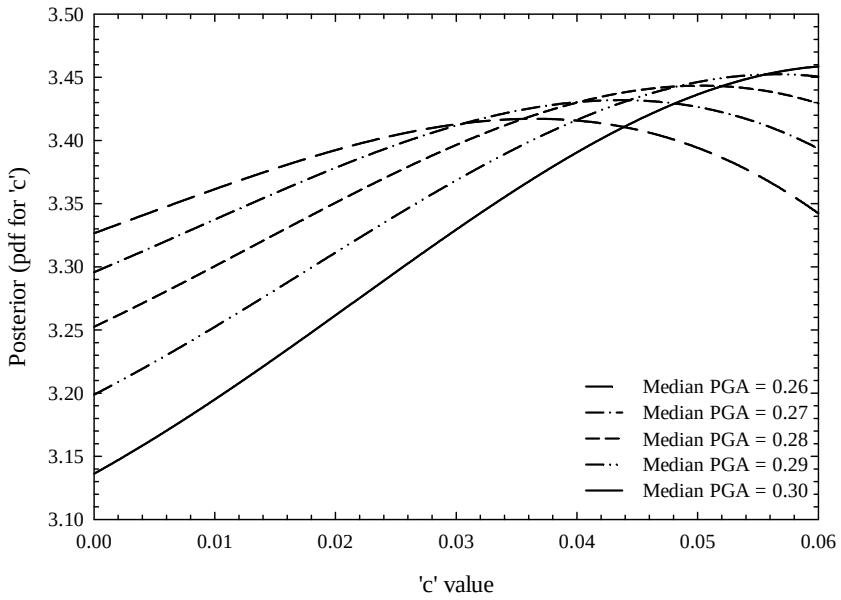

Figure 3.19. Posterior distribution curves for a combination of bin (12) and bin (20) uniform profiles (Approach -A) for σ_{lnPGA} = 0.65

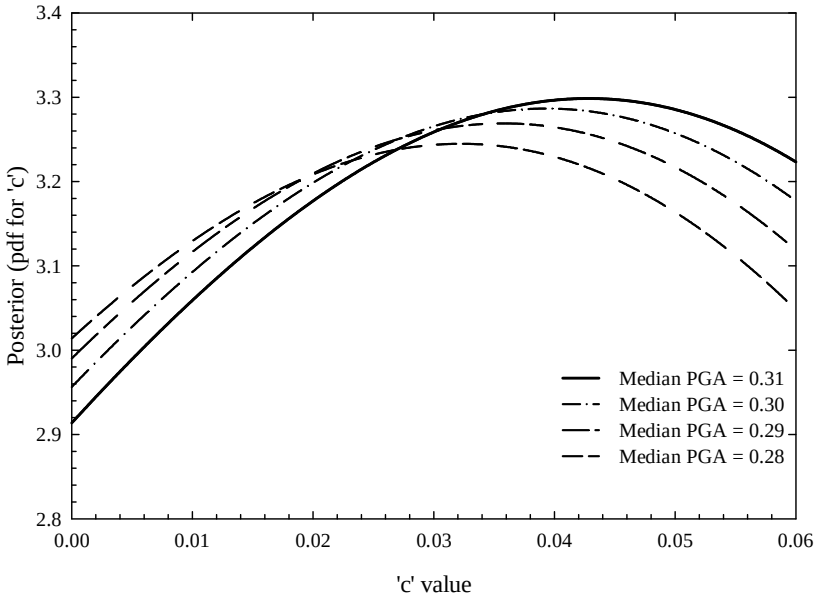

Figure 3.20. Posterior distribution curves for a combination of bin (12) and bin (20) non-uniform profiles (Approach B) for σ_{lnPGA} = 0.65

If an inference of the most likely '*c*' value is needed, the best choice (e.g., the maximum likelihood choice) is the modal value from the posterior distribution curves. We note that the posterior distributions in Figures 3.19 and 3.20 represent the posterior distribution curves developed from the *limit state* lines for a combination of failed bin (12) and non-failed bin (20), for different μ_{lnPGA} with σ_{lnPGA} = 0.65.

The variation of the modal '*c*' value with respect to the change in median PGA and standard deviation of the PGA is presented in Figures 3.21 to 3.24. The posterior distribution curves are developed from the Bayesian updating technique for the *limit state* line results from Approach A. The '*c*' value is the modal value from the posterior distribution curves.

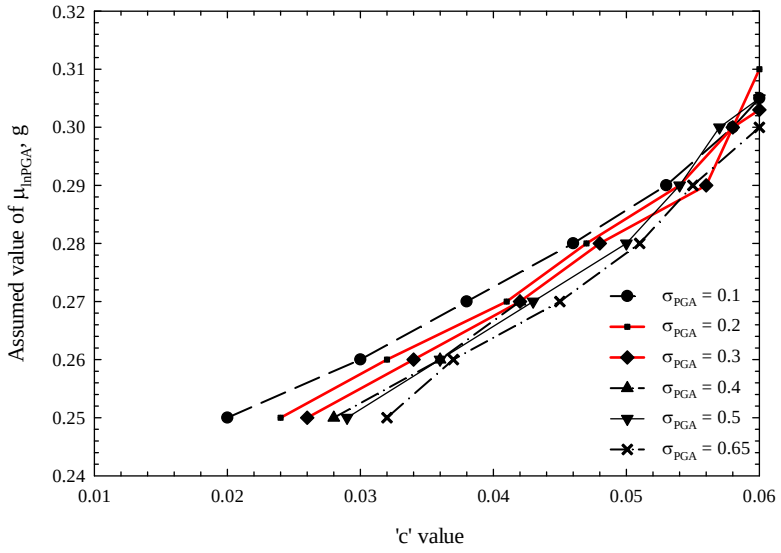

Figure 3.21. Correlation between '*c*' values and the estimated mean PGA (μ_{lnPGA}) from bin (12) and bin (20) *limit state* lines using Approach-A. Red lines indicate best estimate PGA.

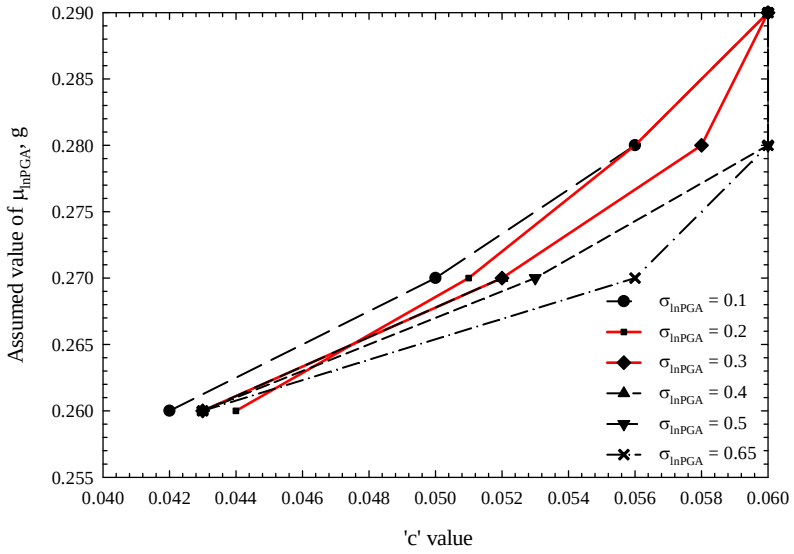

Figure 3.22. Correlation between *'c'* values and the estimated mean PGA (μ_{lnPGA}) from bin (3) and bin (20) *limit state* lines using Approach-A. Red lines indicate best estimate PGA.

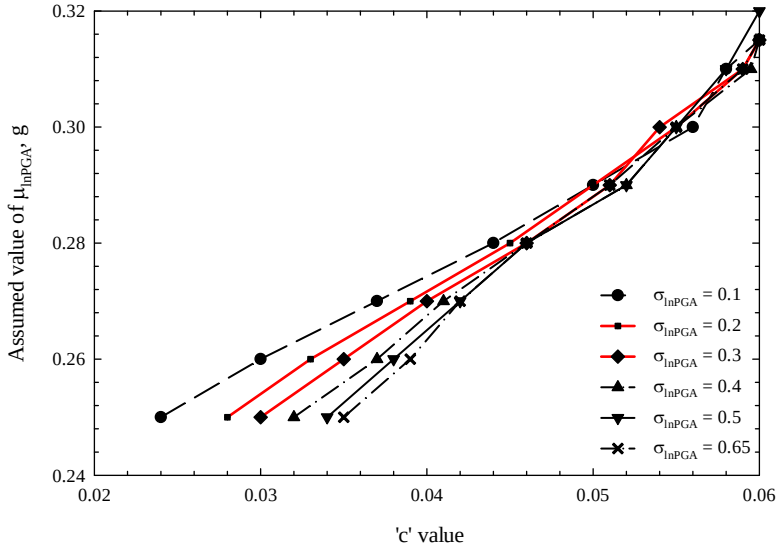

Figure 3.23. Correlation between *'c'* values and the estimated mean PGA (μ_{lnPGA}) from bin (12) and bin (2) *limit state* lines using Approach-A. Red lines indicate best estimate PGA.

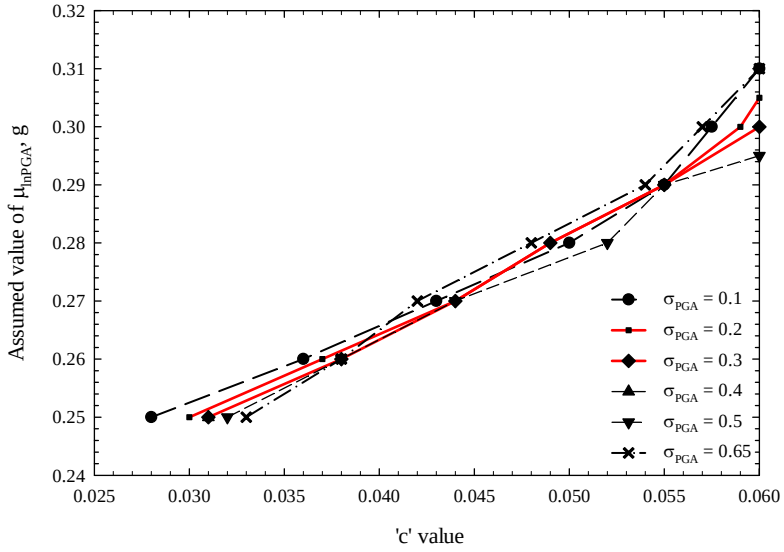

Figure 3.24 Correlation between '*c*' values and the estimated mean PGA (μ_{lnPGA}) from bin (3) and bin (2) *limit state* lines using Approach-A. Red lines indicate best estimate PGA.

Figures 3.21 to 3.24 support the following conclusions:

- The upper bound of the Olson and Stark (2002) relationship (e.g., c = 0.06) indicates that the maximum possible mean PGA for the site varied between 0.3 g and 0.31 g (see Table 3.3). These PGA values are compatible with those measured in the ICA-2 station, which is at the same distance to the source as the Canchamana site; however, are much lower than the records at the ICA-1 station, which recorded PGAs up to 0.5 g. However, the mean PGAs stated above include varied levels of uncertainty, hence the data is not completely incompatible with the 0.5 g PGA measured in ICA-1 station.
- The intra-event standard deviation from Atkinson and Boore (2003) is 0.25. In the absence of additional information, this is the best estimate for the uncertainty at the Canchamana site. Hence, the lines in red in Figures 3.21 to 3.24 represent the best-estimate PGA-'*c*' value relationship. If, in addition, we assume that the PGA at the site

is equal to that measured at ICA-2 station (PGA= 0.31g), which has the same distance to the source as the Canchamana site, then the best estimate for the '*c*' value is given in Table 3.4.

- In the analysis of failure surfaces, we are testing the N-values corresponding to the critical failure surfaces in the cross-sections. In Approach A, for all the bins, the N-values in the critical failure surfaces are greater than 12. Therefore, we are testing the N-values greater than 12 and as a result, we end up testing the Davies and Campanella (1994) curves, which are used to extend the relationship proposed by Olson and Stark (2002) beyond an SPT N-value of 12.

Table 3.3. Estimated μ_{lnPGA} values from Approach A for the *'c'* value corresponding to the upper bound of Olson and Stark (2002) relationship.

(Failed – Not Failed) bins	**Maximum μ_{lnPGA} (g)**
Bin (12) – Bin (20)	0.31
Bin (3)– Bin (20)	0.29
Bin (12) – Bin (2)	0.32
Bin (3) – Bin (2)	0.31

Table 3.4. Range of 'c' values using Approach A and assuming that the median PGA is that measured by the ICA-2 station.

(Failed – Not Failed) bins	**Range of σ_{lnPGA} from 0.1 to 0.65**	**Range of σ_{lnPGA} from 0.2 to 0.3**
Bin (12) – Bin (20)	0.06	0.060
Bin (3)– Bin (20)	--	--
Bin (12) – Bin (2)	0.058 to 0.06	0.059
Bin (3) – Bin (2)	0.06	0.059 to 0.06

The results summarized in Figures 3.21 to 3.24 correspond to Approach A, where a uniform cross-section was assumed. These analyses were repeated for a non-uniform cross-section (Approach B). The results are shown in Figures 3.25 to 3.28.

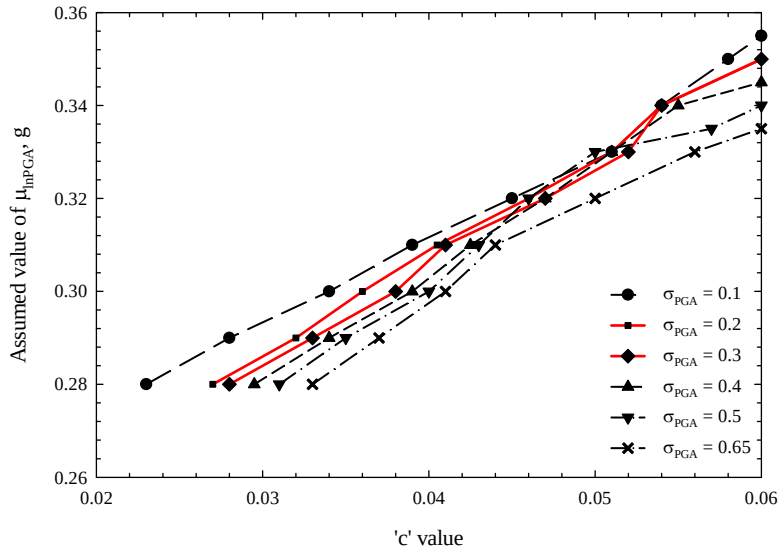

Figure 3.25. Correlation between '*c*' values and the estimated mean PGA (μ_{lnPGA}) from bin (12) and bin (20) *limit state* lines using Approach-B. Red lines indicate best estimate PGA.

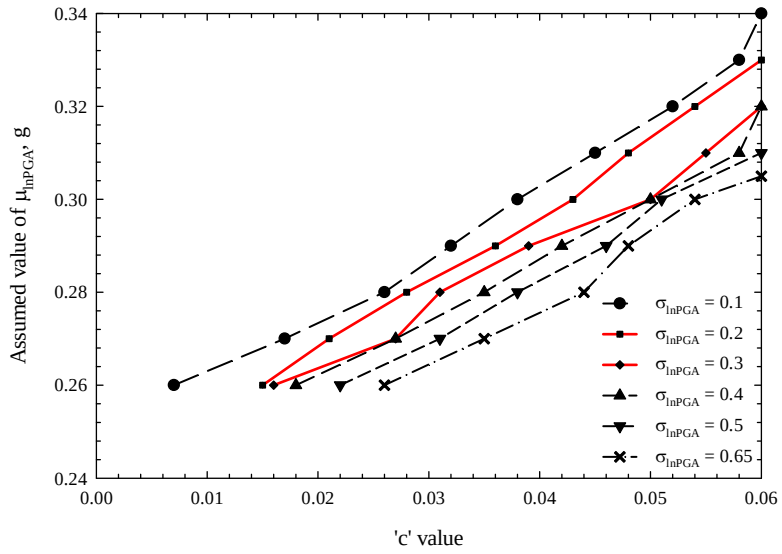

Figure 3.26. Correlation between '*c*' values and the estimated mean PGA (μ_{lnPGA}) from bin (3) and bin (20) *limit state* lines using Approach-B. Red lines indicate best estimate PGA.

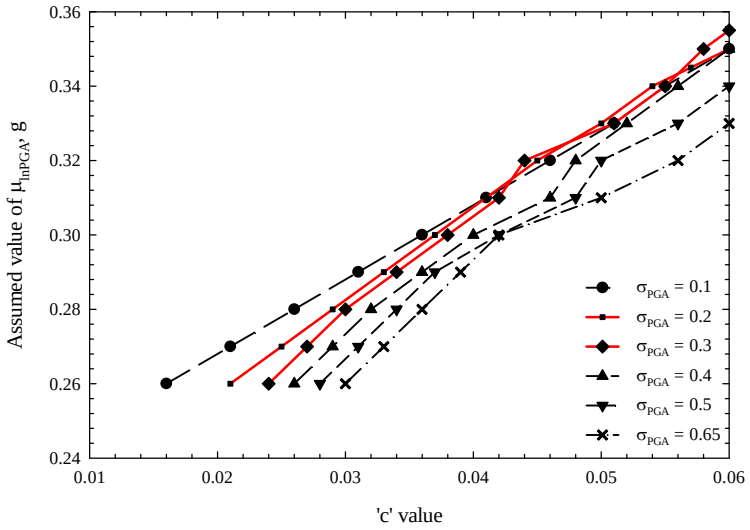

Figure 3.27. Correlation between '*c*' values and the estimated mean PGA (μ_{lnPGA}) from bin (12) and bin (2) *limit state* lines using Approach-B. Red lines indicate best estimate PGA.

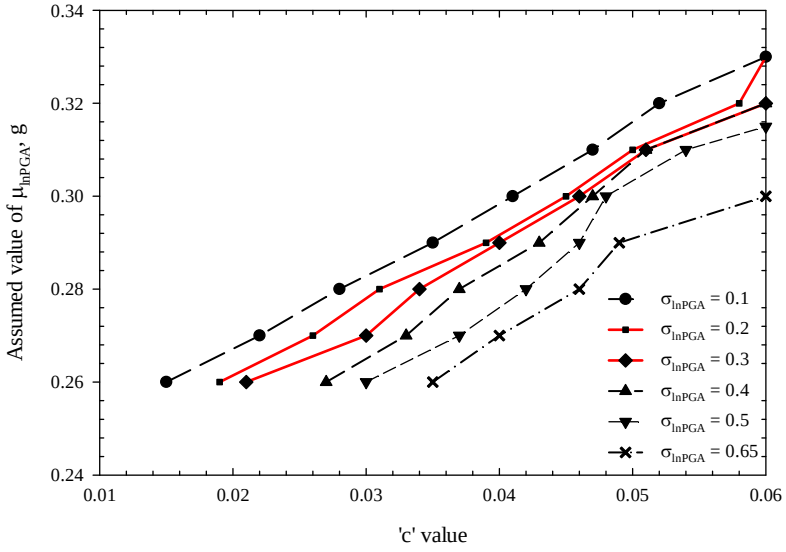

Figure 3.28. Correlation between '*c*' values and the estimated mean PGA (μ_{lnPGA}) from bin (3) and bin (2) *limit state* lines using Approach-B. Red lines indicate best estimate PGA.

The conclusions that can be reached from the information summarized in Figures 3.25 to 3.28 are:

- Assuming that the *'c'* value corresponds the upper bound of Olson and Stark (2002), then the range of median PGAs for the different combination of cross sections is given in Table 3.5 for σ_{lnPGA} ranging from 0.1 to 0.65. If we restrict the range of σ_{lnPGA} to 0.2 to 0.3, compatible with the intra-event variability in Atkinson and Boore (2003), then the median PGAs are those listed in the second column in Table 3.5.
- Similar to Approach A, if we assume the median PGA to be that measured in ICA-2 station, then the range of modal *'c'* values is given in Table 3.6, and the best estimate for these values is those corresponding to a range of σ_{lnPGA} of 0.2 to 0.3, and those estimates are given in the last column of Table 3.6.
- Analysis of the critical failure surfaces from slope stability analyses reveal that the N-values being tested for Approach B are the lowest N-values in the bin (2) and (3), and are less than 12. In this case, we are testing the Olson and Stark (2002) curves for evaluating the undrained shear strength. Whereas, for bin (12) and (20) the critical N-values are greater than 12 and we end up testing the Davies and Campanella (1994) curves for evaluating the undrained shear strength.

Table 3.5. Range of μ_{lnPGA} values (g), from Approach B, for the 'c' value corresponding to the upper bound of Olson and Stark (2002) relationship.

(Failed – Not Failed) bins	**Range of σ_{lnPGA} from 0.1 to 0.65**	**Range of σ_{lnPGA} from 0.2 to 0.3**
Bin (12) – Bin (20)	0.335 to 0.355	0.35
Bin (3)– Bin (20)	0.305 to 0.34	0.33 to 0.32
Bin (12) – Bin (2)	0.33 to 0.35	0.35 to 0.355
Bin (3) – Bin (2)	0.3 to 0.33	0.33 to 0.32

Table 3.6. Range of 'c' values using Approach B and assuming that the median PGA is that measured by the ICA2 station.

(Failed – Not Failed) bins	**Range of σ_{lnPGA} from 0.1 to 0.65**	**Range of σ_{lnPGA} from 0.2 to 0.3**
Bin (12) – Bin (20)	0.039 to 0.044	0.0405 to 0.041
Bin (3)– Bin (20)	0.045 to 0.06	0.048 to 0.055
Bin (12) – Bin (2)	0.041 to 0.05	0.041 to 0.042
Bin (3) – Bin (2)	0.047 to 0.06	0.050 to 0.051

Approach (B) produces better results because it represents a more realistic profile. Results from Approach (B) also allow us to extend our control value of μ_{lnPGA} for Bayesian updating technique to the μ_{lnPGA} recordings at ICA–2. The constant value '*c*' can be estimated to be 0.046, taking the arithmetic average of the results in Table 3.6, for the more limited σ_{lnPGA} range of 0.2 to 0.3. Similarly, Approach A produces an average '*c*' value of 0.060. Thus, we can estimate the range of the constant '*c*' value to be between 0.046 and 0.060, however the difference in the results from the two approaches is marginal. The upper bound curve (Approach A) and the color highlighted curve (Approach B) present the closest estimate of the curves that best fits the observations and the analysis to determine the undrained shear strength of the liquefied soil (Figure 3.29)

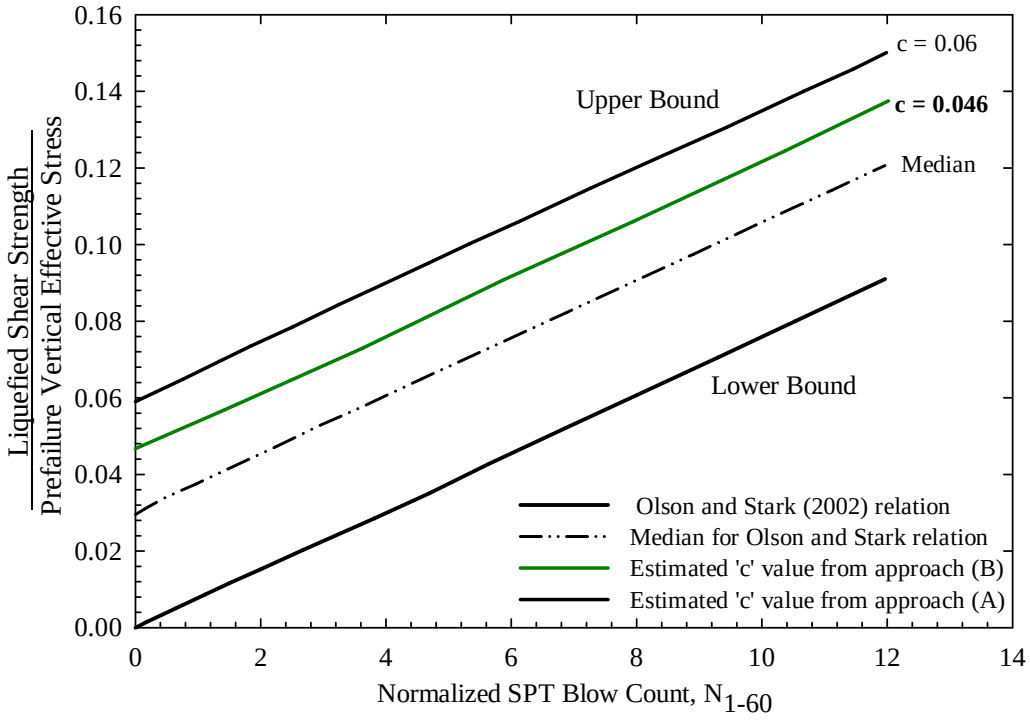

Figure 3.29. Estimated range of constant value '*c*' between Approach A and Approach B bounds

The two approaches yield two different estimate of the '*c*' value. A reasonable assumption will be to consider the estimated range of '*c*' value to lie between the curves derived from Approach A and B. The two curves presenting the '*c*' values are the results of the methodology adopted and can be used to determine the undrained shear strength for the liquefied soil at Canchamana for a given SPT N-value.

3.10 Summary and Conclusions

A back-analysis procedure to estimate the undrained shear strength of liquefied soils from the observations of a lateral spreading ground failure case history was presented in the paper. The procedure was applied to the Canchamana lateral spread complex, which occurred during the 2007 Pisco earthquake. Based on the field exploration results, vertical cross-sections were developed

for various horizontal cross sections across the lateral spread. The relationship by Olson and Stark (2002), which correlates $(N_1)_{60}$ values to liquefied shear strength ratio, was adopted to assign a liquefied shear strength ratio to the soils at the site. The Olson and Stark (2002) relationship was extended to higher $(N_1)_{60}$ values using the bounds proposed by Davies and Campanella (1994). Slope stability analyses were performed to back-calculate the liquefied shear strength for different values of seismic demand. The Bayesian updating technique was then used to get an approximation of the undrained shear strength of the liquefied soils, based on estimates of the accelerations at the site, and on measured displacements in the Canchamana complex.

The proposed methodology accounts for uncertainty of PGA and the undrained shear strength. Results were computed for a profile that was assumed to be horizontally uniform (Approach A) and for a profile that allowed for horizontal variability in undrained strength (Approach B). If, in addition, the median PGA measured at the ICA-2 station is applicable to the site, the results of the analyses gave a '*c*' value of 0.060 and 0.046 for Approach A and B, respectively. Conversely, if the upper bound of the Olson and Stark (2002) and the Davies and Campanella (1994) relationships are assumed to hold, the median PGA at the site is estimated to be between 0.3 g and 0.33 g. These results assume an uncertainty in the PGA equal to the intra-event variability suggested by Atkinson and Boore (2003). The results from Approach-B provide a more reasonable approximation of undrained shear strength of the liquefied soils, as it closely matches the actual conditions in the field.

Acknowledgements

The author is deeply grateful to Dr. Adrian Rodriguez- Marek for his valuable guidance and immense support in the development of the present study. Special thanks to the members of the reconnaissance team for providing the field exploration results that served in the development of the present study. The contribution of Dr. Brady Cox was instrumental in furnishing most of the data used in this study, including the SPT profiles. Dr. Cox also provided the DEM data developed by the CAST center in Arkansas. Last but not the least, this work would not have been possible without the facilities provided by the graduate program in the Civil and Environmental Engineering Department at Virginia Tech.

References

Atkinson, G.M., and Boore, D.M., (2003). “Empirical ground-motion relations for subduction-zone earthquakes and their application to Cascadia and other regions”. *Bulletin of the Seismological Society of America*, v. 93, no. 4, p. 1703–1729.

Bray, J.D. and Rathje, E.R. (1998) “Earthquake-Induced Displacements of Solid-Waste Landfills”. *Journal of Geotechnical and Geoenvironmental Engineering*, 124(3), 242-253.

Bray, J.D. (2007). “Chapter 14: Simplified seismic slope displacement procedures.” *Proc., 4th Int. Conf. on Earthquake Geotechnical Engineering—Invited Lectures, in Geotechnical, Geological, and Earthquake Engineering Series*, K. D. Pitilakis, ed., Vol. 6, Springer, New York, 327–353.

Castro, G. (1969). “Liquefaction of sands.” *Ph.D. thesis reprinted as Harvard Soil Mechanics Series NO.81*, Harvard University, Cambridge MA, 112

Davies, M.P., and Campanella, R.G. (1994). “Selecting design values of undrained strength for cohesionless soils”. In Proceedings of the 47th Canadian Geotechnical Conference, Halifax, Nova Scotia, September 1994, BiTech Publishers. Vol. 1, 176–186.

Duncan J.M. (1996). “State of the art: limit equilibrium and finite element analysis of slopes”. *J. Geotech. Eng.*, 122(7), 577-596.

Duncan, J.M., and Wright, S.G. (2005). *Soil Strength And Slope Stability,* John Wiley & Sons.

Mid-America Earthquake (MAE) Center Report 08-01 (2008). "The Pisco-Chincha Earthquake of August 15,2007 – Seismological, Geotechnical and Structural Assessments". *Report of Mid-America Earthquake Center*., Civil and Environmental Engineering Department, University of Illinois at Urbana-Champaign, Urbana, Illinois, USA.

GEER Association Report No. GEER-012 (2007). "Preliminary reconnaissance report on the geotechnical engineering aspects of the August 15, 2007 Pisco, Peru Earthquake". *Report of the National Science Foundation-sponsored Geotechnical Earthquake Engineering Reconnaissance (GEER) team*. Web report available from: http://www.geerassociation.org/GEER_Post%20EQ%20Reports/Peru_2007/Cover_Peru2007.html

Idriss, I. and Boulanger, R. W. (2008). *Soil liquefaction during earthquakes*, Earthquake Engineering Research Institute.

Ji, C. and Zeng, Y. (2007). "Preliminary Result of the Aug 15, 2007 Mw 8.0 Coast of Central Peru Earthquake". *Web report (http://earthquake.usgs.gov/eqcenter/eqinthenews/2007/us/2007/gbcv/finite_fault.php).*

Kramer,S.L. (1996). *Geotechnical earthquake engineering*, Prentice Hall, New York.

Olson, S.M., & Stark, T.D. (2002). "Liquefied strength ratio from liquefaction flow failure case histories". Canadian Geotechnical Journal, 39(3), 629-647.

Poulos, S.J., Castro, G., and France, J. (1985). "Liquefaction evaluation procedure". *J. Geotech. Engrg.*, 111(6), 772–792

Rauch, A.F. (1997) "EPOLLS: An empirical method for predicting surface displacements due to liquefaction-induced lateral spreading in earthquakes". *PhD thesis*, Virginia Polytechnic Institute and State University; 1997; 333.

Rocscience, Inc. (2010). "*Slide v6.0—2D limit equilibrium slope stability analysis"*, Toronto.

Seed, H., Martin R. (1966). *The Seismic Coefficient in Earth Dam Design*, University of California, Department of Civil Engineering [and] Institute of Transportation and Traffic Engineering, California.

Seed, H. (1987). "Design Problems in Soil Liquefaction". *J.Geotech.Engrg*., 113(8), 827-845

Seed, R. B. and Harder, L. F. (1990). "SPT-based analysis of cyclic pore pressure generation and undrained residual strength". *Proc., H.B. Seed Memorial Symp., Vol. 2*, BiTech Publishers Ltd, Vancouver, B. C., Canada

Shi L., Griffiths T.L., Feldman N.H., & Sanborn A.N. (2010). "Exemplar models as a mechanism for performing Bayesian inference". *Psychonomic Bulletin & Review.* 17, 443–464.

Stark, T.D., and Mesri, G. (1992). "Undrained shear strength of liquefied sands for stability analysis". *J. Geotech. Engrg*., ASCE, 118(11),1727-1747.

Stark, T.D., Olson, S.M., Kramer S.L., Youd, T.L. (1998). "Shear Strength of Liquefied Soil". *Proc.,Geotechnical Earthquake Engineering and Soil Dynamics-III*. pp. 313-324. Seattle Washington USA.

Tavera, H., Bernal, I., Strasser, F.O., Arango-Gaviria, M.C., Alarcón, J.E. and Bommer, J.J. (2008)". Ground motions observed during the 15 August 2007 Pisco, Peru, event". *Bulletin of Earthquake Engineering*.

Terzaghi, K., (1950) “Mechanism of landslides”. *Geological Society of America*, Geol. (Berkeley) Vol. (1950), 83-123.

Wood, C. and Cox, B. (2012). “A Comparison of MASW Dispersion Uncertainty and Bias for Impact and Harmonic Sources”. *Proc., GeoCongress 2012: State of the Art and Practice in Geotechnical Engineering.* pp. 2765-2765.

Youd, T. L., and Hoose, S. N. (1976). “Liquefaction during the 1906 San Francisco Earthquake.” *J. Geotech. Engrg*. Div., ASCE, 112(5), 425-439.

Zolfaghari, A. R., Heath, A. C., McCombie, P.F. (2005) “Simple genetic algorithm search for critical non-circular failure surface in slope stability analysis.” *Computers and Geotechnics*, 32(3), 139–152.

4 Engineering Significance & Recommendations for Future Work

The engineering significance of this work is the presentation of a back-analysis methodology that accounts for uncertainties in the input parameters. When applied to the Canchamana lateral spread case history, the methodology renders estimates of the undrained strength of liquefied soils. Empirical estimates of this parameter are rare, and hence the significance of the work is large.

The methodology proposed in the thesis accounts for uncertainty of PGA and the undrained shear strength. Results were computed for a profile that was assumed to be horizontally uniform (Approach A) and for a profile that allowed for horizontal variability in undrained strength (Approach B). For the median PGA measured at the ICA-2 station being applicable to the site, the results yielded a '*c*' value of 0.060 and 0.046 for Approach A and B, respectively. Conversely, if the upper bound of the Olson and Stark (2002) and the Davies and Campanella (1994) relationships are assumed to hold, the median PGA at the site is estimated to be between 0.3 g and 0.33 g. These results assume an uncertainty in the PGA equal to the intra-event variability suggested by Atkinson and Boore (2003). The results from Approach B provide a more reasonable approximation of undrained shear strength of the liquefied soils, as it represents the realistic conditions in the field.

The back-analysis methodology used to obtain the undrained shear strength of the liquefied soils is not simple and involves assumptions and approximations. Certain areas of this study can be improved in future work. The future work can involve:

- The developed cross-sections from Approach B can be further detailed to include a more realistic change in the soil interface between the tests locations in the terrace.

- A different variation of the SPT penetration resistance and hence the liquefied shear strength can be assumed across the developed cross-sections.
- Current methodology only deals with the maximum displacement occurring in the bin. A better understanding of the displacements in the bin can be incorporated by including the relative displacements of the bins.
- Current model and method used for slope stability analysis can be replaced with more efficient methods of performing slope stability analysis of liquefied soils. Olson and Stark (2002) incorporated kinetics of mass movements in slope stability analysis to get a better approximation of the liquefied shear strength. On similar lines, kinetics of the failure mass can be included to get a better approximation of the liquefied shear strength.
- The variability of the results can be tested by selecting a different relationship that correlates the liquefied shear strength ratio and SPT penetration resistance.
- Moreover, assuming different prior distributions for the '*c*' value and MHEA/PGA can contribute towards the sensitivity analysis, which might possibly yield a different estimate of the liquefied shear strength.
- In addition to the above mentioned recommendations, as we are dealing with a lateral spreading case history, efforts can be made to compute ground surface displacements by using empirical models and simple analytical models. A study comparing the magnitude of the displacements from the two models can be incorporated.
- This lateral spreading case history can be compared with a flow failure case history to compare the back-calculated shear strength of the liquefied soils and to monitor the strength loss due to two different types of ground failures (given that the flow failure case history

has an available SPT penetration resistance dataset or a measure of relative density that can aid in evaluating the “representative” SPT N-values).

Appendix I: Composition of reconnaissance and field investigation teams

In response to the 2007 Pisco earthquake event, the Geotechnical Earthquake Engineering Reconnaissance (GEER) organization, with funding from the National Science Foundation (NSF), organized a reconnaissance team to investigate the geotechnical engineering aspects of the earthquake. The reconnaissance team arrived in Peru on August 20, 2007 and visited the cities of Lima, Paracas, Pisco and Ica and other smaller coastal towns. A complete list of the team members of the reconnaissance team and their associated institution is listed in Table AI-1.

A comprehensive field characterization study was completed in the Canchamana complex about 2.5 years after the earthquake. A complete list of the team members of the field exploration team and their associated institution is listed in Table AI-2.

Table AI-1. Reconnaissance team

Team member	Institution (at time of reconnaissance)	Current Institution
Adrian Rodriguez-Marek	Washington State University	Virginia Tech
Joseph Wartman	Drexel University	University of Washington
Brady Cox	U. of Arkansas	U. of Texas
Jorge Meneses	Kleinfelder	GEI
Manuel Olcese	Catholic University of Peru	Catholic University of Peru

Table AI-2. Field Investigation teams

Institution (at time of reconnaissance)	Team Member
Washington State University	Adrian Rodriguez-Marek
Drexel University	Dr. Joseph Wartman (Leader) Patrick Strenk (Student)
U. of Arkansas	Dr. Brady Cox (Team Leader) Adam Barnes (CAST member, leader of the remote sensing group) Humberto Albarran (Student)
Kleinfelder	Dr. Jorge Meneses
Universidad Nacional de Lima, Peru	Dr. Zenon Aguilar (Leader) Pablo Peri (Student)

Appendix II: Slope Stability Analysis

This section of the thesis presents a short summary of the slope stability analysis performed to back-calculate the liquefied shear strength of soils. The cross-sections for slope stability analysis were developed in SLIDE version 6.0 using Approach A and Approach B, discussed earlier in Chapter 3. The SLIDE input and output files for each bin under investigation are included in this section.

The cross-sections are developed with each layer in the cross-section being parallel to the ground surface topography. Based on Approach A and Approach B, each layer in the cross-section is assigned a liquefied shear strength ratio. Olson and Stark (2002) relationship is used to relate the SPT N-values to the liquefied shear strength ratio. The Olson and Stark (2002) is complemented by Davies and Campanella (1994) curves for SPT N-values > 12. The effective vertical stress at the center of each layer in the cross-section aided in calculating the undrained shear strength in each layer. Once, the post-earthquake shear strengths were assigned to the layers in the cross-section, slope stability analyses were performed using the software SLIDE version 6.0 (Rocscience, 2010).

Spencer's method of slope stability analysis was used to analyze the slopes because this method of analysis was applicable to all types of slope geometries and satisfied all the three equilibrium conditions (i.e. force equilibrium in the horizontal and vertical direction and moment equilibrium). Since the slopes were subjected to seismic loading, an 'undrained' soil model was used for the analysis. For an 'undrained' soil model, the strength of the soil is expressed with $\phi = 0 \; and \; s_u = c$. The cross-sections involved multi-soil layers and hence a non-circular failure surface was selected to characterize the slip surface in the slope. To get the slip surface with the

lowest factor of safety, simulated annealing and optimization techniques were used as a part of the non-circular surface search methodology. In order to simulate the earthquake loading on the slopes, seismic coefficient (k_h) was applied to the slope. Since the cross-sections developed from the details of investigations, were shallow, a dry soil 'cap' layer was inserted at the top of the developed cross-sections to impinge the failure surface deeper into the cross-sections in order to find the weak layer. The input and output files of slope stability analysis are shown in Figures 1 to 16.

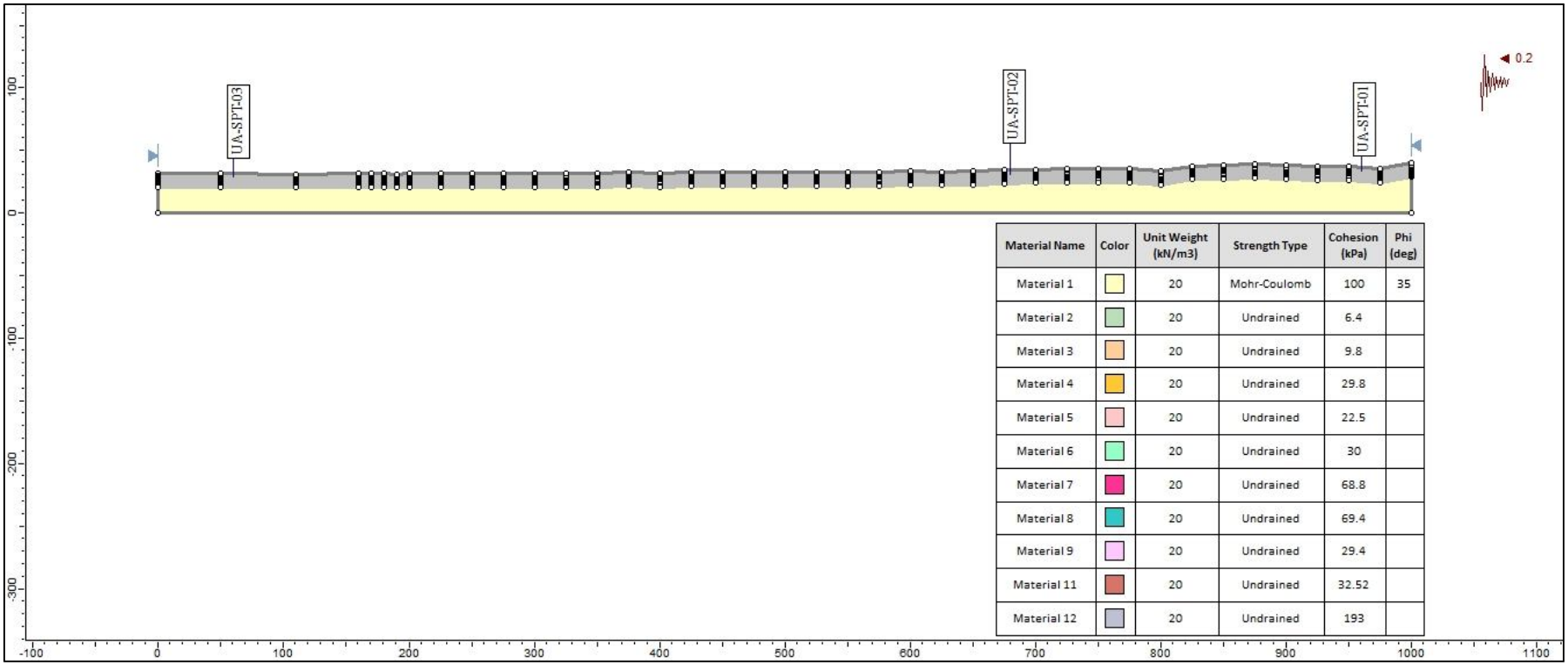

Material Name	Color	Unit Weight (kN/m3)	Strength Type	Cohesion (kPa)	Phi (deg)
Material 1		20	Mohr-Coulomb	100	35
Material 2		20	Undrained	6.4	
Material 3		20	Undrained	9.8	
Material 4		20	Undrained	29.8	
Material 5		20	Undrained	22.5	
Material 6		20	Undrained	30	
Material 7		20	Undrained	68.8	
Material 8		20	Undrained	69.4	
Material 9		20	Undrained	29.4	
Material 11		20	Undrained	32.52	
Material 12		20	Undrained	193	

Figure AII-1. SLIDE input file for Bin (12), Uniform Profile

Figure AII - 2. Layering for Bin (12) – Uniform Profile

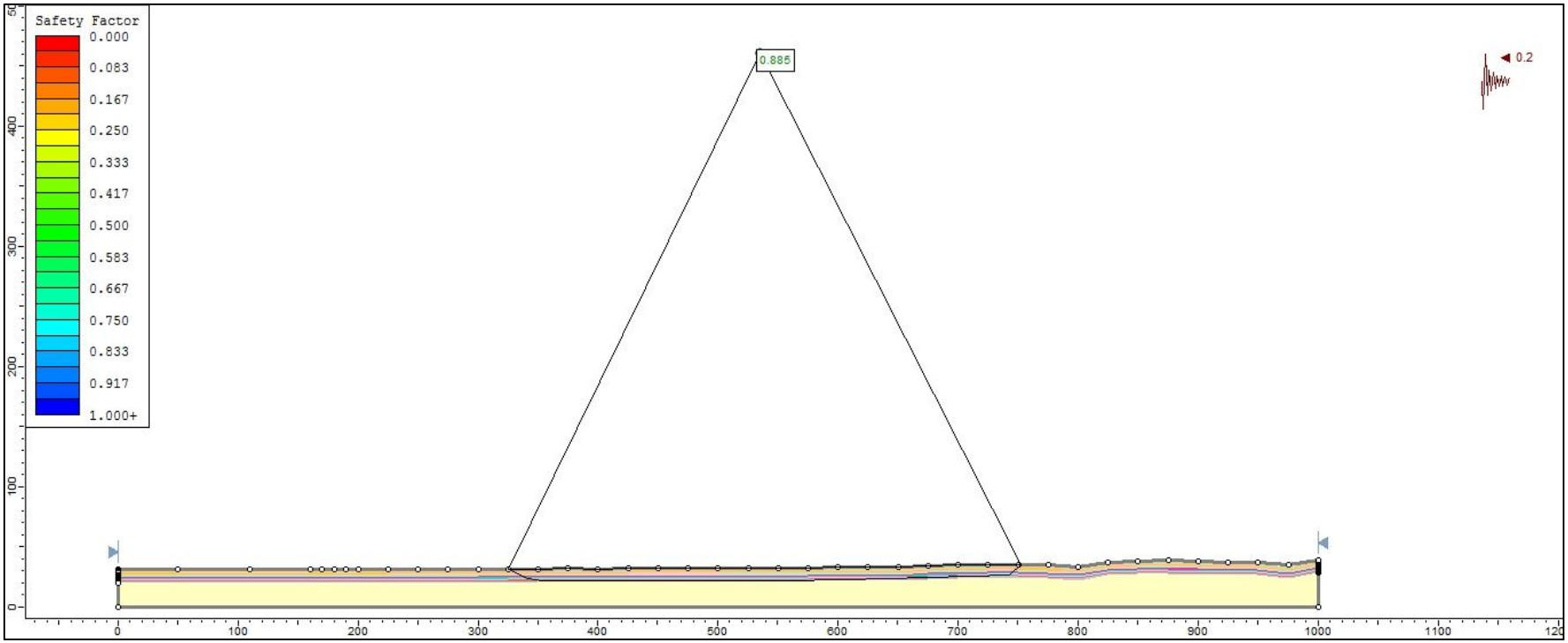

Figure AII - 3. Output for Bin (12) – Uniform Profile

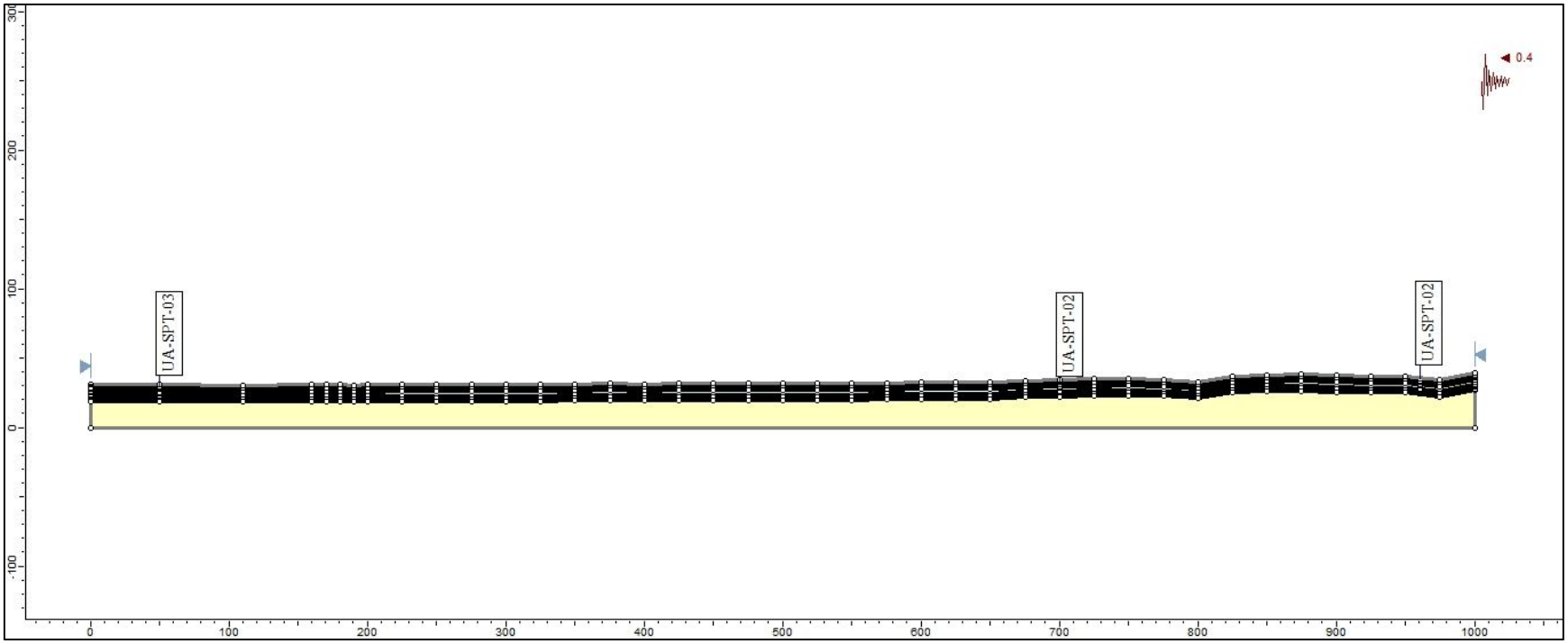

Figure AII-4. SLIDE input file for Bin (12) – Non-uniform layering

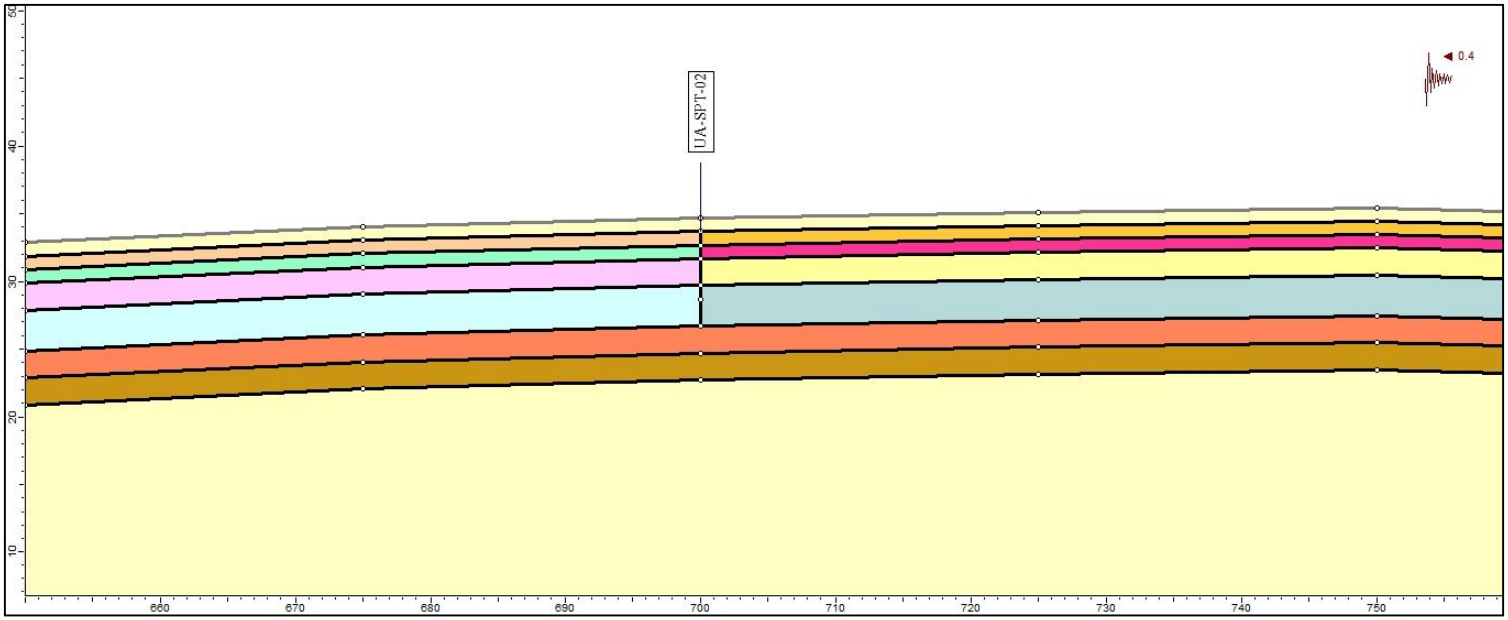

Figure AII-5. Layering for Bin (12) Non-uniform profile

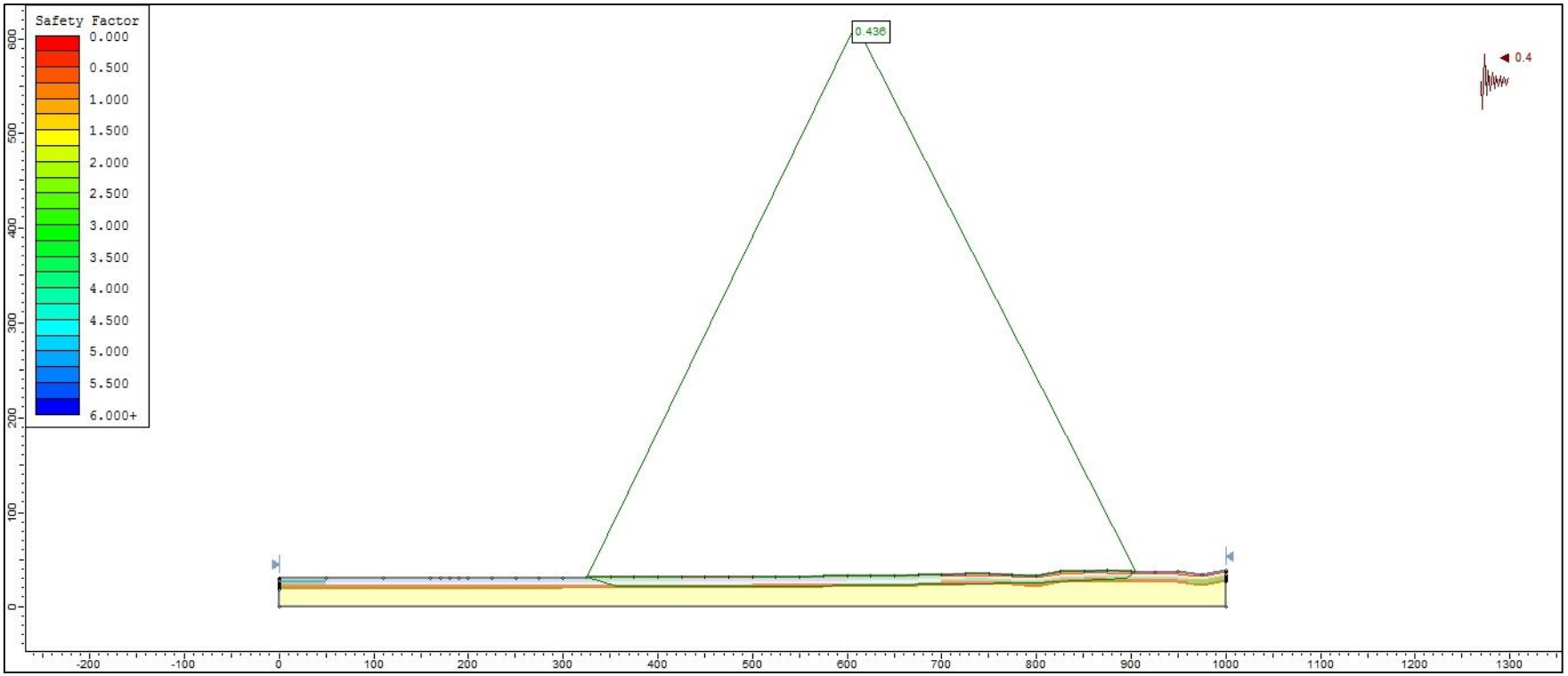

Figure AII-6. Output file for Bin (12), Non-uniform profile

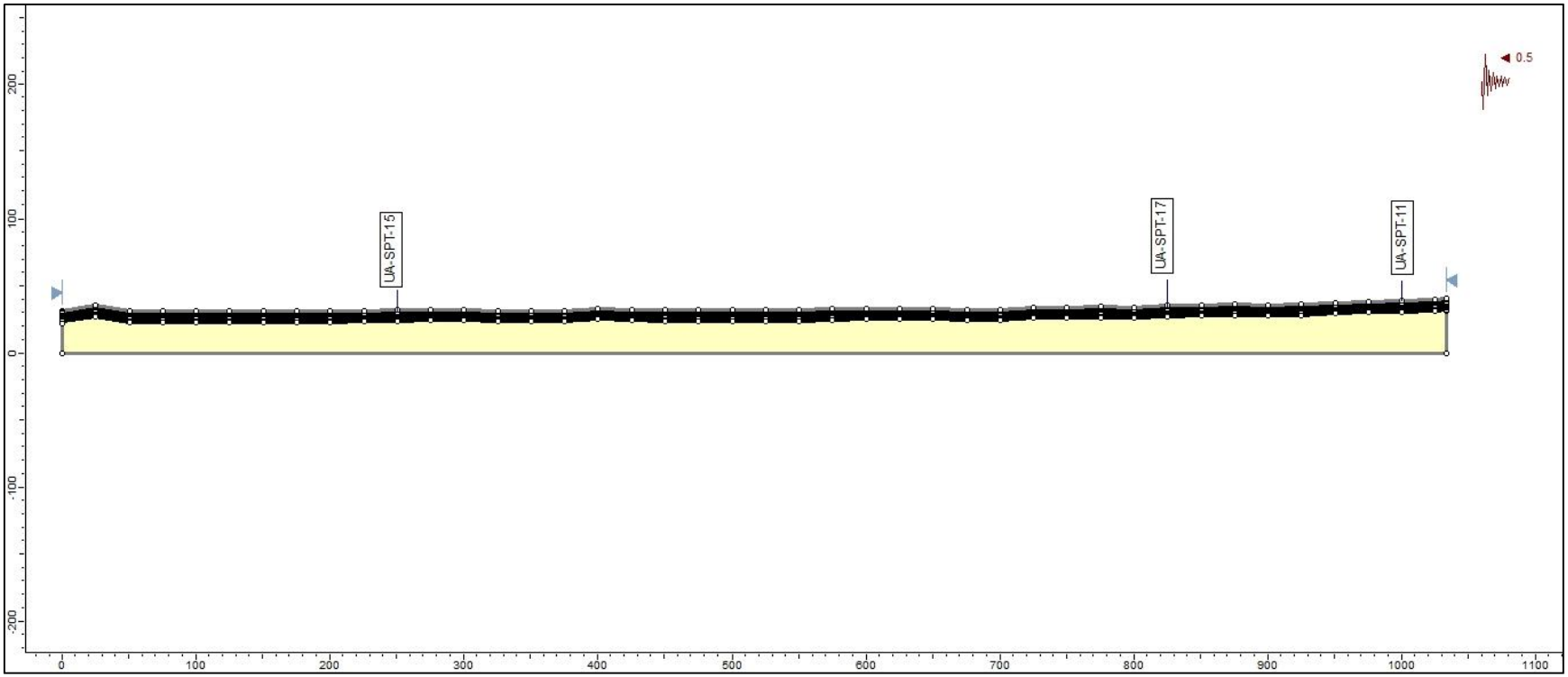

Figure AII-7. SLIDE input file for Bin (20), Non-uniform profile

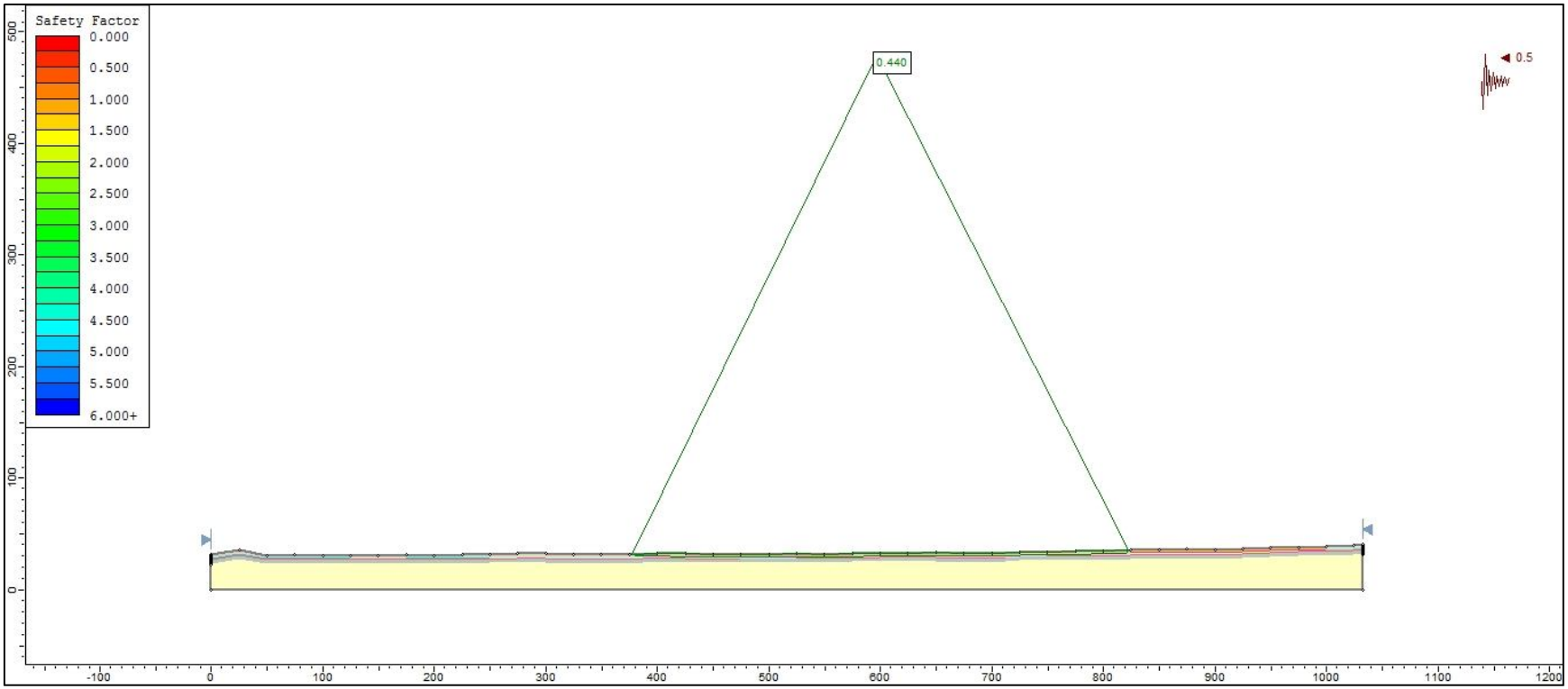

Figure AII-8. Output file for Bin (20), Non-uniform profile

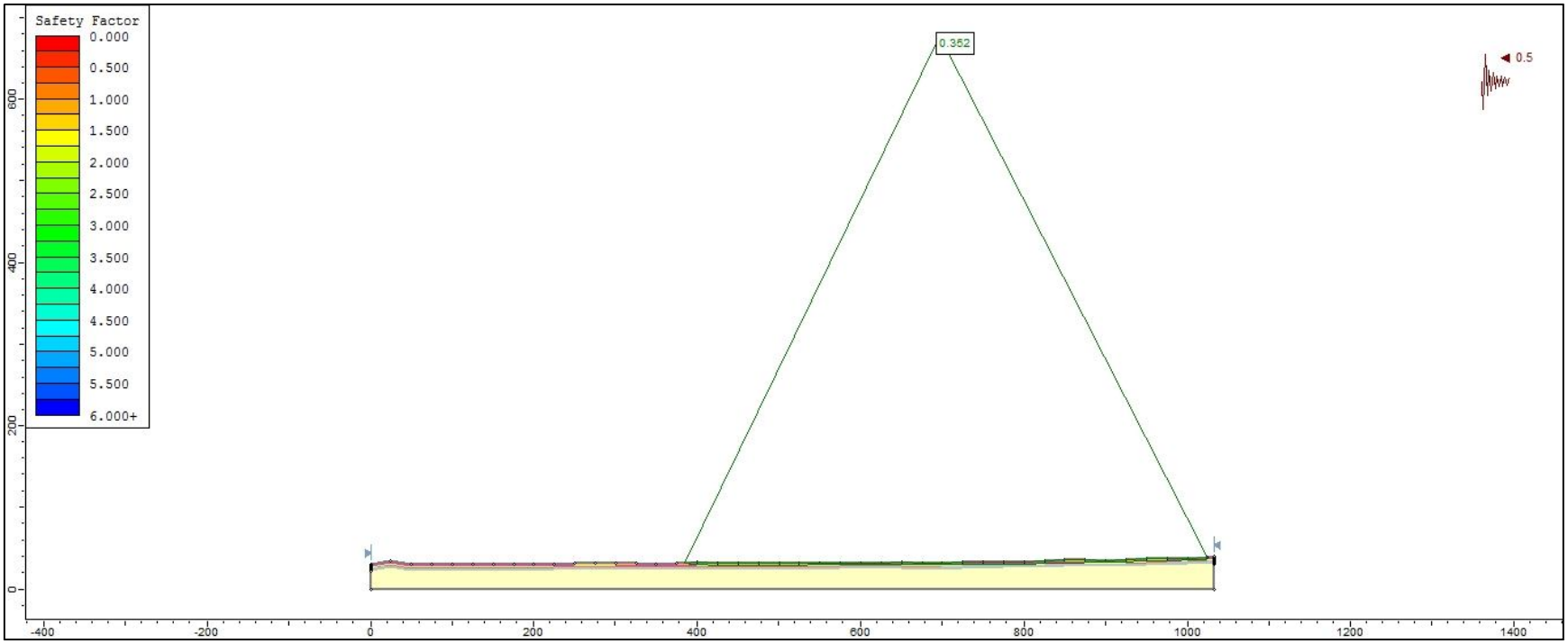

Figure AII-9. Output file for Bin (20), Uniform profile.

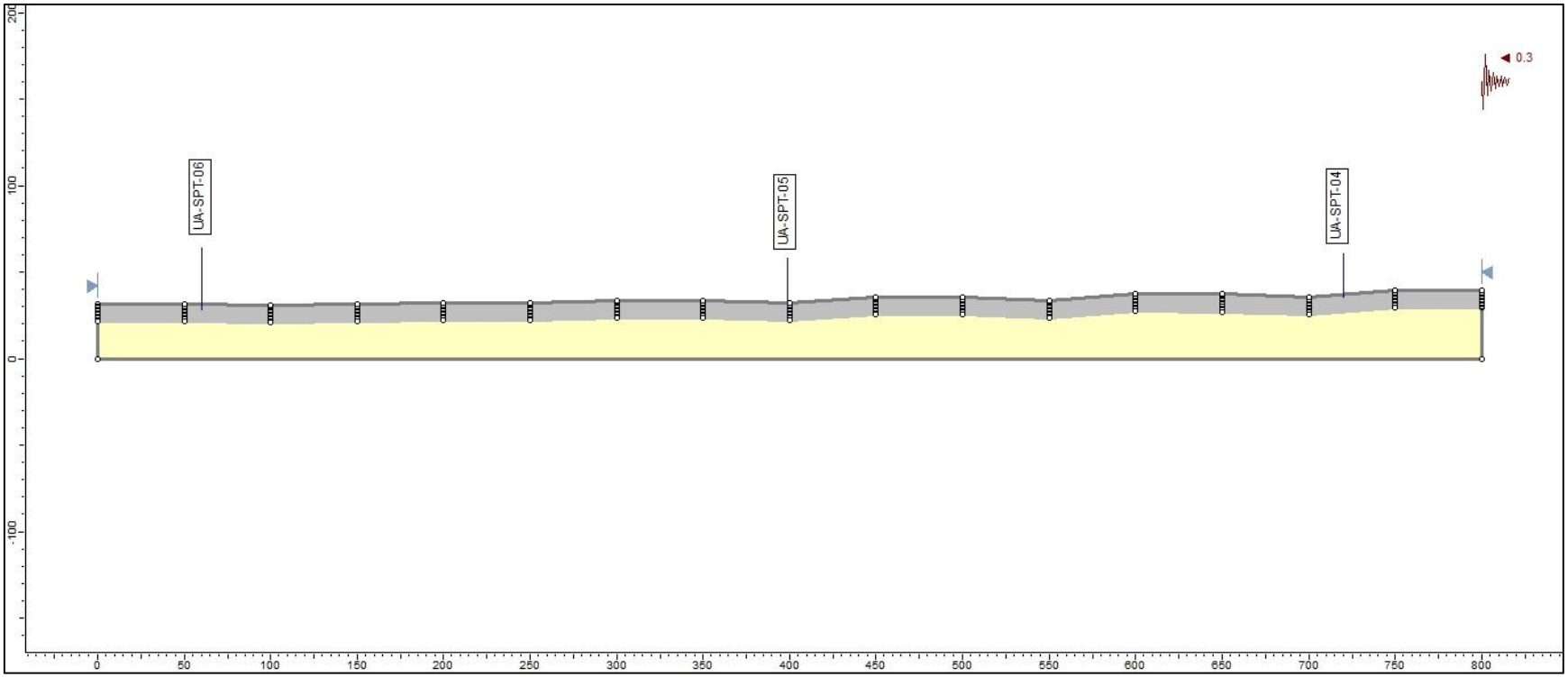

Figure AII-10.SLIDE input file for Bin (3), Uniform profile

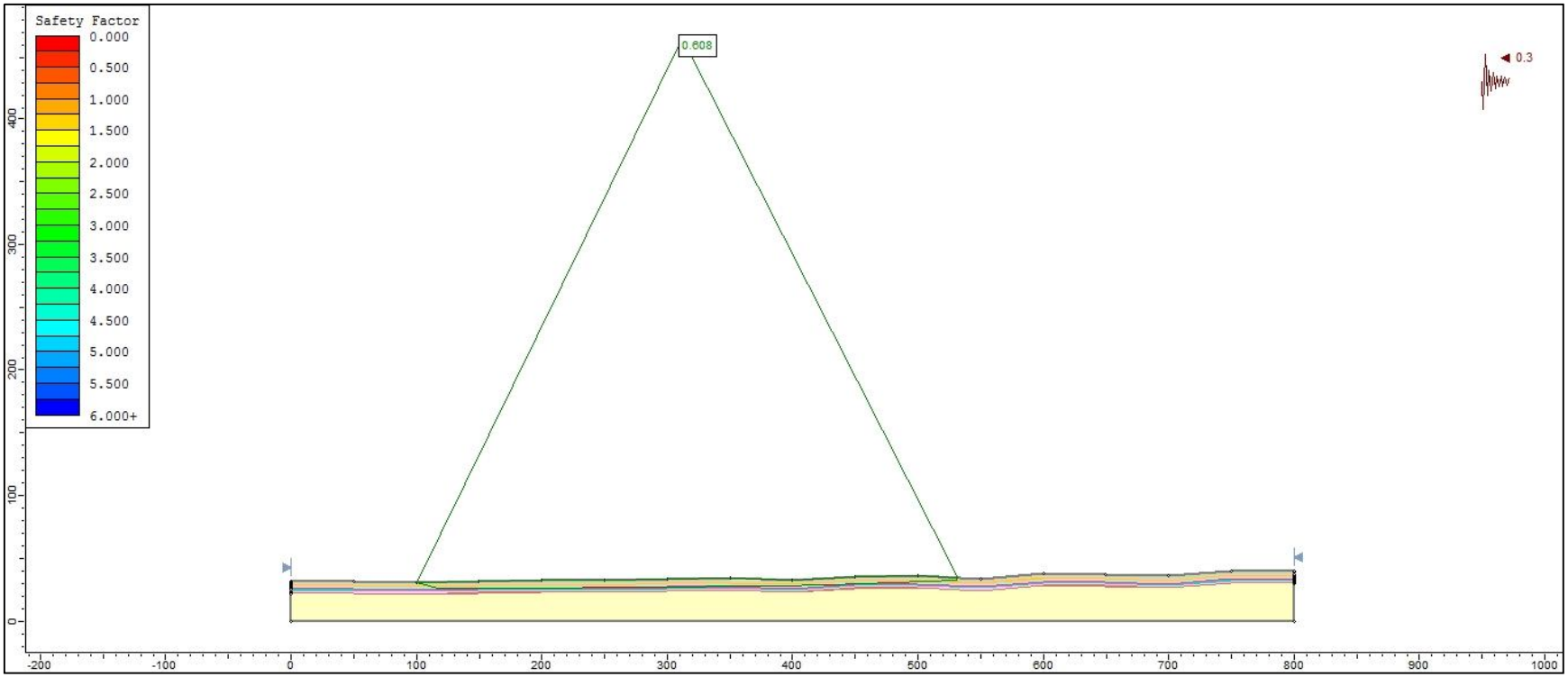

Figure AII-11. Output file for Bin (3), Uniform profile

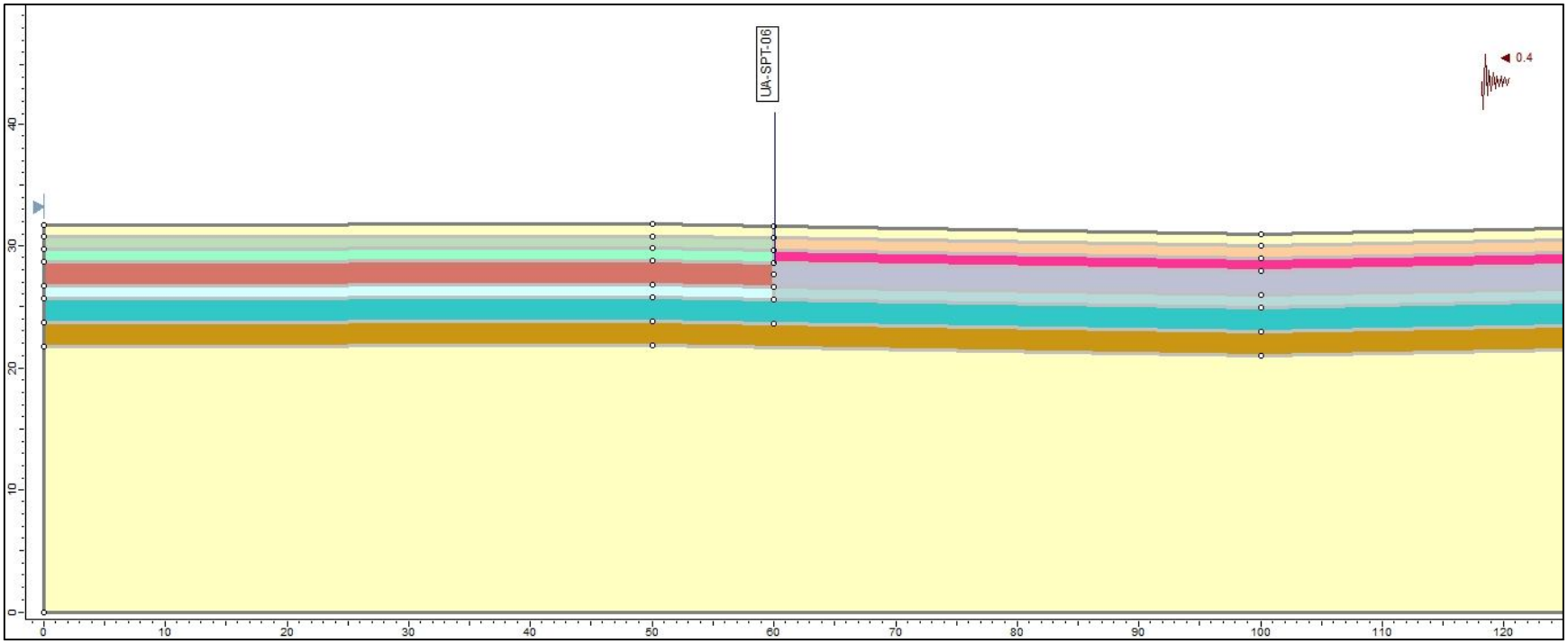

Figure AII-12. Layering for Bin (3), Non-Uniform profile

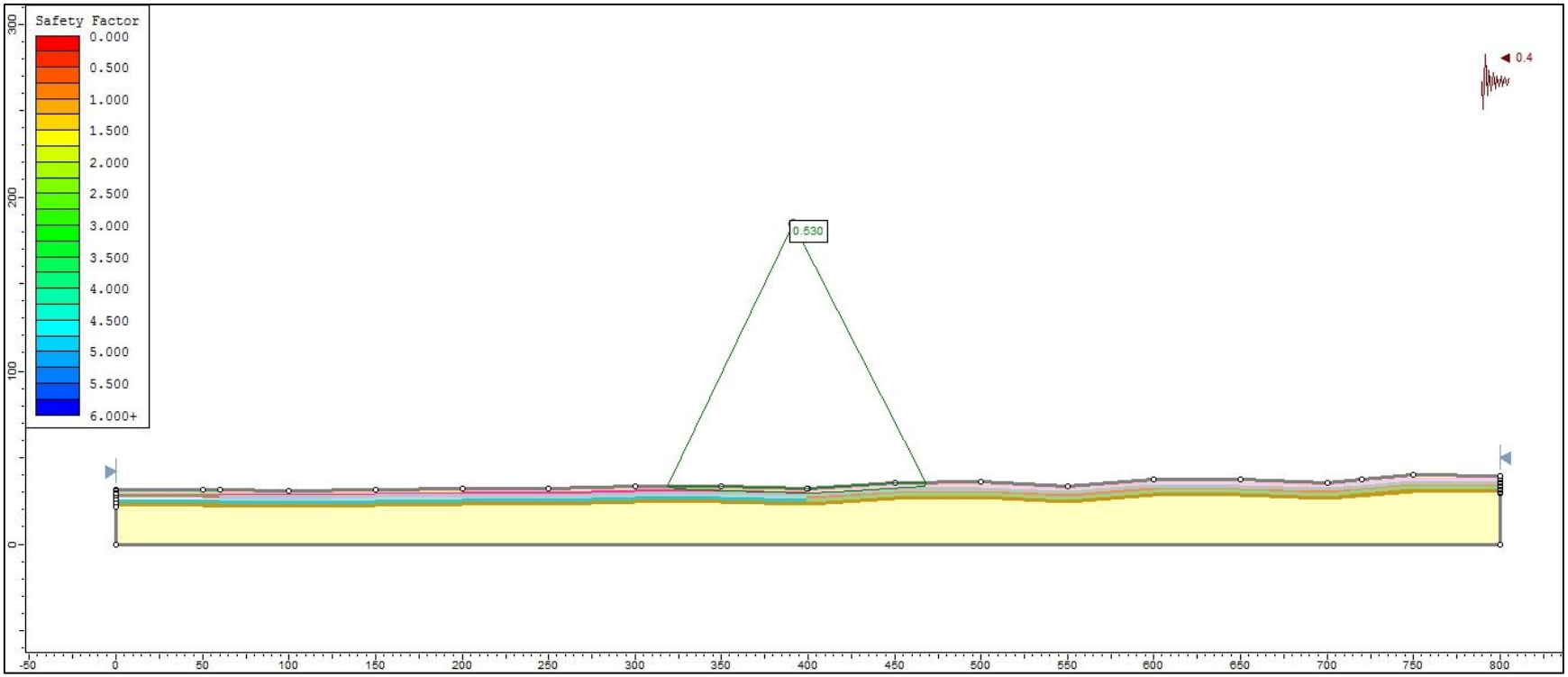

Figure AII-13. Output for Bin (3), Non-uniform profile

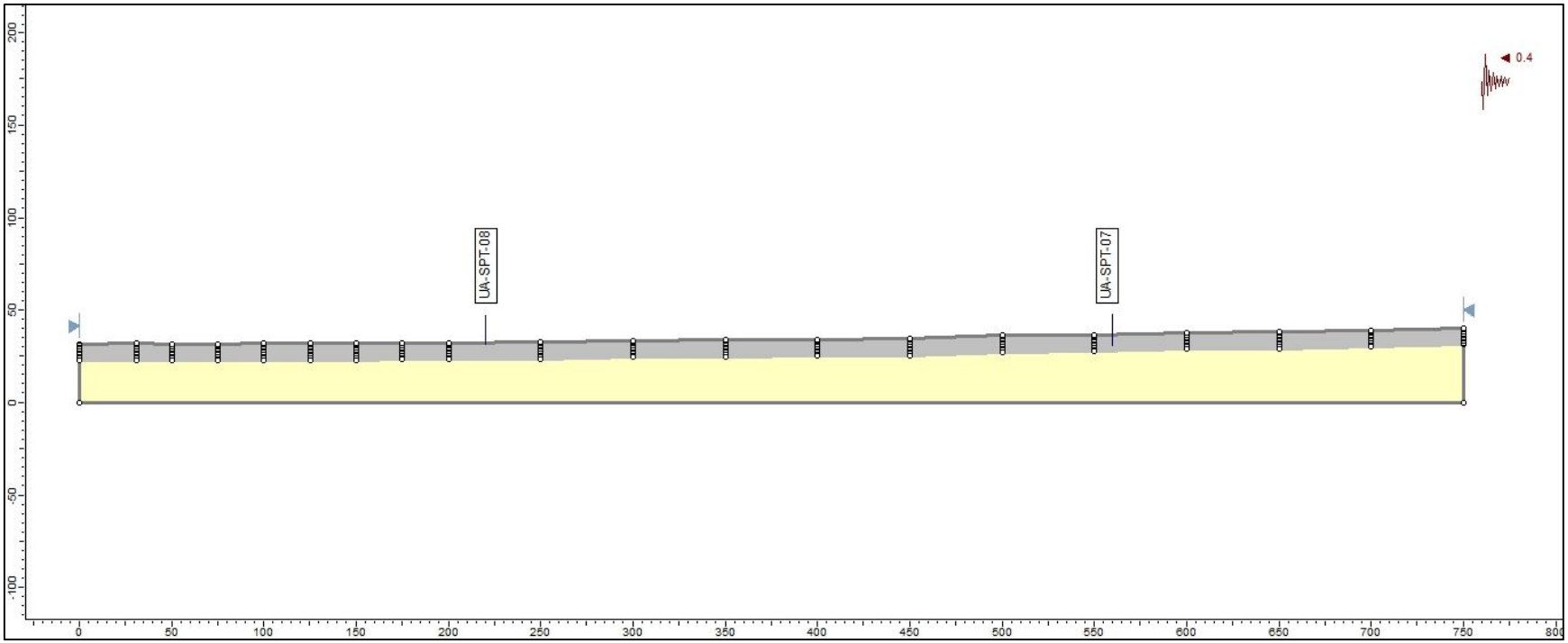

Figure AII-14. SLIDE file for Bin (2), Uniform profile

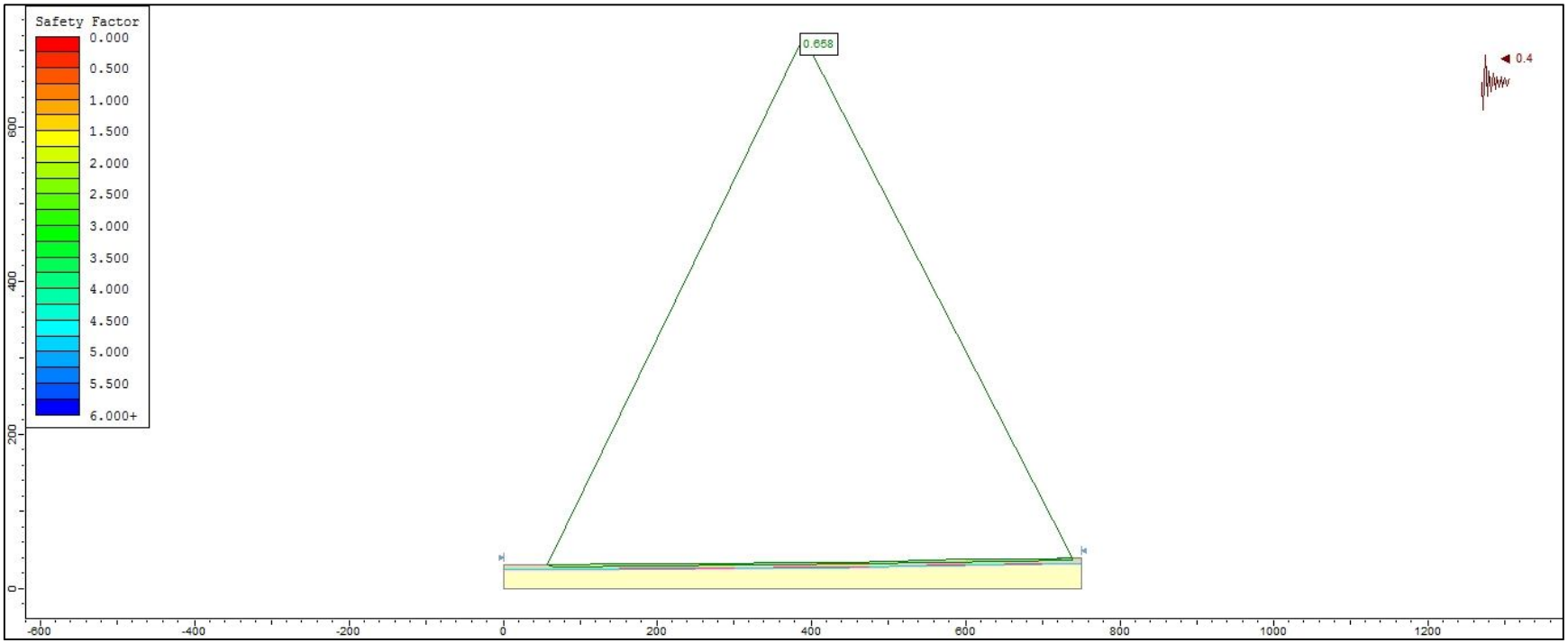

Figure AII-15. Output file for Bin (2), Uniform profile

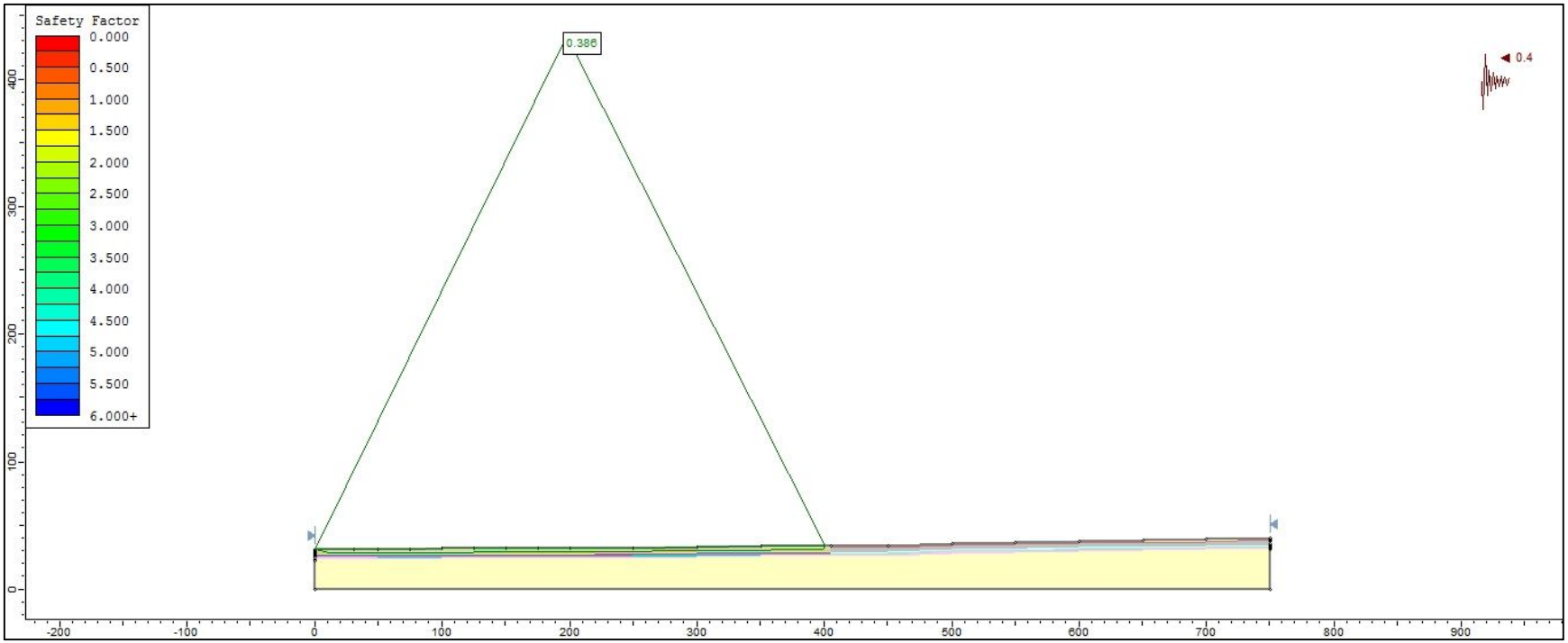

Figure AII-16. Output for Bin (2), non-uniform profile

Appendix III: Summary of Bayesian Updating Technique and Results

This section of the thesis presents a short summary on the Bayesian updating technique used in the methodology. Formulation of the technique is presented below.

Most of the engineering discussions are made in the face of uncertainty. Researchers have made consistent efforts to account for the uncertainty in the field in by discussing the use of probabilistic methods in general engineering practice. Observations in the field are the key in reducing the uncertainty of any hypothesis. An engineer might possess a sound knowledge of the site conditions and the maintenance operation but, there still exists some uncertainty on the outcome of the operations on the field. To account for the uncertainties in the field, use of Bayesian updating technique is suggested. This probabilistic method updates the uncertainty as more information is learned by the engineer in the process of field exploration results.

The research presented in this thesis deals with the uncertainty in estimating the liquefied shear strength ratio in the Canchamana complex. The study assumes that complete liquefaction occurred over the marine terrace. Based on the assumed distributions of '*c*' value, PGA and the ratio of PGA to MHEA, a Bayesian updating approach is formulated in the Tables discussed shown below.

The following points are the key in understanding the Tables discussed below:

- A polynomial expression for a 'failed' and a 'non-failed' bin is derived from the *Limit State* line, relation in MHEA vs. 'c' space.
- The *'c'* value follows a uniform distribution with bounds 0.002 and 0.06 (i.e. a = 0.002 and b = 0.06).
- MHEA/PGA, (k) follows a uniform distribution with bounding values of 0.4 and 1.0 (say, g = 0.4 and h = 0.1)
- PGA follows a log-normal distribution, such that logarithm of a PGA value follows a normal distribution.
- PGA^* is the peak ground acceleration that caused the failure.
- P (PGA<PGA^*) is the probability of PGA (an uncertainty in our case) being less than PGA^*.
- P (F | c) denotes the probability of failure, given we know the 'c' value.
- Posterior distribution of *'c'* value given that failure is observed in the field is denoted by f (c | F).

  Table AIII-1 presents the limit state line equations for the bins, which define the relation between MHEA (g) and *'c'* value. Tables AIII-2 to AIII-4 denote the set-up of the Bayesian updating technique for a 'failed' bin, a 'non-failed' bin and calculation of the posterior distribution to get an approximation of the modal *'c'* value.

Table AIII-1. Limit State Line equation for bins. The equation gives the MHEA as a function of c

Bin	**Failed (F) or Non-Failed Bin(NF)**	***Limit State* Line equation for non-uniform profile**	***Limit State* Line equation for uniform profile**
Bin (3)	F	$2.57c^2+0.63c+0.17$	$3.73c^2+0.43c+0.14$
Bin (12)	F	$8.94c^2+0.306c+0.18$	$6.59c^2+0.18c+.16$
Bin (2)	NF	$1.6c^2+0.833c+0.134$	$0.97c^2+0.61c+.13$
Bin (20)	NF	$3.89c^2+0.617c+0.14$	$5.4c^2+0.23c+.135$

Equations for evaluating parameters in Bayesian Updating:

$$PGA^* = MHEA/(k) \quad \text{(AIII-1)}$$

$$P(PGA < PGA^*) = NORM.DIST(lnPGA, \mu_{lnPGA}, \sigma_{lnPGA}, 1) \quad \text{(AIII-2)}$$

Where NORM.DIST is the excel function for the normal distribution function in Excel.

$$P(F \mid c) = 1 - [P(PGA < PGA^*)] \quad \text{(AIII-3)}$$

$$f(c) = 1/(b-a) \quad \text{(AIII-4)}$$

$$f(k) = 1/(h-g) \quad \text{(AIII-5)}$$

$$f(c \mid F) = P(F \mid c) \cdot P(PGA < PGA^*) \cdot f(c) \quad \text{(AIII-6)}$$

Note: All the equations used are as per the functions available in Microsoft Excel version 2013.

Table AIII-2. Bayesian updating technique set-up for 'Failed' bin

Failed Bin					
c value	MHEA(g)	PGA^*(g)	LN(PGA^*)	P(PGA<PGA^*)	P(F | c)
From *Limit State* Line equation for FAILED bins		PGA at failure for a given c	Converting to normal distribution	Probability of No Failure of the bin	Probability of Failure of the for a given c
From Table AIII-1		Eq. (1)		Equation (2)	Equation (3)

Table AIII-3. Bayesian updating technique set-up for a 'Non-Failed' bin

Non - Failed Bin				
c value	MHEA(g)	PGA^*(g)	LN(PGA^*)	P(PGA<PGA^*)
From *Limit State* Line equation for NON-FAILED bins		PGA at failure for a given c	Converting to normal distribution	Probability of No Failure of the bin
From Table AIII-1		Eq. (1)		Equation (2)

Table AIII-4 Evaluating posterior distribution from the 'failure' and 'no-failure' probabilities of the bins

$P(PGA<PGA^*)$	$P(F \mid c)$	$f(c)$	$f(c \mid F)$
Probability of No Failure of the bin	Probability of Failure of the for a given *c*	Probability distribution function of the '*c*' value (prior)	Posterior Distribution
Equation (2)	Equation (3)	Equation (4)	Equation (6)

Table AIII-5 shows the calculation for a combination of bin (3) and (2) for Approach B of non-uniform profiles with an assumed median PGA = 0.31 g and standard deviation of PGA = 0.1 up to '*c*' value = 0.002. We note that Table AIII-5 extends up to '*c*' value = 0.06. Table AIII-6 shows the calculation for a combination of bin (12) and (20) for Approach A uniform profiles with an assumed median PGA = 0.26 g and standard deviation of PGA = 0.2 up to '*c*' value = 0.002. We note that Table AIII-5 extends up to '*c*' value = 0.06.

Table AIII-5. Bayesian Updating Tables for Non-Uniform profile for a combination of 'failed' Bin (3) and 'non-failed' Bin (2) for median PGA = 0.31 g and standard deviation of PGA = 0.1

	Failed Bin					**Non - Failed Bin**					
***c* value**	**MHEA(g)**	**PGA*(g)**	**LN(PGA*)**	**P(PGA<PGA*)**	**P(F| *c*)**	**MHEA(g)**	**PGA(g)**	**LN(PGA*)**	**P(PGA<PGA*)**	**f (*c*)**	**Posterior**
0	0.17	0.283333	-1.26113	0.1842	0.8158	0.134	0.223333	-1.50	0.0005	16.72	0.01
0.0001	0.170063	0.283438	-1.26076	0.1852	0.8148	0.134083	0.223472	-1.50	0.0005	16.72	0.01
0.0002	0.170126	0.283544	-1.26039	0.1862	0.8138	0.134167	0.223611	-1.50	0.0005	16.72	0.01
0.0003	0.170189	0.283649	-1.26002	0.1872	0.8128	0.13425	0.22375	-1.50	0.0006	16.72	0.01
0.0004	0.170252	0.283754	-1.25965	0.1882	0.8118	0.134333	0.223889	-1.50	0.0006	16.72	0.01
0.0005	0.170316	0.283859	-1.25928	0.1892	0.8108	0.134417	0.224028	-1.50	0.0006	16.72	0.01
0.0006	0.170379	0.283965	-1.2589	0.1902	0.8098	0.1345	0.224167	-1.50	0.0006	16.72	0.01
0.0007	0.170442	0.28407	-1.25853	0.1912	0.8088	0.134584	0.224306	-1.49	0.0006	16.72	0.01
0.0008	0.170506	0.284176	-1.25816	0.1922	0.8078	0.134667	0.224446	-1.49	0.0006	16.72	0.01
0.0009	0.170569	0.284282	-1.25779	0.1932	0.8068	0.134751	0.224585	-1.49	0.0006	16.72	0.01
0.001	0.170633	0.284388	-1.25742	0.1942	0.8058	0.134835	0.224724	-1.49	0.0006	16.72	0.01
0.0011	0.170696	0.284494	-1.25704	0.1953	0.8047	0.134918	0.224864	-1.49	0.0007	16.72	0.01
0.0012	0.17076	0.2846	-1.25667	0.1963	0.8037	0.135002	0.225003	-1.49	0.0007	16.72	0.01
0.0013	0.170823	0.284706	-1.2563	0.1973	0.8027	0.135086	0.225143	-1.49	0.0007	16.72	0.01
0.0014	0.170887	0.284812	-1.25593	0.1984	0.8016	0.135169	0.225282	-1.49	0.0007	16.72	0.01
0.0015	0.170951	0.284918	-1.25555	0.1994	0.8006	0.135253	0.225422	-1.49	0.0007	16.72	0.01
0.0016	0.171015	0.285024	-1.25518	0.2005	0.7995	0.135337	0.225561	-1.49	0.0007	16.72	0.01
0.0017	0.171078	0.285131	-1.25481	0.2015	0.7985	0.135421	0.225701	-1.49	0.0008	16.72	0.01
0.0018	0.171142	0.285237	-1.25443	0.2026	0.7974	0.135505	0.225841	-1.49	0.0008	16.72	0.01
0.0019	0.171206	0.285344	-1.25406	0.2036	0.7964	0.135588	0.225981	-1.49	0.0008	16.72	0.01
0.002	0.17127	0.28545	-1.25369	0.2047	0.7953	0.135672	0.226121	-1.49	0.0008	16.72	0.01
. .	. .	. .	. .	. .	. .	. .	. .	. .	. .	. .	. .

Table AIII-6. Bayesian Updating Tables for Non-Uniform profile for a combination of 'failed' Bin (12) and 'non-failed' Bin (20) for median PGA = 0.26 g and standard deviation of PGA = 0.2

	Failed Bin					Non - Failed Bin					
c(KPa)	**MHEA*(g)**	**PGA*(g)**	**LN(PGA*)**	**P(PGA<PGA*)**	**P(F|C)**	**MHEA*(g)**	**PGA*(g)**	**LN(PGA*)**	**P(PGA<PGA*)**	**f (c)**	**Posterior**
0	0.16	0.266667	-1.321756	0.5504	0.4496	0.135	0.225	-1.49	0.2349	16.67	1.76
0.0001	0.160018	0.266697	-1.321643	0.5506	0.4494	0.135023	0.225038	-1.49	0.2351	16.67	1.76
0.0002	0.160036	0.266727	-1.321529	0.5508	0.4492	0.135046	0.225077	-1.49	0.2354	16.67	1.76
0.0003	0.160055	0.266758	-1.321415	0.5510	0.4490	0.135069	0.225116	-1.49	0.2357	16.67	1.76
0.0004	0.160073	0.266788	-1.321299	0.5513	0.4487	0.135093	0.225155	-1.49	0.2359	16.67	1.76
0.0005	0.160092	0.266819	-1.321183	0.5515	0.4485	0.135116	0.225194	-1.49	0.2362	16.67	1.77
0.0006	0.16011	0.266851	-1.321066	0.5517	0.4483	0.13514	0.225233	-1.49	0.2365	16.67	1.77
0.0007	0.160129	0.266882	-1.320948	0.5520	0.4480	0.135164	0.225273	-1.49	0.2367	16.67	1.77
0.0008	0.160148	0.266914	-1.32083	0.5522	0.4478	0.135187	0.225312	-1.49	0.2370	16.67	1.77
0.0009	0.160167	0.266946	-1.320711	0.5524	0.4476	0.135211	0.225352	-1.49	0.2373	16.67	1.77
0.001	0.160187	0.266978	-1.32059	0.5527	0.4473	0.135235	0.225392	-1.49	0.2376	16.67	1.77
0.0011	0.160206	0.26701	-1.320469	0.5529	0.4471	0.13526	0.225433	-1.49	0.2378	16.67	1.77
0.0012	0.160225	0.267042	-1.320348	0.5532	0.4468	0.135284	0.225473	-1.49	0.2381	16.67	1.77
0.0013	0.160245	0.267075	-1.320225	0.5534	0.4466	0.135308	0.225514	-1.49	0.2384	16.67	1.77
0.0014	0.160265	0.267108	-1.320101	0.5536	0.4464	0.135333	0.225554	-1.49	0.2387	16.67	1.78
0.0015	0.160285	0.267141	-1.319977	0.5539	0.4461	0.135357	0.225595	-1.49	0.2389	16.67	1.78
0.0016	0.160305	0.267175	-1.319852	0.5541	0.4459	0.135382	0.225636	-1.49	0.2392	16.67	1.78
0.0017	0.160325	0.267208	-1.319726	0.5544	0.4456	0.135407	0.225678	-1.49	0.2395	16.67	1.78
0.0018	0.160345	0.267242	-1.3196	0.5546	0.4454	0.135431	0.225719	-1.49	0.2398	16.67	1.78
0.0019	0.160366	0.267276	-1.319472	0.5549	0.4451	0.135456	0.225761	-1.49	0.2401	16.67	1.78
0.002	0.160386	0.267311	-1.319344	0.5551	0.4449	0.135482	0.225803	-1.49	0.2404	16.67	1.78
. .	. .	. .	. .	. .	. .	. .	. .	. .	. .	. .	. . .